

AD-A036 308

NAVAL RESEARCH LAB WASHINGTON D C F/G 20/9
INTENSE RELATIVISTIC ELECTRON BEAM INTERACTION WITH A COOL THET--ETC(U)
JAN 77 D A HAMMER, K A GERBER, W F DOVE

F/G 20/9

UNCLASSIFIED

NRL-MR-3439

NL

1 OF 2
AD
A036308



ADA 036308

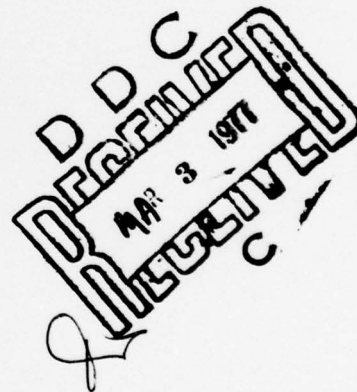
NRL Memorandum Report 3439

Intense Relativistic Electron Beam Interaction with a Cool Theta Pinch Plasma

D. A. HAMMER, K. A. GERBER, W. F. DOVE, G. C. GOLDENBAUM,
B. G. LOGAN, K. PAPADOPOULOS, AND A. W. ALI

Plasma Physics Division

January 1977



NAVAL RESEARCH LABORATORY
Washington, D.C.

Approved for public release; distribution unlimited.

UNCLASSIFIED

SECURITY CLASSIFICATION OF THIS PAGE (When Data Entered)

9 REPORT DOCUMENTATION PAGE		READ INSTRUCTIONS BEFORE COMPLETING FORM
1. REPORT NUMBER NRL Memorandum Report, 3439	2. GOVT ACCESSION NO.	3. RECIPIENT'S CATALOG NUMBER
4. TITLE (and Subtitle) Intense Relativistic Electron Beam Interaction with a Cool Theta Pinch Plasma.	5. TYPE OF REPORT & PERIOD COVERED Interim report on a con- tinuing NRL problem.	
6. PERFORMING ORG. REPORT NUMBER		7. CONTRACT OR GRANT NUMBER(s)
8. AUTHOR(s) D.A. Hammer, K.A. Gerber, W.F. Dove, G.C. Goldenbaum, B.G. Logan, K. Papadopoulos, and A.W. Ali		9. PROGRAM ELEMENT, PROJECT, TASK AREA & WORK UNIT NUMBERS NRL Problem H02-28B
10. PERFORMING ORGANIZATION NAME AND ADDRESS Naval Research Laboratory Washington, D.C. 20375		11. REPORT DATE January 1977
12. CONTROLLING OFFICE NAME AND ADDRESS Naval Research Laboratory Washington, D.C. 20375		13. NUMBER OF PAGES 115
14. MONITORING AGENCY NAME & ADDRESS (if different from Controlling Office) 12-115p.		15. SECURITY CLASS. (of this report) Unclassified
15a. DECLASSIFICATION DOWNGRADING SCHEDULE		
16. DISTRIBUTION STATEMENT (of this Report) Approved for public release; distribution unlimited.		
17. DISTRIBUTION STATEMENT (of the abstract entered in Block 20, if different from Report) 14 NRL-MR-3439		
18. SUPPLEMENTARY NOTES Supported in part by a National Research Council Research Associateship. *Energy Research and Development Administration, Washington, D.C. 20545 +University of Maryland, College Park, Maryland 20742 #Lawrence Livermore Laboratory, Univ. of Cal., Livermore, California 94550		
19. KEY WORDS (Continue on reverse side if necessary and identify by block number) Intense Electron Beams Beam-Plasma Heating Ionization by Electron Beams		
20. ABSTRACT (Continue on reverse side if necessary and identify by block number) Experimental results are presented for the heating of a 4 m long plasma confined by a uniform magnetic field of 4-5 kG by an intense relativistic electron beam. The initial plasma density ranged from ~5 x 10 ¹³ /cm ³ to ~3 x 10 ¹⁵ /cm ³ , the lower density cases being partially ionized and the higher density cases highly ionized. In all cases, the energy coupled from the beam to the plasma is greater than can be explained by binary collisions between beam electrons and the plasma particles. Over most of the density range tested, 5 x 10 ¹³ /cm ³ to 1.5 x 10 ¹⁵ /cm ³ - the		

DD FORM 1 JAN 73 1473

EDITION OF 1 NOV 65 IS OBSOLETE
S/N 0102-014-6601

UNCLASSIFIED

1 SECURITY CLASSIFICATION OF THIS PAGE (When Data Entered)

251 950

4/3

UNCLASSIFIED

SECURITY CLASSIFICATION OF THIS PAGE (When Data Entered)

plasma heating cannot be explained by classical processes. These results are found to be explained quantitatively by the use of a full nonlinear treatment of the electron-electron two stream instability in the kinetic regime. A review of beam plasma interaction theory and previous experiments is presented to facilitate comparison with the present results.

UNCLASSIFIED

ii SECURITY CLASSIFICATION OF THIS PAGE (When Data Entered)

CONTENTS

I. INTRODUCTION	1
II. REVIEW OF INTERACTION MECHANISMS AND PREVIOUS EXPERIMENTS	5
III. EXPERIMENTAL APPARATUS AND CHARACTERIZATION OF THE BEAM AND INITIAL PLASMA	20
IV. EXPERIMENTAL RESULTS	28
V. THEORETICAL CONSIDERATIONS	44
VI. CONCLUSIONS	55
ACKNOWLEDGMENT	57
APPENDIX A	58
APPENDIX B	61
REFERENCES	67

CLASS	Write Section <input checked="" type="checkbox"/>
UNCLASSIFIED	Both Section <input type="checkbox"/>
JUSTIFICATION	
BY	DISTRIBUTION/AVAILABILITY CODES
DATE	AVAIL. and/or SPECIAL
A	

Intense Relativistic Electron Beam Interaction with a Cool Theta Pinch Plasma

I. INTRODUCTION

The recent availability of electron beam generators¹⁻⁵ capable of producing in excess of 1 MJ of relativistic electrons in times of ~ 100 ns has stimulated a great deal of interest in their application to Controlled Thermonuclear Fusion Research. The beam-plasma systems under investigation can be divided into inertially confined and magnetically confined configurations. In the inertial confinement case, present efforts are directed toward the development of beam generators capable of producing the required high power ($\sim 10^{14}$ W), short pulse ($\sim 10^{-8}$ s) electron beams, and the focusing of such beams onto small targets.³⁻⁷ On the other hand, in magnetically confined systems, it is total energy, rather than power, that matters, so long as the beam pulse duration is less than the energy loss time of the confinement system. Therefore, the 10^{-8} s pulsed intense relativistic electron beams (IREB's) presently under development⁸ are appropriate, and it appears that the main problem areas here lie in the compatibility of IREB heating and the confinement system. In particular, the strength of the interaction must be such as to efficiently deposit the beam energy in the plasma. In an open system, such as a high magnetic field, long solenoid,⁹ the energy deposition length must be the system length. If a beam can be injected

Note: Manuscript submitted December 27, 1976.

into a toroidal system¹⁰ without seriously affecting the energy confinement, the deposition length can be much longer so long as the beam energy is deposited before it is lost by such processes as synchrotron radiation.¹¹ Therefore, the strength, as measured by the energy deposition length (or time), and the characteristics of the interaction between an intense beam and a plasma will determine the potential applicability of IREB's to heating magnetically confined plasmas. In particular, since the classical Maxwellian plasma interaction lengths are too long for efficient deposition in plasmas even in the 10^{17} cm^{-3} density range, collective energy coupling processes are required.

Beam-plasma interaction experiments previously reported¹²⁻²⁶ have observed interaction strengths which imply that a collective interaction must be taking place. The present work was directed toward investigating the beam-plasma interaction under conditions in which the strength and the characteristics of the physical processes involved could be studied in detail. It was designed so that several of the difficulties in interpreting the results of previous experiments were eliminated. Thus, a 4 m long uniform plasma was used to avoid magnetic field and plasma inhomogeneities. Secondly, the plasma density was high enough that Thomson scattering could be used to determine plasma electron density and temperature. Finally, the beam current density was kept low enough ($\leq 2 \text{ kA/cm}^2$) that detailed local magnetic field measurements could be made within the beam channel without probe destruction.

Summarizing the experiment, a 0.5 - 1 MeV, 25 - 80 kA, 60 - 70 ns electron beam was injected into preionized plasma confined in a 4 m long theta pinch by a 4-5 kG magnetic field. In addition to Thomson scattering

and magnetic probes, diagnostics used to study the beam plasma interaction included 1) diamagnetic loops surrounding the plasma, principally to compare with the other diagnostics, 2) visible light, to diagnose the characteristics of the plasma discharge, 3) x-band microwave apparatus, to monitor radiation near the electron cyclotron frequency, and 4) hard x-rays, to study the angular spread of the beam. Two different plasma conditions were investigated. In the first one, 100 mTorr of helium was partially ionized to produce a $(0.5 - 4) \times 10^{14}/\text{cm}^3$, 1 - 2 eV plasma at the time of beam injection. For these experiments, the beam to plasma density ratio was $\sim 10^{-2} - 10^{-3}$ and the fraction of beam energy coupled to the plasma was $\sim 5\%/m$. However, a large fraction of this energy was lost to atomic processes (ionization and line radiation). Preliminary results for these plasma conditions were presented by Goldenbaum, *et al.*²⁴ The second plasma condition was highly ionized hydrogen at a density of $(0.5 - 4) \times 10^{15}/\text{cm}^3$ and temperature of 2 - 3 eV (electrons and ions). In this case the beam to plasma density ratio was $10^{-3} - 10^{-4}$ and the energy coupling efficiency was 1 - 2%/m. Since electron and ion temperatures were equal at the time of beam injection, the ion acoustic instability was probably not present. The high plasma density and small neutral fraction made it possible to obtain the heating rate during the beam pulse by Thomson scattering. For plasma density below $2 \times 10^{15}/\text{cm}^3$, evidence for nonclassical heating was obtained. Furthermore, detailed magnetic probe measurements were made of changes in magnetic field components during the beam-plasma interaction. The axial field showed a rapidly rising (~ 20 ns) diamagnetic signal which (on average) continued to rise slowly throughout the beam pulse. The heated cross sectional

area after beam passage was more than twice the beam area. The azimuthal magnetic field indicated a net axial current density within the interaction region which was much higher than predicted by return current theory assuming classical dissipation.²⁷ The anomalously large heating rate and the high net current density can be explained by approximately the same effective collision frequency during the beam plasma interaction. Finally at the highest densities ($> 2 \times 10^{15}/\text{cm}^3$), classical resistivity return current heating adequately accounts for the observations. Part of the results obtained under the highly ionized plasma conditions were reported in preliminary form by Dove, et al.²⁵

Clearly an understanding of these results requires a comparison with expectations based upon the various beam plasma interaction mechanisms which have been discussed.²⁸ We find that the electron-electron two stream instability can provide the anomalous resistivities and heating rates observed in the present experiments. If the model used to explain our results applies into the high temperature plasma regime, then it can be expected that longer pulse duration electron beams will have greater overall plasma heating efficiency. This is because, for a given beam-to-plasma density ratio, the instantaneous coupling efficiency increases as the plasma is heated.

The organization of this article is as follows: In order to facilitate comparison with our results, in Sec. II we review intense beam-plasma interaction mechanisms, and previous experimental results. In Sec. III, we describe the experimental apparatus, including the plasma source, the electron beam generator, the diagnostics and the characteristics of the initial plasma and the beam. In Sec. IV, we discuss

the experimental results, and in Sec. V they are interpreted in terms of theoretical predictions. Finally in Sec. VI, we discuss the implications of the present work to application of IREB's to controlled fusion in magnetically confined systems.

II. REVIEW OF INTERACTION MECHANISMS AND PREVIOUS EXPERIMENTS

A. Theoretical Interaction Mechanisms

Coupling of the energy of an IREB into a plasma by collective processes can occur by several mechanisms. Several of these have been reviewed recently by Breizman and Ryutov.²⁸ We divide the collective mechanisms into two main categories, microscopic and macroscopic. In the first, the beam excites an instability, and the individual electrons interact directly with large amplitude waves which are present at saturation. Thus, the beam transfers its energy to waves, which pass it in turn to the plasma. The instability which has received the most attention in this regard is the electron-electron two stream instability,²⁸⁻³⁵ although other instabilities have also been considered.^{28,36} The macroscopic category includes effects which are unique to intense beams, namely the induced return current,^{27,37-40} the presence of large self fields if the beam is not fully charged neutralized or current neutralized by plasma motion,^{28,37,41,42} and the large transverse pressure exerted by the beam against a confining magnetic field, particularly if the beam is rotating across field lines.^{23,43,44} We now proceed to discuss briefly some of the main characteristics of these mechanisms.

The electron-electron two stream instability (e-e mode) is driven by the relative drift between beam and plasma electrons. Linear

growth rates for unstable waves have been calculated,²⁸ recalculated,³¹ reviewed,²⁸ and then calculated again^{32,33} for evermore "realistic" conditions, meaning conditions which more closely approximate the experiments. For example, the maximum growth rate δ for a "cold" beam satisfying $(n_b/n_p)^{1/3} \gamma \ll 1$ is

$$\delta = \sqrt{\frac{3}{2}} \frac{\omega_p}{\gamma} \left(\frac{n_b}{n_p} \right)^{1/3} (\cos^2 \bar{\theta} + \gamma^2 \sin^2 \bar{\theta})^{1/3}, \quad (1)$$

where n_b and n_p are the beam and plasma densities, respectively, γmc^2 is the beam electron energy, $\omega_p = (n_p e^2 / \epsilon_0 m)^{1/2}$ is the plasma frequency and $\bar{\theta}$ is the angle of the wavevector \underline{k} with respect to the beam propagation direction. (The quantities m , $-e$, c , and ϵ_0 are the mass and charge of the electron, the velocity of light and the permittivity of free space, respectively.) A beam is "cold" when³⁴

$$\Delta v_{\parallel} / c \cong \bar{\theta}^2 + \Delta E / \gamma^3 mc^2 \ll \frac{1}{\gamma} \left(\frac{n_b}{n_p} \right)^{1/3}, \quad (2)$$

where the parallel velocity spread Δv_{\parallel} is due to either the beam energy spread ΔE or the spread in angle of beam electron velocity vectors relative to the beam propagation direction, represented here by the mean angle $\bar{\theta}$. This is the so-called hydrodynamic limit of the instability, in which all of the beam particles see the same phase of the unstable waves, and interact with them coherently as one fluid, on the timescale of the instability ($\sim \delta^{-1}$). In the other limit, called the kinetic, or

warm beam, limit, the growth rate is given by²⁸

$$\delta \approx \omega_p \frac{n_b}{\gamma n_p} \frac{1}{\bar{\theta}^2} \frac{\omega_p^2}{\omega_p^2 + k_{\perp}^2 c^2}, \quad (3)$$

where $k_{\perp} = |k| \sin \bar{\theta}$ and it is assumed that $\bar{\theta}^2 \gg \Delta E / \gamma^3 m c^2$. Similar growth rates can be obtained for strong beams $\left[(n_b/n_p)^{1/3} \gamma \gg 1 \right]$ in these two limits,^{31,32} and for the case when a magnetic field is present, in which case other instabilities are also expected.³³ Unfortunately, the linear growth rate tells only a part of the story since it is the nonlinear limit to which the instability goes which determine the interaction strength and characteristics. Several limiting mechanisms have been discussed, such as quasilinear^{28,29,31} and several wave-wave scattering processes^{28,33} and each gives its own interaction length.^{12,28,31,33} The energy can be removed from the beam either directly via beam electron-wave interaction, as demonstrated graphically by computer simulations,^{30,34-33} or by generating anomalous resistivity,³³ or both. Although the predicted interaction lengths vary by many orders of magnitude they are all short compared to classical interaction length unless the plasma is too inhomogeneous in the direction of beam propagation.²⁸ For example, the quasilinear length,^{28,31} which is the shortest one, is

$$\ell \approx 10 \frac{c}{\omega_p} \frac{n_p}{n_b} \frac{kT_e}{mc^2} \gamma \bar{\theta}^2, \quad (4)$$

where kT_e is the plasma electron temperature. For a $10^{14}/\text{cm}^3$ density, few eV plasma and a $10^{12}/\text{cm}^3$ beam with any mean angle $\bar{\theta}$, ℓ is small

compared to c/ω_p , an extremely short length. In fact it is unreasonably short since the wave energy density used to derive it is sufficiently large that the weak turbulence approximations used in the derivation are invalid.^{28,33} We note that for most of the experiments performed to date, the kinetic growth rate, Eq. (3), should apply, although Thode³⁴ has obtained reasonably good correlation of theory with experimental results with a modified version of the hydrodynamic formulation.

While the microscopic processes just discussed depend upon the ratio n_b/n_p and not on total beam current I_b , the macroscopic interactions may have I_b dependence. Therefore, it is useful to define the ratio v/v , by which the strength of an IREB is commonly measured, before proceeding further. The magnitude of the current in an electron beam is given by

$$I_b \equiv NeV_b \equiv \frac{4\pi\epsilon_0 mc^3}{e} \frac{Ne^2}{4\pi\epsilon_0 mc^2} \beta_b, \quad (5)$$

where N is the number of electrons per meter of beam length and $\beta_b = v_b/c$. In terms of the quantity v , the number of electrons per classical electron radius of beam length $e^2/4\pi\epsilon_0 mc^2 = 2.83 \times 10^{-15}$ m, this is

$$I_b = 17000 v\beta_b \text{ amperes.} \quad (6)$$

As a measure of the strength of the beam self fields, we determine the current, I_c , at which the cyclotron radius r_c of an electron at the boundary of a cylindrical beam of radius b equals $b/2$. At this current, the electron is strongly affected by the beam's self magnetic field $B_\theta(b)$.

Since $r_c = \gamma m v_b / e B_\theta(b)$ and $B_\theta(b) = \mu_0 I_b / 2\pi b = I_b / 2\pi b \epsilon_0 c^2$, we find

$$\begin{aligned} I_c &= 2\pi \epsilon_0 c^2 b B_\theta(b) \\ &= \frac{4\pi \epsilon_0 m c^3}{e} \beta_b \gamma = 17000 \beta_b \gamma. \end{aligned} \quad (7)$$

This "critical" current^{41,45} means that when $v/\gamma \geq 1$, beam self fields, if unneutralized, severely affect electron motion, whereas for $v/\gamma \ll 1$ they do not. Typical value of I_c are 28 kA at 500 keV kinetic energy ($\gamma = 2$), 50 kA at 1 MeV ($\gamma = 3$) and 85 kA at 2 MeV ($\gamma = 5$).

Turning now to the macroscopic interaction processes, we first discuss the induced return current. It is a result of the fact that intense beams are pulsed. The dI/dt in the beam front produces a dB/dt which, by Maxwell's equation $\nabla \times \underline{E} = -\partial \underline{B}/\partial t$, gives rise to an electric field. (The electric field and magnetic induction are \underline{E} and \underline{B} , respectively.) This field tends to slow down beam electrons, but it also tends to accelerate plasma electrons back down the beam channel so as to eliminate the $\partial \underline{B}/\partial t$ (Lenz Law). For a collisionless plasma, when $n_b \ll n_p$ and $\omega_p b/v_b \gg 1$, current neutralization is virtually complete throughout the beam cross section. If $\omega_p b/v_b \leq 1$, then neutralization of the beam current density within the beam channel is only partial. These results are correct in the absence of applied magnetic fields,^{37,38,40} or in the presence of longitudinal or transverse fields,^{27,39} so long as $\omega_p^2 \geq \omega_c^2$, where $\omega_c = eB_0/m$ is the cyclotron frequency of plasma electrons in the applied field B_0 .

Since a plasma is not collisionless, the induced plasma current diffuses out of the beam channel. This has been shown²⁷ to occur on a timescale $T = \left[b^2 / (c/\omega_p)^2 \right] \tau_{col}$, where τ_{col} is the momentum transfer collision frequency of the plasma electrons. $T \gg \tau_{col}$ in a fully current neutralized beam ($\omega_p b/v_b \gg 1$) occurs because energy is delivered inductively from beam electrons to plasma electrons to make up for the energy dissipated (converted to plasma thermal energy) by Ohmic heating.^{28,31,46,47} To summarize, the energy deposited per unit length in the plasma by the return current, Q , is given by⁴⁷

$$Q = \int_0^t dt \int_0^b 2\pi r \mathbf{j} \cdot \mathbf{E} dr = \int_0^t dt R I_p^2, \quad (8)$$

where I_p is the plasma current, \mathbf{j} is the beam current density, and R is the plasma column resistance per unit length within the beam channel. Cylindrical symmetry and axial uniformity are assumed. If there are no space charge electric fields present, then Q is the difference between the work done by the beam and the magnetic field energy per unit length at time t

$$Q = \int_0^t I_b \frac{d\Phi}{dt} dt - \frac{1}{2} L I^2(t), \quad (9)$$

where $I = I_b + I_p$ ($= 0$ at $t = 0$ assuming initially complete current neutralization), and L is the inductance per unit length of the entire beam plasma system. Since $I_b \propto v_b$, and $\gamma \approx (1 - v_b^2/c^2)^{-1/2}$ implies

$\delta v_b/v_b \approx \delta\gamma/\gamma^3$, where δv_b is the velocity decrease of a beam electron due to an energy change of $\delta\gamma$, a relativistic beam electron can lose a large fraction of its energy without changing the beam current significantly. Therefore, we may take I_b out of the integral in Eq. (9) to obtain

$$Q = LI_b I - \frac{1}{2} LI \left(I_b - \frac{1}{2} I \right). \quad (10)$$

Then the energy deposited by the end of the beam pulse is determined by the net current in the system at that time. A reasonable limiting value for the net current is I_c since a larger current is going to face severe magnetic self pinching as we have seen. The time required for the current in a beam with $I_b > I_c$ to reach $I = I_c$ is $\sim T(I_c/I_b)$, at which time, $Q \approx LI_c^2(\gamma/\gamma - 1/2)$. This is always a shorter time than for beam energy deposition by binary collisions between beam electrons and plasma particles for beams and plasmas of interest. How much shorter depends upon τ_{col} , whether it is due to coulomb collisions or is enhanced by the presence of microturbulence due to instabilities. This microturbulence must be low frequency if it is to affect plasma electrons, and can occur either parametrically as a result of the e-e mode^{28,33} or due to instabilities generated by the relative drift between plasma electrons and ions resulting from the return current flow. In the latter category are such instabilities as electron-ion two stream and ion acoustic.^{28,31,46,47} The interaction length from this process can be estimated as

$$\ell \sim \frac{(\gamma - 1)mc^2}{eL \frac{dI}{dt}} \sim \frac{(\gamma - 1)mc^2 \tau_p}{eLI(\tau_p)}, \quad (1)$$

where τ_p is the beam pulse duration. It will vary directly with the effective collision time τ_{col} since (to first approximation) I will vary inversely with τ_{col} . Note that the energy stored in the magnetic field $1/2 LI^2$ in Eq. (10) also ultimately ends up in the plasma by Ohmic dissipation.^{28,48} However, this process can take much longer time than the dissipation during the beam pulse since instabilities have presumably become much weaker or even stabilized.

Also included in the macroscopic collective interaction processes category were the effects of the beam's large self fields and transverse pressure. Suppose, for example, the beam is injected into a low pressure neutral gas. Then until the gas is turned into a plasma the beam self electric and magnetic fields can build up. This can strongly affect the characteristics of the gas breakdown process, determining, in turn, the beam and plasma characteristics after breakdown and the type of interaction that can take place. These processes can reasonably be expected to be strongly affected by the beam strength (v/γ) . Two examples have been studied. In one, the beam self magnetic field, in the absence of an applied guide field, can cause a strong pinch,^{49,50} heating ions as well as electrons. On the other hand, if an IREB is injected into a plasma or neutral gas with a substantial fraction of its energy in the transverse direction, its transverse pressure can substantially exceed the confining pressure of the applied field.

This nonequilibrium situation can result in the generation of large amplitude magnetosonic waves which can also heat both ions and electrons.⁴³ Such expansion waves can also be driven by hot plasma if, for example, the plasma electrons are strongly heated by some instability mechanism (e.g. - electron-electron two stream) in a time short compared to the characteristic plasma expansion time.⁵¹ All of these mechanisms have been observed in experiments, as we shall see in the experimental review.

B. Previous Experimental Results

The availability of intense electron beams in the mid 1960's soon resulted in experimental studies in which beam propagation characteristics were investigated in plasmas and in initially neutral gases.^{41, 52-56} However, no attempt was made to study the beam-to-plasma energy coupling. The first experiment designed to do this was that of Altyntsev, et al.¹² Although a relatively weak beam was used, substantial nonclassical beam-to-plasma energy coupling was observed for n_b/n_p in the range 1 to 10^{-2} . In fact in all studies of energy deposition by an IREB in a plasma in which the density ratio was $\sim 10^{-3}$ or higher, including in the experiment reported here, energy deposition greater than can be explained by classical processes has been observed. Moreover, even when the density ratio was small (again including the present experiment), classical dissipation of the beam-induced return current appears to be the energy coupling mechanism. We note that even this is a collective (nonturbulent, macroscopic) interaction mechanism that would not be present in an ordinary beam-plasma interaction.

Returning now to the experiment of Altyntsev, et al.,¹² a 2 - 3 MeV, 10 kA, 50 ns electron beam was injected into a 3 m long, magnetic mirror confined hydrogen or argon afterglow plasma in the density range $10^{11} - 10^{14}/\text{cm}^3$. The beam density was approximately $10^{11}/\text{cm}^3$ in the interaction volume, and the midplane magnetic field was ≤ 2.5 kG. The interaction strength was diagnosed by monitoring the beam propagation efficiency to the end of the interaction region by beam calorimetry, and by using diamagnetic loops to measure the total transverse energy per unit length of the particles (plasma electrons and ions, and beam electrons). The interaction was found to be strongest when the beam and plasma density were comparable, with most of the beam energy not reaching the end of the system. However, the diamagnetic loops indicated that 10% of the directed beam energy was converted into transverse particle energy, this quantity being optimized at a plasma density of $\sim 10^{12} \text{ cm}^{-3}$. Where the rest of the energy went was unknown. Thus, the interaction length for beam loss was ≤ 3 m for a large enough beam-plasma density ratio. For coupling of beam energy into the plasma, it was perhaps 10 m, much longer than the quasilinear length given in Eq. (4), but still orders of magnitude shorter than is possible by classical collisional processes. Note that 10% of the beam energy equally distributed among all plasma particles in the system corresponds to tens of keV per electron ion pair.

In the Altyntsev, et al., experiment the beam was relatively weak, with $v/\gamma \leq 0.1$. Similar experiments were performed by Smith¹³ and Okamura, et al.,²⁸ using even lower v/γ beams, but again observing much

stronger than classical beam-plasma interaction (also using beam calorimetry and diamagnetic loops). Abrashitov, et al.,¹⁶ and Arzhannikov, et al.,¹⁷ followed up the work of Altyntsev, et al., with a more completely diagnosed experiment, but still a $v/v \ll 1$ beam. In particular, at a plasma density $\sim 10^{14}/\text{cm}^3$, Thomson scattering was used to obtain the plasma transverse electron temperature kT_e . The resulting $n_p kT_e$ was ~ 6 times smaller than the plasma transverse energy inferred from diamagnetic loops. Other diagnostics in this and other experiments suggest a hot electron component,^{15,28} or hot ions,¹⁸ or both, may account for this difference. Since diamagnetic loop measurements were made within 100 ns of beam injection, other possible explanations for the discrepancy are the residual effects of beam diamagnetism,⁵⁷ and magnetosonic waves which have not yet damped.^{44,51} The largest signals were observed for $n_b/n_p = 0.05 - 0.005$. However, at the lower value of n_p ($n_b/n_p > 0.05$), beam propagation was poor (Fig. 4b, Ref. 17).

Two experiments followed shortly after the work of Altyntsev, et al., in which stronger beams, $v/v \approx 1 - 3$, were used. Kapetanakis and Hammer¹⁴ injected a 20 - 40 kA, 400 keV, 50 ns beam into a 40 cm long, mirror confined afterglow hydrogen or helium plasma in the density range $10^{11} - 10^{14}/\text{cm}^3$. Miller and Kuswa¹⁵ used a 50 kA, 350 keV beam of 30 ns duration, and a 30 cm long $10^{12} - 10^{14}/\text{cm}^3$ plasma confined in a uniform magnetic field. Both experiments had beam densities of $10^{12}/\text{cm}^3$, both used diamagnetic loops as the principal diagnostic for beam energy transferred to the plasma, and both observed maximum values of transfer efficiency of $\sim 5\%$. However, these maxima were at different density ratios in the two experiments: at $n_b/n_p \approx 1$ for Kapetanakis and Hammer,

and at $n_b/n_p \approx 10^{-2}$ for Miller and Kuswa. This difference may have been due to the different beam characteristics or plasma confinement configurations. Kapetanakis and Hammer also found plasma diamagnetism to be independent of magnetic field above 2.5 kG and to scale as B^2 below that field, probably a beam or plasma confinement effect. Miller and Kuswa observed soft x-rays at the lower plasma densities confirming the presence of substantially heated plasma electrons. They also made the first mention of magnetosonic oscillations.⁴⁴

Further experiments at intermediate values of v/γ were performed by Korn, *et al.*,¹⁸ and Ekdahl, *et al.*,¹⁹ on the same apparatus. A 10 - 60 kA, 350 keV, 60 ns beam ($v/\gamma \approx 1/2 - 3$) was injected into a fully ionized plasma in the density range $10^{12} - 5 \times 10^{13}/\text{cm}^3$. The mid-plane magnetic field in this 1.6 m long experiment was typically 2.7 kG. As in the case of Kapetanakis and Hammer, the coupling efficiency was highest, up to $\sim 20\%$ of the beam energy deposited in the plasma, at the higher beam to plasma density ratios, again using diamagnetic loops. However, a neutral particle detector was also used and it was found that the plasma ions had gained a substantial amount of energy. This was probably due to large amplitude magnetosonic waves since diamagnetic loop oscillations scaled as B/n as predicted by theory.^{43,44} In one set of experiments, the energy deposition as a function of current was consistent with return current heating in the presence of ion sound turbulent resistivity.¹⁸ In the other experiments,¹⁹ the heating rate required 10 times that resistivity. The use of a foilless diode⁵⁸ in the first set, of experiments and an ordinary foil diode in the second may be the explanation for the different interaction characteristics here.

Furthermore Korn, et al.,¹⁸ suggested that most of the energy deposition occurred in the first few tens of cm of plasma. Previous workers had also seen evidence that this might be the case.^{12,14,16,17} As yet unpublished work on the same apparatus by Sethian, et al.,⁵⁹ has shown a very strong dependence of the interaction strength upon beam mean angle as determined by scattering in the anode foil.⁵⁹ This result, obtained by both Thomson scattering and diamagnetic loops at a plasma density of $5 \times 10^{13}/\text{cm}^3$, points to the presence of the electron-electron two stream instability,³⁴ although return current heating may still be present as well.⁶⁰

Turning now to a higher v/γ beam experiment, Miller²⁰ injected a 600 kA, 100 ns beam ($v/\gamma \approx 5$) into a $\sim 2 \times 10^{13}/\text{cm}^3$ density plasma. Two parameters were varied - the anode foil thickness and the neutral gas pressure. The first of these determines the beam electron mean angle relative to the propagation direction, an important parameter if the two stream instability is operative.^{28,33,34} A decrease by a factor of ~ 10 was observed in diamagnetic loop signals for the thicker foils. The injected beam current density was decreased from a maximum of $\sim 6 \text{ kA}/\text{cm}^2$ ($n_b \approx 10^{12}/\text{cm}^3$) by a factor of ≤ 2 by the thicker foils. Another important result here was that beam diamagnetism, certainly substantially increased by the thicker foils, was not dominating the diamagnetic loop signals. The change in neutral gas density holding the plasma density constant should not affect plasma heating mechanisms unless collisions with neutrals become so numerous as to damp instabilities, or the density changes significantly during the pulse. The small decrease of the observed diamagnetic loop signal at the higher pressures may have been due

to the latter effect since not only would n_b/n_p decrease during the pulse, but also ionization and line radiation can result in substantial plasma kinetic energy loss until full ionization is achieved. The maximum diamagnetic loop signal implied a 1 - 2% energy deposition efficiency, about 1/4 to 1/2 that expected based upon earlier experiments^{12,14-19} at the same value of n_b/n_p . Note that we expect the high v/γ beam Miller used to have no particular effect on interaction strength since $n_p \geq 20 n_b$ and the potentially large beam self fields will be easily neutralized by plasma motion.

In initially neutral gas experiments, however, the high v/γ can be important. In the case of VanDevender, et al.,²¹ a 350 keV, 36 kA ($v/\gamma = 1.6$) 100 ns beam was focused to 25 kA/cm² ($n_b \approx 5 \times 10^{12}$) and injected into hydrogen in the pressure range 50 mTorr - 10 Torr with no applied magnetic fields. At the lower pressures, rather substantial net B_θ , corresponding to a net current of $\sim 30\%$ of the primary beam current, was observed. Since the net current is in the direction of the beam current, during the beam pulse the plasma current is opposite to the net current. Therefore, the plasma is antipinched by the $\underline{j} \times \underline{B}$ volume force. After the beam, the plasma current reverses and the $\underline{j} \times \underline{B}$ force is inward. This antipinching followed by pinching was observed by streak photography, and an ion temperature of ~ 100 eV was found by visible spectroscopy. The electrons, however, were found (by Thomson scattering) to have a non-Maxwellian distribution function with mean energy only ~ 10 eV and a density $\sim 10^{15}/\text{cm}^3$. When the plasma was preionized, the interaction was much weaker, and results were consistent with return current heating, both with and without anomalous resistivity depending upon plasma conditions.

Prono, et al.,²² did use an applied magnetic guide field in their high v/γ neutral gas experiment. They injected a 1 MeV, 200 - 500 kA beam ($v/\gamma = 4 - 10$) of 150 ns duration into neutral hydrogen ranging from 30 mTorr to 1 Torr. In the range 30 - 130 mTorr, where gas breakdown occurs slowly,⁴² the 13 kA/cm² beam ($n_b \approx 2.5 \times 10^{12}/\text{cm}^3$) interacted very strongly, losing $\sim 50\%$ of its energy in the 1 m long experiment, and producing diamagnetic loops signals corresponding to $\sim 1 \text{ J/cm}^3$. Even a small amount of preionization substantially reduced the interaction, pointing to the importance of the initially neutral gas. Similarly, operation at the higher pressures, where gas breakdown occurs quickly,⁴² also greatly weakened the interaction.

The final previously reported beam-plasma interaction experiment to be discussed here, by Kapetanakis, et al.,²³ utilized a sharp magnetic cusp to nonadiabatically convert a beam propagating parallel to a magnetic field (500 keV, 20 - 40 kA, 50 ns) to a beam rotating across magnetic field lines. This rotating beam of density $\sim 5 \times 10^{11}/\text{cm}^3$ was then injected into a plasma in the density range $10^{12} - 10^{14}/\text{cm}^3$. Contrary to the parallel propagation case, this experiment found the strongest beam-to-plasma energy coupling, again as determined by diamagnetic loops, to be at a plasma density of $\sim 10^{14}/\text{cm}^3$. This, however, was in agreement with predictions by Chu and Rostoker.³¹ In their model, the plasma heating is caused by the fields associated with the cross field return current. Ion heating was indicated, although not measured, in this experiment due to the strong magnetosonic oscillations which were observed above $10^{13}/\text{cm}^3$ plasma density.⁴³

We have seen that all of the beam-plasma interaction experiments reported so far have observed rates of energy deposition in the plasma which imply the presence of one or more collective mechanisms. The results of some of the experiments^{12-17,19-21} indicated the presence of the electron-electron two stream instability, particularly at the lower plasma densities, and others^{18,21,22} seemed to imply return current heating. In all of the experiments both mechanisms could have been present. One difficulty in interpreting most of the experimental results is the lack of detailed local measurements of plasma conditions after beam injection. Of the two experiments reported in which Thomson scattering was used to obtain plasma electron density and temperature, one was performed in initially neutral gas,²¹ and the other was in a plasma in which conditions would allow both electron-electron two stream and ion acoustic instabilities to be present.¹⁷ The remaining experiments depended upon nonlocal measurements, mainly diamagnetic loops, to infer beam plasma coupling, and if this is done shortly after beam injection, beam diamagnetism and magnetosonic waves can contribute significantly to the signals.

III. EXPERIMENTAL APPARATUS AND CHARACTERIZATION OF THE BEAM AND INITIAL PLASMA

The electron beam generator used in the present experiment is an 8 Ω , water dielectric coaxial Blumlein⁵ pulse forming line driven by a Marx generator.⁵ The latter consists of twelve 0.5 μ F capacitors which were charged as high as 80 kV each, at which voltage a total of 19 kJ is stored. When the Marx generator is switched into a series configuration,

an output gap is closed and the pulse forming line is charged to peak voltage (up to 1.2 MeV) in approximately 1 μ s. At this time four pressured gas switches are simultaneously triggered by an externally produced high voltage trigger pulse, and a 60 ns (fwhm) pulse is produced. The command triggering of the pulse line switches was incorporated to allow precise timing between beam injection into the plasma and the Thomson scattering diagnostic (see below). The multiple switching serves to reduce the effective switch inductance and, therefore, the rise time of the output pulse. The negative voltage pulse from the pulse forming line is applied to a standard vacuum field emission diode, of the type described by Parker, *et al.*⁶² In this experiment cathodes consisted of flat carbon discs 4 - 7 1/2 cm in diameter. The anode was typically a titanium foil 25 μ m thick, and was spaced 0.7 - 1.2 cm from the cathode. Operating voltages on the cathode-anode gap ranged from 500 keV to as high as 1.4 MeV. (Note that a Blumlein pulse forming line produces a pulsed voltage equal to the charging voltage into a matched load, 8 Ω in this case. Twice the charging voltage is produced on an open circuit.⁵) Electron beam currents ranged from 25 kA to 125 kA. Further details of the generator are available elsewhere.⁶³ Figure 1 shows a sample set of oscilloscope traces of a.) the Marx generator charging the Blumlein pulse forming line, b.) the electron beam diode voltage, and c.) the electron beam current in the diode.

Magnetic field coils were mounted on the accelerator diode so that electrons leaving the cathode followed magnetic field lines through the anode and into the theta pinch target plasma. The rise time of this guide field was long enough (3 ms) to penetrate the stainless steel,

brass, and carbon parts which were inserted within it (see Fig. 2). The amplitude of the guide field was chosen to match the field at the cathode anode gap to the theta pinch magnetic field at the time of beam injection.

The plasma source in this experiment was a 4 m long, 5 μ s rise time theta pinch, together with a Z discharge preionizer. The theta pinch itself was a 20 cm inside diameter single turn coil driven by a 60 kJ, 20 kV capacitor bank. The plasma was contained inside a 15 cm inside diameter glass vacuum vessel which had a base pressure of $\sim 10^{-5}$ Torr. Gas fill pressures ranged from 5 to 200 mTorr of hydrogen, deuterium or helium depending upon the desired plasma conditions. The parameters of the plasma contained in the theta pinch at the moment of electron beam injection were determined by the preionization sequence. In order to produce a partially ionized plasma with $n_p \approx (0.5 - 5) \times 10^{14}/\text{cm}^3$, the discharge tube was filled to a gas pressure of 50 - 200 mTorr, and the Z discharge, powered by a 1 μ f capacitor bank charged to 30 kV, was fired only a few μ s before the theta pinch. To produce a highly ionized plasma the tube was filled to 5 - 10 mTorr and the Z discharge was fired $\sim 20 \mu$ s before the theta pinch. Access to the beam generator required a ~ 1 m long drift section between the anode foil and the entrance to the theta pinch coil. The magnetic guide field at the cathode anode gap extended over this distance. To insure that this drift region was highly ionized at the time of beam injection, the primary Z discharge electrodes were the anode foil and electrodes placed just before the theta pinch entrance, as illustrated in Fig. 2. Shortly after breakdown in this drift region, the ionizing discharge within the

theta pinch tube was struck from the theta pinch entrance electrodes to the Faraday cup - calorimeter (see below) which terminated the beam-plasma interaction region about $1/2$ m inside the end of the theta pinch tube. In some of the highly ionized plasma experiments, a 3 kJ low inductance capacitor bank was switched into the theta pinch coil, the ringing discharge of which preheated the plasma for subsequent further heating and compression by the theta pinch discharge. Figure 3 presents a sample oscilloscope trace of the H_{β} light from the plasma in the discharge tube for the highly ionized case.

For the bulk of the work to be presented here, a typical electron beam pulse launched from the diode was 2 - 3 kJ. Of this energy $\sim 75\%$ actually entered the theta pinch, the loss occurring mainly at the transition between the slow guide field and the fast theta pinch field regions. Within our shot-to-shot reproducibility, $\pm 15\%$, all of the beam energy injected into the theta pinch was collected by the Faraday cup - calorimeter $3\frac{1}{2}$ m downstream. The latter diagnostic, of the type described by Pellinen,⁶⁴ allows beam current and total beam energy to be determined. Surveys with witness plates at various axial locations within the discharge tube showed the beam to maintain its initial cross-sectional area (e.g., 40 cm^2 with the $7\frac{1}{2}$ cm diameter cathode). For example at the axial position of the laser diagnostic it was typically distorted into an elliptical form ($\sim 3\text{ cm} \times \sim 6\text{ cm}$) with its major axis in a horizontal plane (the plane of the theta pinch slot), and displaced upward and toward the theta pinch slot 1 - 2 cm.

Studies of the beam produced x-ray spectrum and angular dependence from a titanium strip in the guide field region indicated that the

beam had an angular spread of ~ 1 radian.²⁴ Scattering in the 0.0025 cm titanium anode can account for only a small portion of this ($\sim 1/3$ radian at the 600 keV level used in those studies). Therefore, we postulate that the angular spread was caused by beam interaction with the plasma near the anode foil, or by magnetic field nonuniformities due to, for example, joints in the guide field coils.

The electron beam was injected into the plasma 1 μ s after peak current was achieved in the theta pinch coil in order to allow the plasma to expand to a reasonably uniform radial profile. This tended to maximize the electron beam energy which could be injected. In the fully ionized plasma case, this also allowed the electrons and ions to equilibrate. At the time of beam injection, electron and ion temperatures were determined to be 2 - 3 eV, the former by Thomson scattering and the latter by measuring the Doppler broadening of the H_{α} radiation. In the partially ionized case the density was determined by an absolute calibration of the continuum intensity using the model described by Griem,⁶⁵ and by Thomson scattering when the density was high enough ($\geq 10^{14}/\text{cm}^3$).

The key measurements of plasma electron density and temperature after beam injection into the plasma were made by Thomson scattering⁶⁶ of ruby laser light (6943 Å). The laser had a peak power of 400 MW and a pulse width of 30 ns (fwhm). The scattering volume was a 1 - 1 $\frac{1}{2}$ cm long by 3 mm diameter cylinder of plasma centered on the axis of the theta pinch tube 1 $\frac{1}{2}$ m from the entrance. The scattering vector was transverse to the tube axis and the applied magnetic field direction so that $f(v_{\perp})$ was measured. Side arms in the glass tube which passed

through the theta pinch coil were used for the laser input and dump. The scattered light was collected via a third side arm at 90° to the other two. Stray light was reduced by having a thin sheet of anodized stainless steel attached to the discharge tube wall opposite the scattered light collection port. The scattered light was analyzed with a 5 channel polychromator consisting of a $1/2$ m spectrometer, 23 \AA spectral width fibre bundles and (RCA 7265) photomultiplier tubes. The entire analyzing system was heavily lead shielded to eliminate signals due to hard x-rays from the electron beam. Optical and electrical design parameters of the scattering system are available elsewhere.⁶⁷ The relative sensitivities of the scattering channels were determined using a Tungsten lamp having a known profile, and with the continuum from the plasma before and after beam injection. The absolute calibration was then determined for the channel on the laser line center (6943 \AA) by Rayleigh scattering from nitrogen gas. Figure 4a shows a typical scattered light signal on one of the channels when the plasma was partially ionized helium. The large initial signal occurred during beam injection. It was optical continuum during the beam-plasma interaction, not x-rays. This large background signal made density and temperature measurements by laser scattering impossible until about 70 ns after the start of beam injection. Figure 4b shows a typical scattering signal in the highly ionized case. The continuum radiation increased here as well, but only a small amount. Thus, in this case the increase served as a marker for the time of arrival of the beam at the laser scattering port. However, it did not prevent density and temperature measurements by laser scattering during the beam pulse. Figure 5 shows the range of densities and

temperatures obtained in one sequence of discharges of the Z discharge-theta pinch system in which the initial fill was 10 mTorr hydrogen (6.7×10^{14} atoms/cm³). Although the density varied from $\sim 6 \times 10^{14}$ cm⁻³ to $\sim 4 \times 10^{15}$ cm⁻³ the temperature remained in the narrow range of 2.2 - 3.2 eV. The large density variation was probably due to nonreproducible desorption of gases from the glass tube walls during the early stages of the theta pinch discharges, and/or nonreproducible compression of the resultant plasma by the theta pinch. The latter could also explain the previously mentioned $\pm 15\%$ variation in beam energy injected into the theta pinch.

Visible light measurements were made on the plasma discharge using 1/4 m and 1 m monochromators together with photomultipliers. For example, in partially ionized helium plasmas, the time history of He-I (4922 Å) and He-II (4686 Å) lines were observed to determine the rate of energy deposition in the plasma during the beam pulse.²⁴ The 1 m monochromator was used to obtain the Doppler broadened H_α (6561 Å) line width in the highly ionized hydrogen plasma. Stark and Zeeman line broadening were small for our plasma conditions, and resonant charge exchange neutrals emitted easily observable levels of Doppler broadened radiation. The line width was measured by sampling 0.3 Å width segments of the line on successive plasma discharges, three or more discharges each wavelength. The result of this measurement is shown in Fig. 6. Also shown in the figure is the instrument profile as measured separately with a discharge tube source. The line broadening, assuming Gaussian profiles, is about 0.54 Å, which yields an ion temperature of ~ 3 eV at the time of injection of the electron beam. Approximately equal electro

and ion temperatures is consistent with collisional relaxation times for our conditions. These measurements were made ~ 3 m from the entrance to the theta pinch coil.

Two different types of magnetic diagnostics were used during various phases of this work. Local magnetic field measurements were made in the highly ionized plasma case with a 3 mm diameter, 6 turn pickup loop mounted on the end of a 3 mm diameter solid copper outer conductor 50 Ω coaxial cable. The loop was moved vertically across the plasma on successive shots inside a 1.25 cm diameter, 3 mm wall quartz tube which extended all the way across the discharge tube on all shots. In this way the plasma and beam perturbation by the probe housing was the same on all shots. Silicon dielectric fluid within the quartz tube served to suppress electrical discharges within the tube. The presence of the probe housing within the discharge tube (~ 3 m from the entrance to the theta pinch coil) was found to have negligible effect on the plasma density and temperature.

The second type of magnetic diagnostic device was a diamagnetic loop, positioned around the glass discharge chamber, which measures the change in total enclosed axial flux. Because of the large voltages induced in the loop by the theta pinch discharge, it was necessary to connect the loop in series with a multiturn, small diameter compensating coil located between the discharge tube and the theta pinch coil. Because of the large inductance of the resulting electrical circuit, the rise time of the loop circuit was $\sim 1/2$ μ s. Integration time constants of 5 and 10 μ s were used. One such loop was located $\sim 1/2$ m inside each end of the theta pinch coil (see Fig. 2).

IV. EXPERIMENTAL RESULTS

A. Highly Ionized Case

Several different experimental runs were taken injecting the electron beam into the highly ionized hydrogen plasma. In the first case to be discussed, a 60 - 75 kA peak current, 70 ns (fwhm current pulse), ~ 2 kJ beam reached the Faraday cup-calorimeter. Cathode-anode gap peak voltage was 1.0 MeV, and the beam cross section was $\sim 40 \text{ cm}^2$. Figure 7 shows plasma density vs temperature data from Thomson scattering for this run. This figure includes scattering data taken from 40 to 350 ns after the arrival of the beam front at the scattering port. The data points shown in Fig. 5, obtained by firing the full system with the exception of the electron beam, were taken interspersed among the beam shots in Fig. Therefore, they are representative of the plasma into which the beam was injected. Note that the density range covered by the prebeam plasma data ("prep shots") and the beam data is virtually the same. It is clear in Fig. 7 that the temperature is strongly density dependent, with the higher density data clearly showing the lowest temperatures, and vice versa, even though the scatter is substantial. (The curve is simply to guide the eye.) Relative errors in these data points are typically $\pm 10\%$ in both density and temperature. In Fig. 8, the temperature as a function of time is plotted. As a result of the functional dependence of temperature on density, the data has been divided into three density ranges based upon the results shown in Fig. 7: $(7 \pm 3) \times 10^{14}/\text{cm}^3$, $(1.5 \pm .5) \times 10^{15}/\text{cm}^3$ and $(3.1 \pm 1.0) \times 10^{15}/\text{cm}^3$. The curves drawn for the highest density case will be discussed in the next section. There appears to be no real trend over the time period covered. This is in

contrast to our previously published results²⁵ from a different series of shots, in which rapid post beam cooling seemed to occur. Given the scatter in the present data, the discrepancy is probably due to the small number of shots in the previously published run. The lack of cooling is consistent with the fact that even in the 17 eV shot, electrons moving at the thermal velocity would take 1 μ s to travel half the length of the discharge tube. However, the present data does tend to verify our previous contention that most of the heating occurs in the early part of the beam pulse. The data from the previously published run are included in Fig. 8 in the appropriate density grouping for comparison.

The series of shots just discussed were performed with the five Thomson scattering channels placed symmetrically in wavelength space around the line center at the exit plane of the polychromator. Thus, channels 1 and 2 were located on the red (longer wavelength) side of 6943 Å, 3 was centered on 6943, and channels 4 and 5 were on the blue (shorter wavelength) side. This allowed a slight shift between the line center in prep shots and beam shots to be observed. Such a shift should exist since the beam leaves behind plasma currents in the r, θ plane as well as in the z direction when it exits the plasma.²⁵ If the beam plasma system were azimuthally symmetric, the currents in the r, θ plane would be purely azimuthal and the plasma electron distribution would have a drift in the theta direction if the current is due to electrons. Figure 9a is an idealization of the actual unsymmetric geometry showing the scattering volume, the beam position on a typical shot, and the diamagnetic drift direction. Since the beam cross section was not circular

the system was even less symmetric than shown. Figure 9b shows sample prep shot and beam shot scattering data to illustrate the relative change between a slight blue side enhancement in the prep shot case to a slight red side enhancement for a beam shot. The blue side enhancement in the case of prep shots is a geometric effect determined by such things as the precise placement of the fibre bundles in the exit plane of the polychromator. Line center, 6943 \AA , is taken to be at the average line center obtained from the prep shots assuming the line shape is Gaussian. The calculation is illustrated in Appendix A. A shift of the profile toward the red side during beam shots implies a mean electron velocity vector $\langle \underline{v} \rangle$ such that $\underline{k} \cdot \langle \underline{v} \rangle$ is negative, where \underline{k} is the scattering vector, the direction of which is shown in Fig. 9a.

Figure 10 shows the observed line center for the beam shots of Fig. 8 as a function of plasma density and temperature, together with the same information for the prep shots of Fig. 5. Errors in the observed intensities produce a typical uncertainty in the deduced line center in each shot of approximately $\pm 1 \text{ \AA}$. This is consistent with the calculated standard deviation for the prep shot line centers of 0.93 \AA . Figures 10a (line center vs density) and 10b (line center vs temperature) show no apparent density and temperature dependence for the line center position in the prep shots. On the other hand, for beam shots, Figs. 10a and 10b show possible trends to greater line center for lower density and for higher temperature, respectively.

For the geometric situation shown in Fig. 9a, we might expect the drift velocity, if it is a result of plasma electron diamagnetic current flow, to be more evident in the lower part of the scattering

volume than the upper assuming symmetric plasma motion around the beam axis. This is because the electron drift should be a minimum near the middle of the beam heated plasma - i.e., near the beam axis. Therefore, a series of beam and prep shots were performed looking only at the lower half or only the upper half of the scattering volume. The results for these cases are shown in Fig. 11. The line center as a function of temperature and density for the upper half of the scattering volume, Fig. 11a and b, appears completely random relative to the prep shots. This might be expected since the beam axis moved around from shot to shot relative to that volume. However, the beam axis was always above the lower half of the scattering volume, and there beam shot line centers were very consistent, as shown in Figs. 11c and d. (Note that the shift in average line center for prep shots included in Fig. 11 relative to the full scattering volume prep shots in Fig. 10 is believed to be due to differences in the upper and lower halves of the fibre bundles. Thus, it is the relative shift between beam and prep shots which is of interest here.)

We note that a 3 \AA line center shift implies a drift velocity of $1.3 \times 10^7 \text{ cm/sec}$. At 10^{15} cm^{-3} density, this would imply a plasma electron current of $\geq 2 \text{ kA/cm}^2$. This is an order of magnitude higher than we would expect from plasma diamagnetic currents, or residual net current density after beam passage through the plasma.²⁵ However, any lack of symmetry in the interaction, or residual radial electric fields, might cause gross plasma motion which would not have currents associated with it. Extreme asymmetries of the type suggested by VanDevender, et al.,²¹ as an explanation for apparent drift velocities of $\sim 10^8 \text{ cm/sec}$

in neutral gas experiments would not be expected in our high density plasma case. However, the magnetic field profiles to be discussed shortly do suggest the presence of asymmetries which may account for our observed drift.

With only two channels on each side of line center in this run, tails in the electron distribution function observed in the previously reported run²⁵ could not be observed. In that run, one channel was centered at 6943 Å and the remaining four channels were spaced out on the blue side. Recalculation of the density for those experiments gives $(1 \pm 0.5) \times 10^{15}/\text{cm}^3$ rather than the previously reported $2 \times 10^{15}/\text{cm}^3$. That run also included a limited number of shots with deuterium, and evidence for tails on the electron distribution function during the beam pulse, similar to those reported in hydrogen,²⁵ was observed.

Since data was taken with one or two diamagnetic loops (as described in Sec. III) on most of the above shots, it is of interest to compare the Thomson scattering results with the diamagnetic loop signal amplitudes. Since the compensating coil required in our loop circuit makes it a few hundred nanosecond rise time diagnostic, a shot by shot comparison with the "early time" Thomson scattering results is not justified. Therefore, we shall only consider the average signal amplitudes for the entire run. In order to obtain a temperature-density product from the diamagnetic loop signal, it is necessary to know the heated cross-sectional area, A_h , since for a simple loop (uncompensated)

$$\Delta(n_p \epsilon_{\perp}) = \frac{B_o V_{dl} \tau}{\mu_o A_h (1 - R_L^2/R_w^2)} \quad (\text{MKS units}). \quad (12)$$

In this equation ϵ_{\perp} is the sum of electron and ion transverse energies per particle, B_o is the applied magnetic field, V_{dl} is the observed voltage, τ is the diamagnetic loop circuit integration time constant, and R_L and R_w are the loop and conducting wall radii, respectively. The average signal V_{dl} was 9 V (with a 20% standard deviation), $\tau = 5.6 \mu s$, $B_o = 0.4 \text{ W/m}^2$ and $(1 - R_L^2/R_w^2) = 0.4$. Taking the beam cross sectional area of 40 cm^2 gives $\Delta(n_p \epsilon_{\perp}) = 6 \times 10^{15} \text{ eV/cm}^3$, or 60 eV per electron ion pair at $10^{15}/\text{cm}^3$ density. However, we will very shortly see that at least 100 cm^2 is a more reasonable estimate of the heated cross-sectional area, giving 24 eV per electron ion pair at $10^{15}/\text{cm}^3$. From Figs. 5 and 8 we see that the electron temperature rise according to Thomson scattering is only $\sim 3 \text{ eV}$. Even assuming equal energies in electrons and ions, the discrepancy here is a factor of 4, remarkably close to the factor of 6 observed by Arzhannikov, et al.,¹⁷ at $\sim 10^{14}/\text{cm}^3$ density. This may be due to energy in rotational drift motion which was noted as a possible explanation for the larger than expected liner center shifts. The presence of an energetic tail on the electron distribution function, as predicted by e-e instability theory,^{30,33} may also explain the discrepancy. Finally, it may be the residual effect of beam diamagnetism.⁵⁷ If it is a tail, it must be of order 500 eV or more in order not to thermalize with the main distribution in 300 - 400 ns by collisions.

The heated plasma area was obtained in a separate experimental run in which a 40 - 50 kA peak current, 900 keV peak voltage, 60 ns beam

was injected into the theta pinch. The plasma density was $(1 \pm .5) \times 10^{15}/\text{cm}^3$ and the temperature ~ 2.5 eV. [The laser scattering system was not in operation during this run. These values for density and temperature were obtained in a series of prep shots taken after the probe shots were completed. Prep shots were taken both with and without the probe housing (and probe) in place. There was no significant difference.] The magnetic probe, as described in Sec. III, located ~ 3 m into the theta pinch (and $1/2$ m in front of the second diamagnetic loop) was used to measure local magnetic field changes resulting from the beam plasma interaction. Figure 12a shows the interaction geometry at the probe port for this run. (The beam position was obtained using solid targets in the beam path at the probe port as well as by x-ray pinhole photography on the probe housing and on a coarse grid of Tungsten wires placed at the same axial position.) Figure 12b shows a typical Faraday cup waveform for time reference. The results for the change in axial magnetic field (ΔB_z) and the horizontal field (B_x) are shown in Figs. 13a and 13b. Note that in an axisymmetric experiment, B_x would be the azimuthal field component, B_θ . B_x was obtained from the probe signal, dB_x/dt , by the standard technique of a passive RC integrator (having a 2 μs time constant) at the oscilloscope. However, it was necessary to display dB_z/dt and graphically integrate the oscillograph to obtain ΔB_z because of the voltage induced in the probe by the theta pinch. These curves have been published in our previous article,²⁵ but our discussion here will be greatly facilitated by having them at hand.

At the moment our interest is the diamagnetic area in Fig. 13a after the beam has passed. (A diamagnetic ΔB_z signal is negative in the

figure.) We note that it is considerably larger than the region in which current is flowing, as indicated by the B_x signals in Fig. 13b. Moreover, since the beam geometry, obtained from targets and x-ray pinhole photography (Fig. 12a), and the B_x signals both indicate that the probe is measuring ΔB_z across a chord in the heated plasma rather than a diameter, we infer a disturbed area of 100 - 125 cm² after the beam pulse (see the profiles at 125 or 175 ns).

The 100 gauss depth of the diamagnetic well implies a $\Delta(e_{\perp})$ of ~ 20 eV per electron-ion pair for $10^{15}/\text{cm}^3$ density. Diamagnetic loop amplitudes corresponding to about half this temperature change were observed on these shots (assuming 100 cm² heated cross section). These diagnostics imply ~ 50 J/m of beam energy deposited in the plasma, assuming isotropy, for a coupling efficiency of 3%/m.

It is interesting to note that the disturbed cross-sectional area indicated in Fig. 13a even as early as 50 ns is considerably larger than the area in which the beam current (and, therefore, the plasma current) is flowing. The speed of cross field energy transport implied by this is ≥ 40 cm/ μs , a value considerably larger than that obtained in an ordinary turbulent heating experiment by Aranchuk, *et al.*⁶⁸ Thus, not only does beam heating of a plasma avoid skin effect difficulties of ordinary turbulent heating, it also rapidly heats the surrounding volume, possibly by wave energy transport.^{68,69}

Turning now to the B_x profiles, there are several characteristics of interest. Firstly, as already noted, the net current implied by this profile during the beam pulse locates the beam in a position consistent with target and x-ray diagnostics (i.e. above the discharge tube

axis by ~ 2 cm). Secondly, the net current position shifts from 2 - 3 cm off axis to very nearly on axis at the end of the beam pulse. The reason for this is not known, although it may be reflecting a movement of the beam as its current drops from its maximum to zero at the end of the pulse. The magnitude of the net axial current is also of interest. Taking into account the system geometry (Fig. 12a), ~ 500 A of net current is implied, i.e., $I_b/100$. This is a factor of 3 greater than would be predicted by sharp beam boundary theory,^{27,37} and a factor of 1000 greater than for the more realistic beam radial density profiles of Küppers, et al.,⁴⁰ ignoring return current damping.³⁷ Assuming classical resistivity, the damping time T (see Sec. IIA) for a 3.5 cm radius, 2.5 eV plasma is 7 μ s. Thus, a net current density of $\sim 1\%$ might be expected in ~ 70 ns. The fact that it appears virtually instantaneously (by the end of the beam rise time), and then changes very slowly during the main part of the beam pulse appears to be consistent with a collision frequency ≥ 10 times classical at first, and perhaps 2 - 3 times classical during the next 50 ns. (T increases to ~ 20 μ s at 5 eV.) These collision frequencies are consistent with values obtained by calculating the heating rates implied by the magnetic profiles.²⁵

B. Partially Ionized Case

The use of a partially ionized plasma adds the possibility of substantial ionization and radiative energy losses to the other processes associated with IREB-plasma interaction. If these processes occur fast enough in the target plasma, they must be taken into account in assessing the energy transferred from the beam to the plasma. For example, the ionization energy for hydrogen (H_2) is $\sim 15^{1/2}$ eV and it is ~ 25 eV in

helium. In fact, twice these minimum energies are required since line radiation energy losses must be considered. In previously reported results²⁴ from the present experiment, a ~ 30 kA, 550 keV, 70 ns beam was injected into a $5 \times 10^{13}/\text{cm}^3$ density helium plasma with neutral helium density $n_0 \cong 3.5 \times 10^{15}/\text{cm}^3$ (100 mTorr pressure). The applied magnetic field throughout the experimental system was 5 kG in this run, as well as in the partially ionized cases to be discussed below. The plasma density and temperature observed after beam passage were $\sim 7 \times 10^{14}/\text{cm}^3$ and up to 5 eV. Using these numbers and 40 eV to produce each electron-ion pair to estimate the energy input, we obtain $n_p (3/2 kT_e + 40)/70 \text{ ns} \approx 5 \times 10^{23} \text{ eV/cm}^3 - \text{sec}$ as the average energy deposition rate. This represents a coupling efficiency of $\sim 3\%/m$ assuming a heated plasma cross section equal to the beam area (20 cm^2). If the heated area is $2^{1/2}$ that area as was the case for the highly ionized experiments discussed in Sec. IIA, the implied coupling efficiency is $\sim 7\%/m$. (The factor of $2^{1/2}$ is only conjectural in the partially ionized experiments since no magnetic probe scans were taken.)

Two additional experimental runs were taken in which the beam was injected into partially ionized helium at 100 mTorr pressure. In the first, a 1 MeV, 50 kA peak current, 5 cm diameter beam of 70 ns duration was injected into an $8 \times 10^{13}/\text{cm}^3$ density, 2 eV plasma (the " 8×10^{13} case"). In the second run, the beam was 900 keV and 40 kA peak current, and the initial plasma density was $4 \times 10^{14}/\text{cm}^3$, with the remaining parameters being the same (the " 4×10^{14} case"). Figures 14 and 15 present the plasma electron temperature and density obtained by Thomson scattering. The time interval covered was 70 - 450 ns after

beam front arrival at the scattering port, as defined in Fig. 4a. (As discussed in Sec. III, scattering during the beam pulse was not possible due to the high level continuum light during the beam pulse.)

The data in Figs. 14 and 15 both show the following characteristics: 1.) The plasma density rises from its initial value to $\sim 10^{15}/\text{cm}^3$ by the end of the beam pulse, and 2.) the temperature is 6 - 8 eV just after the beam, and falls over ~ 100 ns to about 3 eV where it stabilizes.

These two runs give average energy deposition rates, $n_p(3/2 kTe + 40)/70$ ns, slightly higher than the previously reported case,²⁴ namely $(7 - 12) \times 10^{23}$ eV/cm³ - sec. Because the injected beam energy for these runs was ~ 3 times that of the previous case, the resulting coupling efficiencies for these higher density cases were lower, namely $\sim 2\%/m$ assuming only the beam area is heated, and $\sim 5\%/m$ if $2^{1/2}$ times that area is heated, as previously discussed.

In order to understand these results a one dimensional ionization and heating model, similar to that used previously²⁴ was constructed. It is discussed in detail in Appendix B. To summarize, energy is deposited resistively in the plasma at a rate ηj^2 , where η is the plasma resistivity and j is the return current density in the plasma (assumed equal to the beam current density). The resulting changes in plasma density and temperature are followed in time by solving a coupled set of differential equations (Eqs. (B1 - B7)) for the densities of neutral, singly, and doubly ionized helium, and for the temperature of these species. The principal energy loss processes included are ionization and line radiation, although Eq. (B5) for the electron energy contains several others. Rate coefficients are temperature dependent as

appropriate^{70,71} (Eqs. (B11) and (B12)). The quantity η includes classical (Eq. B8), as well as anomalous resistivities due to ion acoustic and e-e mode turbulence (Eqs. B9 and B10), which are discussed in Appendix B.

The model ignores such plasma dynamic and kinetic effects as expansion and end loss. This is equivalent to assuming the plasma to be spatially uniform. This should be consistent with the low observed temperatures, the short timescale of interest, and classical transport and thermal expansion.

The plasma current density is assumed to have a 10 ns e-fold rise time, a 70 ns width (fwhm), and a 10 ns e-fold fall time.

Results obtained from this model are shown together with the experimental data in Figs. 14 and 15. We see that the theoretical plasma temperature shoots up at early time (Figs. 14a and 15a). This is because there are relatively few electrons to share the energy input. (This is enhanced by the inverse dependence of the anomalous resistivities on density, Eqs. (B9) and (B10).) The exponential dependence of ionization on temperature, Eq. (B11), means that only when the temperature is above ~ 10 eV will rapid ionization occur. This occurs in less than 10 ns in the 8×10^{13} case, and the density rises rapidly, doubling in 25 ns and redoubling in less than 50 ns in this case (Fig. 14a). The rate of energy input then decreases (since the anomalous resistivities decrease) and the energy is divided among more electrons, depressing the temperature. By the end of the beam pulse in the 8×10^{13} case, the temperature is only $1/3$ of its maximum value. At this time, the energy input stops (since j decreases to zero), the temperature rapidly decreases to less

than 10 eV and further ionization ceases. In the 4×10^{14} case, the temperature peaks at a much lower value. Therefore, the ionization proceeds at a slower rate than in the first case, and the density when the beam (and heating) pulse is over is only three times the initial value. We note that the plasma conditions after the beam pulse are insensitive to small changes in the initial conditions. For example, decreasing the initial electron density to $3 \times 10^{14}/\text{cm}^3$ changed the density by 2% and decreased the temperature by 1% at $t = 100$ ns. This was in spite of the fact that the maximum temperature, at $t = 35 - 40$ ns, increased by 15%.

Comparing the theoretical and experimental results, we see that the theoretical density rises too quickly in the 8×10^{13} case and too slowly in the 4×10^{14} case. Agreement with the final value is quite good in the lower density case, but it is low in the higher density case. In both cases, the experimental temperatures appear to drop to their asymptotic values (~ 3 eV in both cases) much more quickly than the model predicts. This is probably a result of either nonclassical energy transfer to ions (possibly due to the presence of ion acoustic turbulence), or nonclassical radial energy transport (as by waves). For example, if half the plasma energy at ~ 100 ns is apportioned to ions (which are ≤ 1 eV from classical heating), temperature agreement would be quite good at that time. Other processes for plasma energy loss (such as via impurity radiation, assuming of order 1% Nitrogen, Carbon and/or Oxygen) are too slow to account for the necessary electron cooling rate.

Since we have used only resistive heating in our model, it is reasonable to ask what will happen to these results if nonresistive

heating by the electron-electron instability is added. In Sec. V, we shall see that direct heating from this instability can be expected to be greatest near the beginning of the beam-plasma interaction for our experimental conditions. Therefore, in the 4×10^{14} case, we have arbitrarily increased \dot{Q} in Eq. (B5) by 10^{24} eV/cm³ - second for 10 ns from $t = 6$ to 16 ns. The resultant density at 100 ns was 10% higher, and the temperature, although higher at 25 ns, was virtually the same (2% lower) at 100 ns. We have not carried the numerical calculation beyond 200 ns since its 1-dimensionality and lack of plasma transport mechanisms limit its validity to short times.

A final numerical result to be noted is the deposited energy per electron-ion pair. From Fig. 14 (8×10^{13} case), the plasma energy density, $\frac{3}{2} n_p k T_e$, is $\sim 1.5 \times 10^{16}$ eV/cm³. An energy of 5.4×10^{16} eV/cm³ was deposited (resistively) in that numerical run. Thus, approximately 4×10^{16} eV/cm³ remains, implying 40 eV was required to produce each electron-ion pair, as previously assumed. (The approximate equality of the ionization and excitation rate coefficients, Eqs. (B10) and (B12), explains the need for about 1.6 times the 24.6 eV ionization energy for helium.)

In addition to Thomson scattering measurements, we have observed microwave emission in X-band (8 - 12 GHz) and optical emission of helium I and II lines, and have made diamagnetic loop measurements. The microwave measurements revealed strong emission near the relativistic cyclotron frequency corresponding to the diode voltage and the applied magnetic field (5 kG). This emission occurred at the beginning of the beam pulse and had ≤ 20 ns full width at half maximum. The optical line

emission, however, could not be accounted for by assuming all the energy deposition occurred during this time. A more uniform deposition rate was required.²⁴ This leads to the conclusion that the X-band radiation was not associated with the bulk of the energy deposition.

Taking up the diamagnetic loop results now, Fig. 16 shows a typical diamagnetic loop signal (after subtracting out the uncompensated portion of the induced voltage from the theta pinch) for the 8×10^{13} case. (It is representative of the other case as well.) Very similar amplitude and shape signals were obtained on the two diamagnetic loops when both were used, indicating the uniformity of the interaction over the 4 m length of the interaction region for this, the partially ionized case, as it was in the highly ionized case. (The only difference was that the diamagnetic loop signal at the upstream end of the system sometimes showed oscillations of the type to be discussed below.) Because of the slow response time of the diamagnetic loop circuit the signal voltage is not simply related to the instantaneous plasma energy density as measured by Thomson scattering. We assume the theoretical density and temperature time histories as shown in Fig. 14 to be correct, and approximate the product $n_p k T_{\perp}$ by a triangular shaped transverse energy pulse of full width 100 ns and peak of 6×10^{13} eV/cm³ at $t = 50$ ns. We then calculate the expected oscilloscope voltage as a function of time V_s using the circuit shown in Fig. 17a to approximate the diamagnetic loop circuit. With $L = 22$ μ h and $RC = 10$ μ s, the result is given in Fig. 17. The signal peak is only a factor of two smaller than the observed signal in Fig. 16.

In Fig. 17, we calculated the expected diamagnetic loop signal from a triangular shaped (in time) pulse of diamagnetism which was chosen as an approximation to the plasma diamagnetism implied by Fig. 14. However, it could just as well represent beam diamagnetism since $n_b \approx 4 \times 10^{11}/\text{cm}^3$ ($2 \text{ kA}/\text{cm}^2$) would require only 150 keV transverse energy per beam electron to produce the $6 \times 10^{16} \text{ eV}/\text{cm}^3$ peak we used in Fig. 17. In the final series of shots to be discussed in this paper, 12 cm^2 and 40 cm^2 beams at $\sim 900 \text{ keV}$ were injected into partially ionized hydrogen at $\leq 5 \times 10^{13}/\text{cm}^3$ and $\sim 1 \text{ eV}$. The beam current density was in the range ~ 1.2 to $\sim 3.5 \text{ kA}/\text{cm}^2$ for the smaller area beam and was $\sim 1.2 \text{ kA}/\text{cm}^2$ for the larger beam. (Density and temperature as a function of time from laser scattering gave results quantitatively similar to the partially ionized helium data shown in Figs. 14 and 15. There were, however, too few shots at any given beam condition to draw a graph similar to those figures for these shots.) Figure 18 shows typical diamagnetic signals for these shots. In Fig. 19a we plot the amplitude of the diamagnetic loop near the calorimeter against the calorimeter energy. The smaller area beam shows a clear trend toward loop signal being proportional to propagated beam energy. (Note: since the beam voltage pulse duration was virtually the same for all shots plotted, only the current varies to produce the variation in beam energy.) The larger area beam does not show this trend.

In Fig. 19b, $n_p kT_{\perp}$ obtained from laser scattering is plotted against diamagnetic loop amplitude for those shots from Fig. 19a for which scattering data was taken. There is some indication here that plasma energy after the beam pulse and the diamagnetic loop signal are

correlated. As in the helium cases, the diamagnetic loop is indicating more than an order of magnitude more transverse energy than the laser scattering, presumably for the same reasons. The data of Fig. 19a suggests that beam diamagnetism cannot be ruled out as a contributing factor, at least for the smaller area beam. However, an equally allowable explanation is stronger beam-plasma interaction for the higher current density beams.

Returning to Fig. 18, we note that both signals show oscillations with the same period, probably the magnetosonic oscillations previously discussed.^{15,19,23,44,51} The more prominent oscillations on the diamagnetic loop signals here as compared to the helium shots (e.g. - Fig. 16) may be a result of the magnetosonic waves being damped by more collisions in the helium case.⁴⁴ In addition we see that the amplitudes are virtually the same, again indicating the uniformity of the interaction of the entire system length.

V. THEORETICAL CONSIDERATIONS

In this section we address the questions of what beam-to-plasma energy transfer mechanisms are expected under the conditions of our experiments, and how much energy we expect the beam to lose according to the appropriate theory. We first present a qualitative discussion of the most probable loss mechanisms (direct electron-electron two stream and return current heating), including their time dependent characteristics. These are subsequently applied to our experiments.

According to linear theory two types of waves are expected during IREB - plasma interaction. The first type corresponds to Langmuir waves:

excited by the electron-electron two stream instability (e-e mode) with wavelength of the order c/ω_p . We refer to the energy density of these waves as W_1 . The second type corresponds to ion acoustic waves, W_a , which can be excited when the induced return current drives electron-ion instabilities (e-i modes). An approximate criterion for the excitation of such instabilities is $v_d/c_s \gg T_i/T_e$ ($v_d > c_s$ if $T_i \ll T_e$), where $c_s = [k(T_e + T_i)M]^{1/2}$ and v_d is the plasma electron drift velocity relative to the mass M ions. Two energy transfer mechanisms are, therefore, possible. One is the direct interaction of the beam electrons in resonance with the waves W_1 (i.e., $\omega_p - c(\underline{k} \cdot \underline{p}/|\underline{p}|) = 0$ where \underline{p} is the beam electron momentum vector). The second is scattering of the plasma electrons forming the return current on W_a , which results in anomalously high resistance. In order to compute the energy transfer rates, the wave energy levels W_1 and W_a must be known. The computation of these levels has been the most controversial aspect of IREB plasma heating.

An extensive amount of work has focused on the determination of W_1 and the associated energy coupling length (ℓ) on the basis of convective quasilinear theory.^{28,29,31} Such considerations produced the length given by Eq. (4). As discussed in Sec. II experiments have shown this to be much too short. This is physically expected since for any parameters of interest, the magnitude of W_1 violates the assumptions of quasilinear theory.³³ An alternative possibility is that the amplitude W_1 is limited by nonlinear wave-wave interactions. The general idea of this concept is that beyond a certain level of W_1 , wave energy is transferred into a nonresonant region. A stationary state can then be achieved

where the energy transfer from the beam to the (resonant) Langmuir waves is balanced by the transfer of wave energy to the nonresonant region. As a result, W_1 is maintained at a sufficiently low level while dissipation occurs only in the nonresonant regions. The energy loss rate for the beam electrons is then proportional to $2\delta W_1$, where δ is the instability growth rate given by Eq. (3). Early attempts to apply these concepts to IREB plasma experiments^{28,31} were confined within the framework of validity of weak turbulence theory (i.e. the real part of the frequency obeys the linear dispersion relation). These efforts still failed to reconcile the differences between theory and experiment. However, Papadopoulos³³ showed that for any reasonable parameters applicable to present day intense beam plasma interaction experiments the weak turbulence theory is not valid and inclusion of nonlinear frequency shifts is important. It was shown that when $W_1/n_p kT_e > (v_e/c)^2$, the wave spectrum becomes unstable to a secondary instability similar to the oscillating two stream instability (OTSI).^{33,72} (Within this context the instability is known also as the modulational or modified decay instability.) This process transfers energy to electron plasma waves with lower phase velocities (shorter wavelengths) and associated low frequency ion waves. The lower phase velocity plasma waves can be linearly Landau damped by the tails of the plasma electron distribution function. Note that these wave processes viewed in configuration space correspond to plasma waves trapped in low density regions and have been given the name of plasma solitons, cavitons and spikons.⁷³ It has been shown⁷⁴ that they are equivalent representations of the OTSI. It should also be noted that among the new concepts introduced by the strong turbulence

theory is the possibility of exciting ion waves W_a created directly by the ponderomotive force exerted on the plasma by W_1 even in the absence of return current driven instabilities (e-i modes).

On the basis of this model, the details of which are available elsewhere,³³ the time sequence of events is as follows. Upon injection of the beam in the plasma the waves W_1 grow rapidly until they reach a level such that their removal from the instability region is faster than the e-e instability growth. This is given by (see Eqs. (25-26) of Ref. 33)

$$\frac{W_1^{\max}}{n_p k T_e} = \frac{M}{m} \left(\frac{\delta}{\omega_p} \right)^2 \Lambda^2, \quad \Lambda = \ln \left[\frac{\delta}{\omega_p} \left(\frac{M}{m} \right)^{1/2} \frac{n_p k T_e}{W_2(t=0)} \left(\frac{W_1^{\max}}{n_p k T_e} \right)^{1/2} \right], \quad (13)$$

where M is the ion mass. They subsequently decay to Langmuir waves non-resonant with the beam electrons (W_2) and modified ion plasma waves (W_a). This is illustrated in Fig. 20. A quasistationary state can be established on the basis of the following arguments: The presence of finite amplitude ion waves W_a can produce an ac resistivity for waves near the plasma frequency with effective collision rate ν_H^* as discussed by Dawson and Oberman⁷⁵ and a dc resistivity^{33,76} with rate $\nu_o^* = \overline{k\lambda_D} \nu_H^*$, where $\overline{k\lambda_D}$ is the characteristic wave number Debye length product for the ion waves. When

$$\nu_H^* = 2 \delta, \quad (14)$$

the e-e instability is stabilized and the energy deposition rate via waves $d\epsilon_1/dt$ will be given by

$$\frac{d\epsilon_1}{dt} = \nu_H^* W_1 \left(1 + \frac{\partial \omega D}{\partial \omega} \right) = 4 \delta W_1, \quad (15)$$

where D is the dielectric function of the plasma. In addition to this, the presence of the dc collision frequency ν_o^* will provide an energy deposition mechanism due to the return current $j = n_p e v_d$. This will be given by

$$\frac{d\epsilon_2}{dt} = \eta^* j^2 = \frac{4\pi \nu_o^*}{\omega_p^2} j^2 = \frac{4\pi}{\omega_p} \frac{2 \delta}{k \lambda_D} j^2. \quad (16)$$

Notice that if the Coulomb collision rate ν_{cl} is greater than ν_H^* or ν_o^* , then it replaces them in these arguments. Furthermore if an e-i instability is present, W_a and therefore the effective collision frequencies might have to be determined by other considerations.²⁸ The energy levels W_1 and W_2 are determined by the condition that the ion waves are marginally stable. This gives [Ref. 33 Eqs. (39-44)]

$$\frac{W_1}{n_p k T_e} = 4 \frac{\nu_H^*}{\omega_p} = 8 \frac{\delta}{\omega_p}. \quad (17)$$

It should be noted that these relations have been verified by computer simulations using particle and mode coupling codes.⁷⁷

We now proceed to apply these concepts to the present experiment.

In order to be more precise quantitatively we select first the case where the IREB ($n_b \approx 5 \times 10^{11}/\text{cm}^3$) was injected into a highly ionized plasma with density $(7 \pm 3) \times 10^{14}/\text{cm}^3$ and initial temperature $T_e \approx T_i \approx 3$ eV. For these parameters, e-i instabilities are not expected, since $v_d \ll v_e$. We consider the beam pulse shape shown in Fig. 21 and see if Eqs. (13-17) predict the energy absorption data and the field penetration timescale as measured by the laser scattering and magnetic probes. The time $\tau = 0$ is the time the beam front arrives at the particular diagnostic port. We compare the observation first with the approximate analytic results, and then the results of a numerical solution of the nonlinear equations.⁷⁷

For the parameters of this experiment and for the energy deposition during the initial stage we find from Eq. (13) that $W_1^{\max}/n_p kT_e = 0.32$. The actual energy loss of the beam is given by $\Delta \epsilon_o = W_1^{\max} \left(1 + \frac{\partial W D(\omega, k)}{\partial \omega} \right) \approx 2 W_1^{\max} \approx 1.36 \times 10^{15} \text{ eV/cm}^3$. This energy is delivered during a 5 ns time interval around $\tau = 20$ ns, since the instability does not start ($2\delta < v_{cl}$) until $\tau \approx 15$ ns. At this time both v_H^* and v_o^* reach a maximum and then relax towards their quasistationary values. For the case under consideration these are given by $W_1/n_p kT_e \approx W_2/n_p kT_e \approx 8\delta/\omega_p \approx 2 \times 10^{-2}$, $W_a/n_p kT_e \approx 10^{-4}$ and $\overline{k\lambda_D} \approx .1 - .2$ (for $\gamma = 3$ and $\bar{\theta} \approx 1/3$). With the above values we find that for the rest of the beam pulse the energy deposition rate due to wave damping, given by Eq. (15), is

$$\frac{d\epsilon_1}{dt} = 4.6 \times 10^{23} \frac{\text{eV}}{\text{cm}^3 - \text{sec}},$$

while the one due to the return current, Eq. (16), is

$$\frac{de}{dt} = 2.5 \times 10^{23} \frac{\text{eV}}{\text{cm}^3 - \text{sec}}.$$

The total energy lost by the beam according to this model is $\sim 3.5 \times 10^{18}$ eV/cm³. For a 40 cm² beam, this gives $\sim 1.5 \times 10^{18}$ eV/cm during the entire pulse. This is to be compared with $\sim 5 \times 10^{17}$ eV/cm deposited energy measured by laser scattering assuming 100 cm² heated plasma cross section, (Fig. 8a) and $\sim 2 \times 10^{18}$ from the diamagnetic loop average.

We have checked the conclusions of the simplified analytic model by numerically solving⁷⁷ the exact mode coupling equations which are derived in Ref. (33), including the effect of finite beam rise time and classical collisional damping. The results for the energy deposition, low frequency resistivity, and wave spectrum as a function of time are shown in Figs. 22-24. The analytic results are included for comparison and are seen to be consistent with the discussion we have presented. Note that the computational results for energy deposition (Fig. 22) do not include resistive heating contributions. From Fig. 23 we can see an early time resistivity which is more than an order of magnitude larger than classical, and a later time resistivity of about twice the classical value, as required to explain the magnetic probe results (Fig. 13). The high and low frequency wave spectra during the various stages of the interaction, shown in Fig. 24, demonstrate that modes with phase velocity in resonance with the beam (marked by +) dominate only at early time.

In the higher density highly ionized experiments for which results are shown in Fig. 8 [i.e., $n_p = (1.5 \pm .5) \times 10^{15}/\text{cm}^3$ and $n_p = (3.1 \pm 1) \times 10^{15}/\text{cm}^3$], $2.8 < v_{cl}$ for all time during the pulse assuming

that $T_e = 3$ eV and $\bar{\theta} \approx 1/3$. Therefore, we do not expect the e-e instability to be excited. For the case $(3.1 \pm 1) \times 10^{15} \text{ cm}^3$, as shown in Fig. 8c, classical heating by dissipation of the return current can account for the observed increase in temperature. However, this is not true for the $(1.5 \pm .5) \times 10^{15}/\text{cm}^3$ case. At this stage we can only speculate that perhaps some nonuniformity in the beam current density can produce a sufficient local heating at early time, to allow $2\delta > \nu_{cl}$ and the e-e instability to be excited.

We proceed now to examine the partially ionized results. For the $4 \times 10^{14}/\text{cm}^3$ case with a 40 kA, 900 keV beam, we have that the initial growth rate is given by $\delta = 3.8 \times 10^{-3} \omega_p$. Therefore, from Eq. (17) we obtain an energy delivered in the initial stages of the instability of $\Delta\epsilon_0 = 5 \times 10^{15} \text{ eV/cm}^3$. At this point we must consider the effect of substantial temperature changes due to heating and the increasing plasma density due to ionization of the $3 \times 10^{15}/\text{cm}^3$ neutrals present in the system. If we combine Eqs. (15) and (17), we obtain a wave energy deposition rate appropriate for this case

$$\frac{d\epsilon_1}{dt} = \frac{2 \times 10^{23} kT_e(t)}{(n_p(t)/4 \times 10^{14} \text{ cm}^{-3})^{3/2}}. \quad (18)$$

(In this equation, kT_e is an effective temperature, since there may be tails, as shown in Fig. 20.) In Fig. 15 we saw that the time for significant increase in density in this case is comparable to the pulse duration for initial energy deposition rates of order $10^{24} \text{ eV/cm}^3 \cdot \text{sec}$. Therefore, it is reasonable to assume small density change and take $n_p(t) \approx 5 \times 10^{14}/\text{cm}^3$. We can also approximate $kT_e(t)$ by 10 eV. This gives an "average" value for the wave energy deposition rate of

$$\frac{d\epsilon_1}{dt} \approx 1.5 \times 10^{24} \text{ eV/cm}^3 - \text{sec} ,$$

a result consistent with our use of Fig. 15 for guidance. Thus, the energy deposition via waves during the remaining beam pulse is $\Delta\epsilon_1 \approx 7.5 \times 10^{18} \text{ eV/cm}^3$. Using Eq. (16) to obtain a resistive energy deposition rate equivalent to Eq. (18), we obtain

$$\frac{d\epsilon_2}{dt} = \frac{1.6 \times 10^{17} j^2 (\text{A/cm}^2)}{(n_p/4 \times 10^{14} \text{ cm}^{-3})^{3/2}} , \quad (19)$$

$$\approx 5 \times 10^{23} \frac{\text{eV}}{\text{cm}^3 - \text{sec}} ,$$

the latter number being an average rate during the pulse. The resistively deposited energy, therefore, totals $\Delta\epsilon_2 \approx 2.5 \times 10^{18} \text{ eV/cm}^3$. Summing the three components, the energy deposition according to the present model comes to $1.0 \times 10^{17} \text{ eV/cm}^3$. Averaging this over the full beam pulse width (70 ns), we obtain an average energy deposition rate of $1.5 \times 10^{24} \text{ eV/cm}^3 - \text{sec}$, 30% greater than the value estimated for this case from Fig. 15 (including the 40 eV ionization energy and the $2^{1/2}$ area factor) in Sec. IVB.

Since the plasma conditions in the partially ionized cases allow the possibility of ion acoustic turbulence, we must consider the contribution which this instability may make to the heating. From the work of Zavoisky, et al.,⁷⁸ it is possible to obtain a value of the anomalous resistivity due to ion acoustic turbulence, η_{ia} , for $v_e > v_d > c_s$, where c_s is the ion sound speed, $(k(T_e + T_i)/M)^{1/2}$. This value, in a form appropriate for comparison with the coefficient of j^2 in Eq. (19), is

$$\eta_{ia} = \frac{1.8 \times 10^{17}}{(n_p/4 \times 10^{14} \text{ cm}^{-3})^{1/2}} \frac{\text{eV}}{\text{cm}^3 \cdot \text{sec} \cdot \text{A}^2} \quad (20)$$

Thus, it is virtually the same as the resistivity due to the e-e mode, implying negligible additional heating.

The final case to be discussed here is the one with an initial density of $8 \times 10^{13}/\text{cm}^3$ and temperature 2 eV. The beam was 1 MeV and 50 kA. At this low plasma density, the growth rate δ exceeds the collision frequency very early in the rise time of the current pulse. Therefore, we take half the beam maximum density ($6 \times 10^{11}/\text{cm}^3$) and $\nu = 2$ in order to obtain the δ to use in calculating $\Delta\epsilon_0$. We obtain $\delta/\omega_p \approx 2 \times 10^{-2}$ and $\Delta\epsilon_0 \approx 1.0 \times 10^{13} \text{ eV}/\text{cm}^3$. During the next stage of the heating $\delta/\omega_p \approx 3 \times 10^{-3}$. However, we now have the additional complication of a significant change in the plasma density and temperature during the course of the interaction. The wave and resistive energy deposition between 20 and 70 ns can be written

$$\Delta\epsilon_1 \approx 2 \times 10^{24} \int_{20}^{70} \frac{kT_e(t) dt \times 10^{-9}}{(n_p(t)/8 \times 10^{13} \text{ cm}^{-3})^{3/2}} \frac{\text{eV}}{\text{cm}^3}, \quad (21a)$$

$$\Delta\epsilon_2 \approx 2 \times 10^{18} \int_{20}^{70} \frac{j^2 dt \times 10^{-9}}{(n_p(t)/8 \times 10^{13} \text{ cm}^{-3})^{3/2}} \frac{\text{eV}}{\text{cm}^3}. \quad (21b)$$

From Fig. 14, we take $kT_e \approx 30 \text{ eV}$ as an average over that time interval, and approximate the density by $n_p(t) \approx 8 \times 10^{13} [1 + 0.12 t]$, where t is in ns. This gives

$$\Delta\epsilon_1 \approx 3 \times 10^{17} \text{ eV/cm}^3; \quad \Delta\epsilon_2 \approx 4 \times 10^{13} \text{ eV/cm}^3,$$

for a total predicted energy deposition of $3.5 \times 10^{17} \text{ eV/cm}^3$. Assuming uniform energy deposition over the 20 cm^2 beam area, this is a factor of ~ 3 greater than the value we would estimate from the results shown in Fig. 14 (including the 40 eV ionization energy and the $2^{1/2}$ area factor).

Again checking the possibility of ion acoustic resistive heating, the coefficient of j^2 in Eq. (21b) is a factor of 5 greater than the value of η_{ia} at $n_p = 8 \times 10^{13}/\text{cm}^3$, obtained from Eq. (20). However, $\eta_{ia} \propto 1/n_p$ whereas e-e mode resistivity is evidently proportional to $n_p^{-3/2}$. Thus, these resistivities are about equal at $4 \times 10^{14}/\text{cm}^3$, which is reached at about 50 ns. Since most of the contribution to $\Delta\epsilon_2$ is made by this time (because of the inverse dependence on density for both resistivities), and since $\Delta\epsilon_2 \ll \Delta\epsilon_1$, ion acoustic turbulence will again contribute only a small amount to the total deposited energy.

In Fig. 25, we plot the theoretically predicted energy deposition as a function of beam to plasma density ratio for the three cases considered. Also shown on the graph are the experimental results from scattering and from magnetic diagnostics. The quantitative agreement is quite reasonable considering the difficulties in making the theoretical estimates. We emphasize that this comparison is a result of including the early and late stages of the interaction, and is not scaled. By contrast, the quasi-hydrodynamic formulation of Thode³⁴ gives good agreement with the scaling of plasma heating by an IREB as a function of beam and plasma parameters. Quantitatively, Thode predicts much

greater energy deposition than most experiments observe (including the present one), presumably because he considers only the early stages of the interaction, when it is strongest.

VI. CONCLUSIONS

In this paper, we have presented experimental results for plasma heating by an intense relativistic electron beam. The initial plasma density ranged from $\sim 5 \times 10^{13}/\text{cm}^3$ to $\sim 3 \times 10^{15}/\text{cm}^3$, the lower density cases being partially ionized and the higher density cases highly ionized. In all cases, the energy coupled from the beam to the plasma is greater than can be explained by binary collisions between beam electrons and plasma particles. At the highest plasma densities, classical damping of the beam induced return current is adequate to explain the observed heating. However, over most of the plasma density range tested, i.e. $\leq 1.5 \times 10^{15}/\text{cm}^3$, using a $2 \text{ kA}/\text{cm}^2$ beam, the plasma heating by the beam cannot be explained by classical processes. These results are found to be explained qualitatively and quantitatively by the use of a full nonlinear treatment of the electron-electron two stream instability in the kinetic regime.

The results of this experiment, namely 2 - 7%/m energy coupling efficiency, at beam to plasma density ratios n_b/n_p in the range 10^{-4} - 10^{-2} are consistent with results of previous experiments with comparable beam and plasma parameters.^{12-20,23,59} Similar conclusions as to the energy coupling mechanism, namely the electron-electron instability, have been reached in most of these experiments. However, the use of more detailed diagnostics, and a more uniform interaction geometry in the

present experiment, and a complete nonlinear treatment of the e-e mode instability for comparison with theory, have provided strong confirmation for the presence of this instability.

We should also note that the theory we have used predicts that return current heating due to the parametrically generated ion waves W_a will be dominant for higher beam current densities,³³ a fact confirmed in recently presented preliminary results.^{60, 79}

Presuming that the agreement between theory and experiment is not fortuitous, it is interesting to note a particular implication of our theoretical discussion. Equation (15) for the wave energy transfer rate during the stages of the interaction, when combined with Eq. (17), implies a rate which increases linearly with plasma temperature (at constant densities):

$$\frac{d\epsilon_1}{dt} = 32 \frac{\delta^2}{\omega_p} n_p k T_e .$$

Thus, as the plasma heats, the coupling efficiency via this mechanism increases. This implies that the use of 1 μ s pulse IREB's should be advantageous for heating plasma in a long solenoidal system of the type suggested by Benford, et al.⁹ Clearly, this equation also implies that the coupling efficiency of the entire beam will be increased if the plasma can be preheated to a higher temperature.

ACKNOWLEDGMENT

During the course of this work, a large number of people have provided us with many helpful discussions and assistance. For example, I. Haber provided important assistance in the construction of the atomic physics computational model for the explanation of the partially ionized experiments, as well as in preparation of the results presented in Figs. 23 and 24. R.E. Kribel, C. Ekdahl, K.R. Chu, A.E. Robson, R.N. Sudan, and many others have participated in fruitful discussions of this work with us. The engineering support required by this experiment was provided by J.K. Burton, D. Conte, W.H. Lupton and M.P. Young. Technical assistance was provided by R.M. Jones, J.R. Singer, and J.M. Vary. Initial work on the Thomson scattering system was done by R.H. Dixon and J.L. Ford.

Finally, we would like to acknowledge the support, encouragement and interest of R. Shanny during the entire course of this work.

APPENDIX A

The observation of the scattered power spectrum from a beam of laser light incident on a plasma is a well established technique for obtaining information on the electron velocity distribution function.⁶⁸

If the electrons have a nonrelativistic (electron temperature $T_e \ll 1$ keV) Maxwellian velocity distribution function with a mean velocity of zero, then the electron temperature T_e may be obtained by plotting the logarithm of the measured scattered power I_i vs $\Delta\lambda^2 \equiv (\lambda_o - \lambda_i)^2$, where λ_o is the wavelength of the incident radiation and λ_i is the central wavelength of the i^{th} channel. Assuming that the scattering parameter $\alpha = \lambda_o / 2\pi\lambda_D \ll 1$, where $\lambda_D = v_e / \omega_p$ is the plasma Debye length (v_e is the electron thermal velocity and ω_p the plasma frequency), then we may write

$$I_i = I_o \exp \left[G(\Delta\lambda)^2 \right], \quad (\text{A1})$$

where I_o is the scattered power at $\Delta\lambda = 0$, and

$$G \approx - \frac{c^2}{4 v_e^2 \lambda_o^2 \sin^2(\theta/2)} = - \frac{6.2 \times 10^4}{\lambda_o^2 \sin^2(\theta/2) T_e (\text{eV})}. \quad (\text{A2})$$

The velocity of light is c and θ is the angle between the incident wavevector and the scattered wavevector.

If the Maxwellian distribution has a nonzero mean velocity v_m , then the scattered power spectrum will peak at a wavelength λ_c such that $(\lambda_c - \lambda_o) = (v_m/c)\lambda_o$. Then instead of Eq. (A1), we will have

$$I_i = I_o' \exp \left[G(\lambda_i - \lambda_c)^2 \right], \quad (A3)$$

where now I_o' is the scattered power at $\lambda_i - \lambda_c = 0$, and G is the same so long as $|\lambda_o - \lambda_c| \ll \lambda_o$.

Suppose now we have five scattering channels, labeled 1 thru 5, observing scattered power. Then the ratios of the observed intensities will be

$$\frac{I_1}{I_4} \approx \exp \left\{ G \left[(\lambda_1 - \lambda_c)^2 - (\lambda_4 - \lambda_c)^2 \right] \right\}, \quad (A4)$$

$$\frac{I_2}{I_5} \approx \exp \left\{ G \left[(\lambda_2 - \lambda_c)^2 - (\lambda_5 - \lambda_c)^2 \right] \right\}. \quad (A5)$$

Taking the natural logarithm of both sides of Eqs. (A4) and (A5), solving each for G and equating, we can solve for λ_c :

$$\lambda_c \approx \frac{(\lambda_2^2 - \lambda_5^2) \ln \frac{I_1}{I_4} - (\lambda_1^2 - \lambda_4^2) \ln \frac{I_2}{I_5}}{2(\lambda_2 - \lambda_5) \ln \frac{I_1}{I_4} - 2(\lambda_1 - \lambda_4) \ln \frac{I_2}{I_5}}. \quad (A6)$$

Substituting Eq. (A6) for λ_c back into either Eq. (A4) or (A5) allows a determination of G . More specifically since λ_o and θ are known and fixed (6943 Å and 90°, respectively, in the present experiment) we can solve for T_e :

$$T_e \approx \frac{2.6 \times 10^{-3} (\lambda_1 + \lambda_4 - \lambda_2 - \lambda_5) (\lambda_2 - \lambda_5) (\lambda_1 - \lambda_4)}{(\lambda_1 - \lambda_4) \ln \frac{I_2}{I_5} - (\lambda_2 - \lambda_5) \ln \frac{I_1}{I_4}}. \quad (A')$$

The error associated with the use of λ_0^2 in the denominator of G in place of λ_c^2 , is small relative to the statistical variations of channel data so long as $v_m \ll c$.

Once λ_c and T_e are known, I_0' may be calculated from Eq. (A3). Therefore, the electron density can also be obtained in the usual way⁸⁸ using a Rayleigh density calibration.

In order to minimize errors in Eqs. (A6) and (A7), we clearly want easily measurable intensities, but we also do not want $I_1 \approx I_4$ and $I_2 \approx I_5$ since then the logarithm of the required ratios will be near zero. Placing our (equal width) channels symmetrically about line center, i.e., $\lambda_1 - \lambda_0 \approx -(\lambda_5 - \lambda_0)$, $(\lambda_2 - \lambda_0) \approx -(\lambda_4 - \lambda_0)$, and not using I_2/I_4 and I_1/I_5 allows satisfaction of both of these requirements.

APPENDIX B

In order to understand the observed time dependence of the plasma density and temperature in the partially ionized helium experiments described in Sec. IV.B, we have solved the following set of coupled differential equations:

$$\frac{dn_o}{dt} = - n_p n_o S_1 + n_p n_+ (\alpha_r^+ + \alpha_s^+ n_e) , \quad (B1)$$

$$\frac{dn_+}{dt} = - \frac{dn_o}{dt} - n_p n_+ S_2 + n_p n_{++} (\alpha_r^{++} + \alpha_s^{++} n_p) , \quad (B2)$$

$$n_{++} = N - n_o - n_+ , \quad (B3)$$

$$n_p = n_+ + 2 n_{++} , \quad (B4)$$

$$\begin{aligned} \frac{d}{dt} \left(\sum_2 n_p kT_e \right) = & Q - n_p n_o S_1 E_1 - n_p n_+ S_2 E_2 - n_p n_o \sum_{\text{He-I}} X_i E_i \\ & - n_p n_+ \sum_{\text{He-II}} X_j E_j - P_B - Q_+ - Q_{++} - \frac{3}{2} n_p kT_e (n_+ \alpha_r^+ + n_{++} \alpha_r^{++}) \\ & + n_p^2 \left(\frac{3}{2} kT_e + \bar{E} \right) \left(n_+ \alpha_s^+ + n_{++} \alpha_s^{++} \right) , \end{aligned} \quad (B5)$$

$$\frac{d}{dt} \left(\sum_2 n_+ kT_+ \right) = Q_+ , \quad (B6)$$

$$\frac{d}{dt} \left(\frac{3}{2} n_{++} kT_{++} \right) = Q_{++} \quad . \quad (B7)$$

In these equations we are considering atomic processes only, neglecting all plasma dynamical, kinetic and transport processes (such as expansion, end loss, etc.). This is equivalent to considering the plasma to be spatially uniform on the timescale and spatial scale of interest. These ideas are consistent with the low temperature observed and classical transport and thermal expansion. In solving these equations we assume a Maxwellian velocity distribution for the free electrons and ions.

The first three equations describe the time development of the neutral, singly and doubly ionized helium densities, n_0 , n_+ and n_{++} , respectively, in terms of the electron density n_p and the various rate coefficients. S_1 and S_2 are the ionization rate coefficients for neutral and singly ionized helium, respectively, α_r^+ and α_r^{++} are the radiative recombination coefficients for singly and twice ionized helium, and α_3^+ and α_3^{++} are the three body recombination coefficients. Expressions for S_1 and S_2 are from Drawin,⁷⁰ which agree well with the calculations of Lotz.⁷¹ Adjustments are made to these coefficients to account for ionization from the upper levels of the resonance lines. The radiative recombination coefficients used are those given by Seaton⁸⁰ (α_r^+) and Burgess and Seaton⁸¹ (α_r^{++}), and a hydrogenic expression⁸² has been utilized for the three body recombination coefficient. Equations (B3) and (B4) indicate the conservation of heavy particles (100 mTorr He implies $N \approx 3.5 \times 10^{15}/\text{cm}^3$) and charge neutrality, respectively.

The last three of the above equations, when combined with the other four, give the time dependence of the electron temperature T_e , and the singly and doubly ionized helium temperatures, T_+ and T_{++} , respectively. The terms on the right hand side of Eq. (B5) are, in order: 1.) the heat source term for the electrons, usually taken to be a single resistive term, ηj^2 , where η is the resistivity and j is the plasma current density; power loss due to ionization of 2.) helium atoms and 3.) singly ionized helium, where the ionization energies are $E_1 = 24.6$ eV and $E_2 = 54.4$ eV; power loss due to inelastic electron impact excitation of 4.) helium atoms (He-I), including radiative and metastable states, and 5.) singly ionized helium (He-II), where E_i is the threshold energy for excitation of the i^{th} state with an excitation rate coefficient X_i ; 6.) power loss due to bremsstrahlung; energy transfer rate between the electrons and 7.) singly charged ions and 8.) doubly charged ions (loss rates so long as $T_e > T_+, T_{++}$); 9.) power loss due to radiative recombination of singly and doubly ionized helium; and 10.) power gain due to three body recombination of singly and doubly ionized helium where \bar{E} is an average energy per recombination (taken to be $1/4 E_1$ and $1/4 E_2$ for the two species). The excitation rate coefficient X_i are from Drawin⁷⁰ for energy loss to allowed transitions. The coefficients for the metastable states of helium are obtained⁸³ from measured cross sections.^{84, 85} The bremsstrahlung power coefficient used is the value given by Spitzer⁸⁶ and the electron ion energy transfer rates are obtained from the classical formula given by Braginskii.⁸⁷

The resistivity used in the energy source term $Q = \eta j^2$ in Eq. (B5) consisted of the sum of three terms: 1.) classical resistivity η_{cl} ,

2.) resistivity due to ion acoustic turbulence, η_{ia} , as determined from the experimental results of Zavoiskiy, et al.,⁷⁸ and 3.) resistivity due to electron-electron two stream instability turbulence, η_{ee} , as discussed in Sec. V. Specific values used, in units such that when multiplied by j^2 , with j in kA/cm², the product is in eV/cm³ - sec, were

$$\eta_{cl} = 6 \times 10^{22} \left(\frac{\ln \Lambda}{T_e^{3/2}} + \frac{.005 n_o}{n_p} \right), \quad (B8)$$

$$\eta_{ia} = \frac{3 \times 10^{30}}{\sqrt{n_p}}, \quad (B9)$$

$$\eta_{ee} = 5 \times 10^{32} \frac{n_p}{n_p^{3/2}}. \quad (B10)$$

In these equations, temperatures are in eV and densities in cm⁻³. The first term in η_{cl} is from Spitzer,⁸⁸ $\ln \Lambda$ being the usual coulomb logarithm, and the second term is the resistivity due to electron-neutral collisions, and it is approximated using the elastic collision cross section given by Brown.⁸⁹ The effective collision frequency due to ion acoustic turbulence implied by Eq. (B9) is $\sim \omega_p/80$, where ω_p is the plasma frequency. Since $T_e \gg T_+$, T_{++} whenever plasma current is flowing in the partially ionized He calculations described here, η_{ia} is cut off when the plasma electron drift speed drops below the sound speed $c_s = \sqrt{kT_e/M}$, where M is the mass of the helium ion, as per the discussions in Sec. II.A and V.

By far the most important ionization and energy loss terms in Eqs. (B1), (B2) and (B5) for the partially ionized helium calculations for which results were given in Sec. IV.B were those involving ionization of, and line radiation from, neutral helium. Therefore, we also give the specific coefficients used for these terms, in units of eV-cm³/sec:

$$S_1 = 2.35 \times 10^{-7} \Psi(24.6) \exp \left[-24.6/T_e \right] / \sqrt{T_e}, \quad (B11)$$

$$\sum_{\text{He-I}} X_i E_i = 4.3 \times 10^{-9} \left\{ 0.276 \Psi(21.1) \exp \left[-21.1/T_e \right] + \right. \quad (B12)$$

$$0.2 \Psi(22.9) \exp \left[-22.0/T_e \right] / \sqrt{T_e} \left. + 2.33 \exp \left[-20/T_e \right] \times \right.$$

$$\left. (4.7 \times 10^{-9} + 4.6 \times 10^{-10} T_e - 1.2 \times 10^{-11} T_e^2) \right\},$$

where T_e is in eV and

$$\Psi(X) = \frac{1}{1 + X/T_e} \left(\frac{1}{20 + X/T_e} + \ln \left[1.2 (1 + T_e/X) \right] \right)$$

The first set of terms in Eq. (B12) are the most important optical transitions, and the second set of terms is for metastable transitions.

Equations (B1 - B7) were solved using a computational scheme developed by Boris and Winsor.⁹⁰

Calculated electron density and temperature even at early time (~ 10 ns) were found to be independent of initial electron temperature over the range 1 - 5 eV and ion temperatures from 0.1 - 1 eV. Changes

of the order of 25% in initial density did affect early time temperature (lower initial density giving higher peak temperatures - see Figs. 14 and 15 - and conversely), but only small changes in electron density and temperature for $t \geq 100$ ns were obtained.

REFERENCES

1. J.C. Martin, T.H. Storr, M.J. Goodman and D.W. Forster, private communications, and unpublished reports, AWRE, Aldermaston, England.
2. T.H. Martin, J.P. VanDevender, D.L. Johnson, D.H. McDaniel, and M. Aker in Proc. International Topical Conference on Electron Beam Research and Technology, G. Yonas, Ed. (Sandia Laboratories, Albuquerque, 1976) Vol. 1, pp 450-471, and references therein.
3. J.J. Clark, M. Ury, M.L. Andrews, D.A. Hammer and S. Linke, Record of the 10th Symposium on Electron, Ion and Laser Beam Technology, L. Marton, Ed. (San Francisco Press, San Francisco, 1969), pp 117-130.
4. B. Bernstein and I. Smith, IEEE Trans. Nucl. Sci. NS-18, 294-302 (1971).
5. For a general discussion with many references, see L.S. Levine and M. Ury, IEEE Trans. Nucl. Sci. NS-20, 456-462 (1973).
6. See, for example, Proc. International Topical Conference on Electron Beam Research and Technology, G. Yonas, Ed. (Sandia Laboratories, Albuquerque, 1976), Vol. 1, Ch. 1, and references therein.

7. G. Yonas, J.W. Poukey, K.R. Prestwich, J.R. Freeman, A.J. Toepfer and M.J. Clauser, Nucl. Fusion 14, 731-740 (1974).
8. C. Stallings, R. Schneider and D. Cummings in Proc. International Topical Conference on Electron Beam Research and Technology, G. Yonas, Ed. (Sandia Laboratories, Albuquerque, 1976), Vol. 1, pp 364-375.
9. J. Benford, T.S.T. Young, B. Ecker, D. Dakin, I. Smith, S. Putnam and V. Bailey, in Proc. International Topical Conference on Electron Beam Research and Technology, G. Yonas, Ed. (Sandia Laboratories, Albuquerque, 1976), Vol. 2, pp 476-508.
10. Beam injection into toroidal geometry has been investigated by J. Benford, B. Ecker and V. Bailey, Phys. Rev. Lett. 33, 574-577 (1974); P. Gilad, B.R. Kusse and T.R. Lockner, Phys. Rev. Lett. 33, 1275-1278 (1974) and Phys. Fluids 18, 607-613 (1975); and M. Masuzaki, A. Mohri, T. Tsuzuki and K. Ikuta, in Proc. International Topical Conference on Electron Beam Research and Technology, G. Yonas, Ed. (Sandia Laboratories, Albuquerque, 1976), Vol. 2, pp 435-454.
11. D.A. Hammer and K. Papadopoulos, Nucl. Fusion 15, 977-984 (1975).
12. A.T. Altyntsev, A.G. Eskov, O.A. Zolotovskii, V.I. Koroteev, R. Kh. Kurtmullaev, V.D. Masalov, and V.N. Semenov, ZhETF Pis. Red. 13, 197-201 (1971) [JETP Lett. 13, 139-141 (1971)]; A.T. Altyntsev, B.N. Breizman, A.G. Eskov, O.A. Zolotovskii, V.I. Koroteev, R. Kh. Kurtmullaev, V.D. Masalov, D.D. Ryutov and V.N. Semenov, in Plasma Physics and Controlled Nuclear Fusion Research 1971 (IAEA, Vienna, 1971), Vol. II, pp 309-324.

13. D.R. Smith, Phys. Lett. 42A, 211-212 (1972).
14. C.A. Kapetanacos and D.A. Hammer, Appl. Phys. Lett. 23, 17-19 (1973).
15. P.A. Miller and G.W. Kuswa, Phys. Rev. Lett. 30, 958-961 (1973).
16. Yu. I. Abrashitov, V.S. Koydan, V.V. Konyukhov, V.M. Lagunov, V.N. Luk'yanov, and K.I. Mekler, ZhETF Pis. Red. 18, 675-679 (1973)
[JETP Lett. 18, 395-397 (1973)]; Yu. I. Abrashitov, V.S. Koydan, V.V. Konyukhov, V.M. Lagunov, V.N. Luk'yanov, K.I. Mekler and D.D. Ryutov, Zh. Eksp. Teor. Fiz. 66, 1324-1337 (1974) [Sov. Phys. - JETP 39, 647-653 (1975)].
17. A.V. Arzhannikov, B.N. Breizman, L.N. Vyacheslavov, V.S. Koydan, V.V. Konyukhov and D.D. Ryutov, in Plasma Physics and Controlled Nuclear Fusion Research 1974 (IAEA, Vienna, 1975), Vol. III, pp 257-268.
18. P. Korn, F. Sandel and C.B. Wharton, Phys. Rev. Lett. 31, 579-583 (1973); J. Appl. Phys. 44, 4946-4949 (1973).
19. C. Ekdahl, M. Greenspan, R.E. Kribel, J. Sethian and C.B. Wharton, Phys. Rev. Lett. 33, 346-348 (1974).
20. P.A. Miller, Appl. Phys. Lett. 27, 107-109 (1975).
21. J.P. VanDevender, J.D. Kilkenny and A.E. Dangor, Phys. Rev. Lett. 33, 689-692 (1974); J. Appl. Phys. 47, 1955-1963 (1976).
22. D. Prono, B. Ecker, N. Bergstrom and J. Benford, Phys. Rev. Lett. 35, 438-441 (1975).
23. C.A. Kapetanacos, W.M. Black and K.R. Chu, Phys. Rev. Lett. 34, 1156-1159 (1975).

24. G.C. Goldenbaum, W.F. Dove, K.A. Gerber and B.G. Logan, Phys. Rev. Lett. 32, 830-833 (1974); B.G. Logan, W.F. Dove, K.A. Gerber and G.C. Goldenbaum, IEEE Trans. Plasma Sci. 2, 182-186 (1974).
25. W.F. Dove, K.A. Gerber and D.A. Hammer, Appl. Phys. Lett. 28, 173-176 (1976).
26. R. Okamura, Y. Nakamura and N. Kawashima, Appl. Phys. Lett. 28, 701-703 (1976).
27. R.E. Lee and R.N. Sudan, Phys. Fluids 14, 1213-1225 (1971).
28. B.N. Breizman and D.D. Ryutov, Nucl. Fusion 14, 873-907 (1974).
29. Ya. B. Fainberg, V.D. Shapiro and V.I. Shevchenko, Zh. Eksp. Teor. Fiz. 57, 966-977 (1969) [Sov. Phys. - JETP 30, 528-533 (1970)].
30. L.E. Thode and R.N. Sudan, Phys. Rev. Lett. 30, 732-734 (1973); Phys. Fluids 18, 1552-1563 (1975).
31. L.I. Rudakov, Zh. Eksp. Teor. Fiz. 59, 2091-2104 (1970) [Sov. Phys. - JETP 32, 1134-1140 (1971)].
32. R.L. Ferch and R.N. Sudan, Plasma Phys. 17, 905-915 (1975).
33. K. Papadopoulos, Phys. Fluids 18, 1769-1777 (1975).
34. L.E. Thode, Phys. Fluids 19, 305-315 and 831-848 (1976).
35. A.J. Toepfer and J.W. Poukey, Phys. Lett. 42A, 383-384 (1973); Phys. Fluids 16, 1546-1547 (1973).
36. L.E. Thode and B.B. Godfrey, Phys. Fluids 19, 316-320 (1976); B.B. Godfrey, W.R. Shanahan and L.E. Thode, Phys. Fluids 18, 346-355 (1975).
37. D.A. Hammer and N. Rostoker, Phys. Fluids 13, 1831-1850 (1970).
38. J.L. Cox and W.H. Bennett, Phys. Fluids 13, 182-192 (1970).

39. K.R. Chu and N. Rostoker, Phys. Fluids 16, 1472-1479 (1973).
40. G. Küppers, A. Salat and H.K. Wimmel, Plasma Phys. 15, 429-439 (1973).
41. J.D. Lawson, J. Electron. Control 3, 587-594 (1957); 5, 146-151 (1958); J. Nucl. Energy, Pt. C, 1, 31-35 (1959).
42. G. Yonas and P. Spence in Record of the 10th Symposium on Electron, Ion and Laser Beam Technology, L. Marton, Ed. (San Francisco Press, San Francisco, 1969), pp 143-154; PIFR-106, Physics International Co. (1968), unpublished.
43. K.R. Chu, C.A. Kapetanakis and R.W. Clark, Appl. Phys. Lett. 27, 185-187 (1975).
44. K.R. Chu, R.W. Clark, M. Lampe, P.C. Liewer and W.M. Manheimer, Phys. Rev. Lett. 35, 94-98 (1975).
45. H. Alfven, Phys. Rev. 55, 425-429 (1939).
46. R.V.E. Lovelace and R.N. Sudan 27, 1256-1258 (1971).
47. L.E. Thode and R.N. Sudan, Phys. Fluids 18, 1564-1573 (1975).
48. C.A. Kapetanakis, W.M. Black and C.D. Striffler, Appl. Phys. Lett. 26, 368-370 (1975).
49. W.H. Bennett, Phys. Rev. 45, 890-897 (1934); 98, 1584-1593 (1955).
50. D.J. Rose and M. Clark, Jr., Plasmas and Controlled Fusion, (John Wiley, New York, 1961), Ch. 14.
51. K.R. Chu and R.W. Clark, to be published.
52. T.G. Roberts and W.H. Bennett, Plasma Phys. 10, 381-389 (1968).
53. J. Benford and B. Ecker, Phys. Fluids 15, 366-368 (1972).
54. L.S. Levine, I.M. Vitkovitsky, D.A. Hammer and M.L. Andrews, J. Appl. Phys. 42, 1863-1869 (1971).

55. M.L. Andrews, H.E. Davitian, D.A. Hammer, H.H. Fleischmann, J.A. Nation, and N. Rostoker, *Appl. Phys. Lett.* 16, 98-100 (1970).
56. The phenomena observed in the early experiments in which beams were injected into neutral gas are reviewed by S.E. Graybill, *IEEE Trans. Nucl. Sci.* NS-18, 438-446 (1971). A preionized plasma was used in Refs. 52-54.
57. C.A. Kapetanakos and C.D. Striffler, *J. Appl. Phys.* 46, 2509-2515 (1975).
58. M. Friedman and M. Ury, *Rev. Sci. Instr.* 41, 1334-1335 (1970).
59. C. Ekdahl, M. Greenspan, J. Sethian and C.B. Wharton, *Bull. Am. Phys. Soc.* 20, 1270-1271 (1975); J.D. Sethian, C. Ekdahl, and C.B. Wharton, *Bull. Am. Phys. Soc.* 21, 674 (1976).
60. M. Greenspan, C. Ekdahl, J. Sethian and C.B. Wharton, *Bull. Am. Phys. Soc.* 20, 1271 (1976).
61. K.R. Chu and N. Rostoker, *Phys. Fluids* 17, 813-827 (1974).
62. R.K. Parker, R.E. Anderson and C.V. Duncan, *J. Appl. Phys.* 45, 2463-2479 (1974).
63. J.K. Burton, J.J. Condon, M.D. Jevnager, W.H. Lupton, and T.J. O'Connell, *Proc. Fifth Symp. on Engineering Problems of Fusion Research* (IEEE, New York, 1974), pp 613-618.
64. D. Pellinen, *Rev. Sci. Instr.* 41, 1347-1348 (1970).
65. H.R. Griem, *Plasma Spectroscopy* (McGraw-Hill, New York, 1964), pp 309-312.
66. J. Sheffield, *Plasma Scattering of Electromagnetic Radiation*, (Academic Press, New York, 1975).
67. K.A. Gerber, Naval Research Laboratory Memorandum Report 2818 (1974).

68. L.E. Aranchuk, E.K. Zavoiskii, D.N. Lin, and L.I. Rudakov, ZhETF Pis. Red. 15, 33-34 (1972) [JETP Lett. 15, 22-24 (1972)].
69. M.N. Rosenbluth and C.S. Liu, Phys. Fluids 19, 815-818 (1976).
70. H.W. Drawin, Collisions and Transport Cross Sections, Euratron Special Report EUR-CEA-FC-383, March, 1966, Revised 1967.
71. W. Lotz, Astrophys. J. Suppl. 14, 207-238 (1967).
72. K. Papadopoulos, M.L. Goldstein and R.A. Smith, Astrophys. J. 190, 175-185 (1974).
73. V.N. Tsytovich, Physics 82C, 141-154 (1976).
74. W. Manheimer and K. Papadopoulos, Phys. Fluids 18, 1397-1398 (1975).
75. J. Dawson and C. Oberman, Phys. Fluids 5, 517-524 (1962); Phys. Fluids 6, 394-397 (1963).
76. K. Papadopoulos and T. Coffey, J. Geophys. Res. 79, 1558-1561 (1974).
77. P.J. Palmadesso, T.P. Coffey, I. Haber and K. Papadopoulos, Bull. Am. Phys. Soc. 20, 1277 (1975); H. Rowland and K. Papadopoulos, Bull. Am. Phys. Soc. 21, 1170 (1976).
78. E.K. Zavoisky, B.A. Demidov, Yu. G. Kalinin, A.G. Plakhov, L.I. Rudskov, V.E. Rusanov, V.A. Skoryupin, G. Ye. Smolkin, A.V. Titov, S.D. Franchenko, V.V. Shapkin, and G.V. Sholin, Plasma Physics and Controlled Fusion Research, (IAEA, Vienna, 1971) Vol. II, pp 3-24.
79. A.K.L. Dymore-Bradshaw, A.E. Dangor and J.D. Kilkenny, Plasma Physics and Controlled Fusion Research 1976, (IAEA, Vienna, 1977) to be published (paper CN-35/G2-4).
80. M.J. Seaton, Royal Astron. Soc. M.N. 119, 81-89 (1959).
81. A. Burgess and M.J. Seaton, Royal Astron. Soc. M.N. 121, 76 (1960).

82. Y.B. Zeldovitch and Y.P. Raizer, Physics of Shock Waves and High Temperature Hydrodynamic Phenomena (Academic Press, New York, 1966) Vol. 1, p. 407.
83. A.W. Ali and A.D. Anderson, Naval Research Laboratory, Private Communication.
84. C.R. Lloyd, E. Weigold, P.J.O. Teubner, and S.T. Hood, J. Phys. B5, 1712-1718 (1972).
85. W.L. Borst, Phys. Rev. A9, 1195-1200 (1974).
86. L. Spitzer, Jr., Physics of Fully Ionized Gases (Interscience, New York, 1967), p. 149
87. S.I. Braginskii, in Reviews of Plasma Physics, M.A. Leontovich, Ed. (Consultant Bureau, New York, 1965), Vol. 1, p. 217.
88. Spitzer, Op. cit., p. 139.
89. S.C. Brown, Basic Data of Plasma Physics, 1966 (MIT Press, Cambridge, 1967), p. 17.
90. Jay Boris and Niels Winsor, Princeton Plasma Physics Laboratory Report MATT-652 (1970).

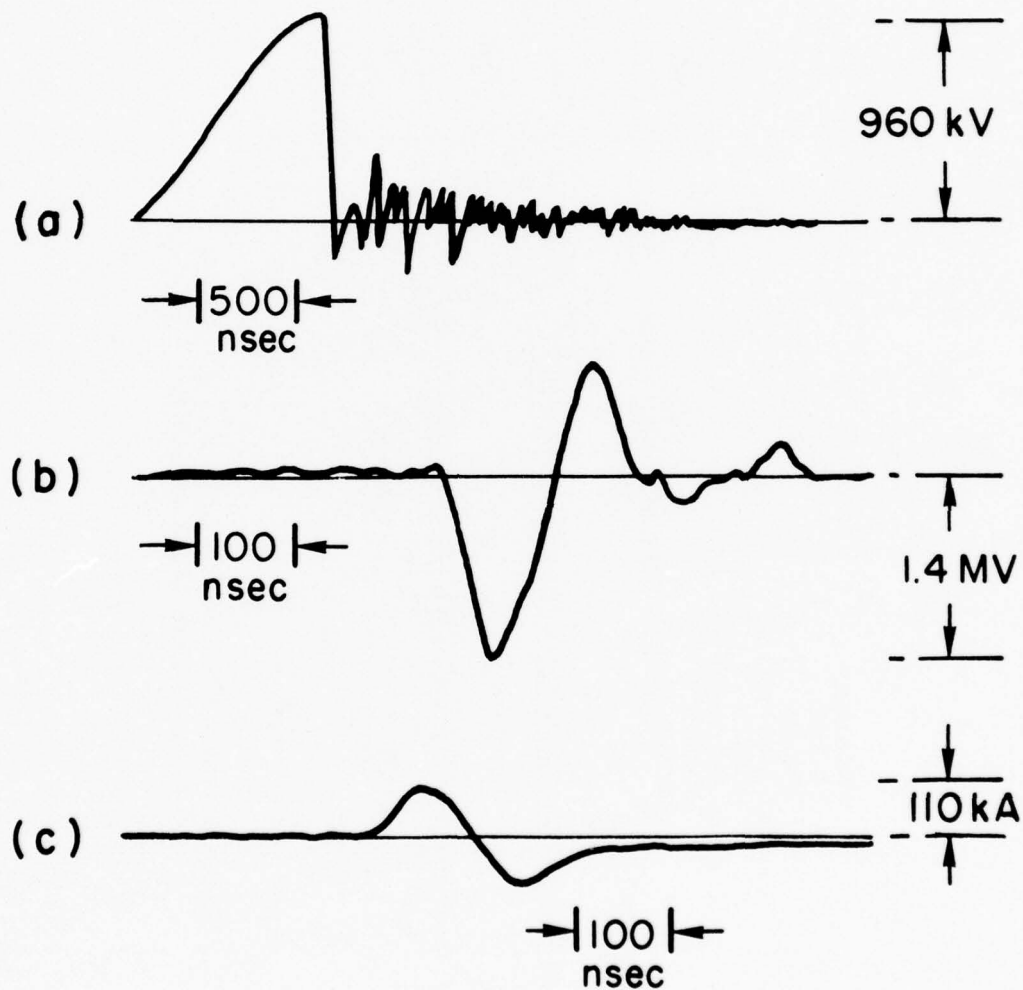


Fig. 1 — A sample set of oscillographs of (a) the Marx generator charging the Blumlein pulse forming line, (b) the electron beam diode voltage, and (c) the electron beam current in the diode

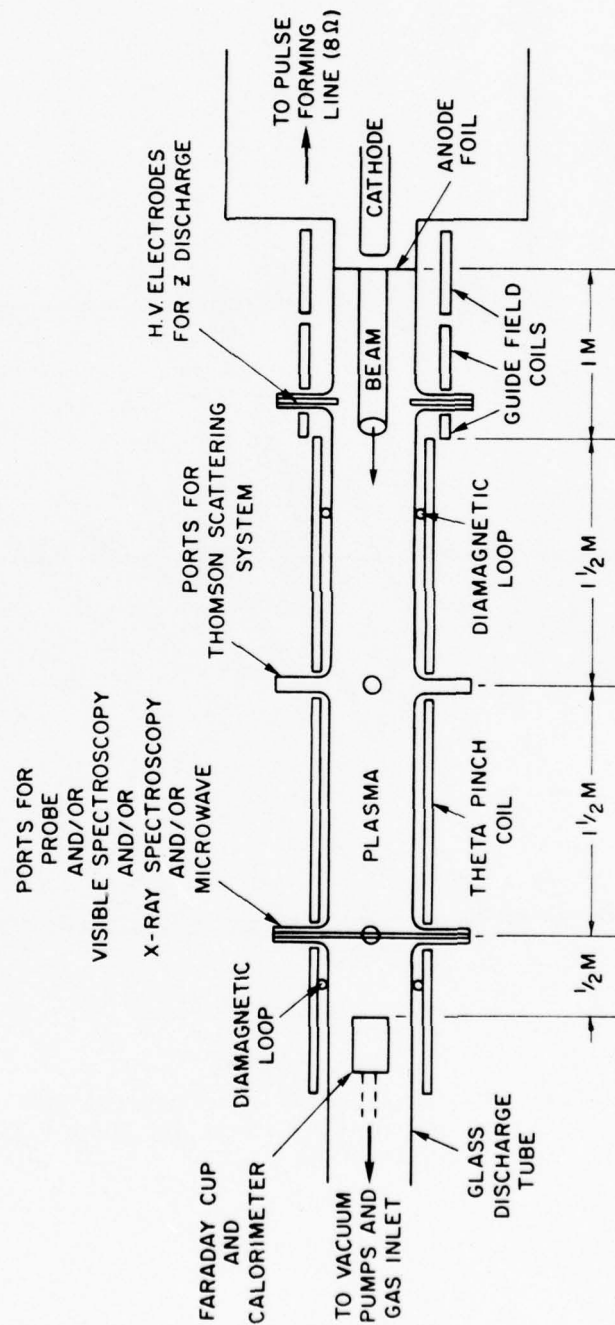


Fig. 2 — Schematic of the experiment showing the location of key components and diagnostics

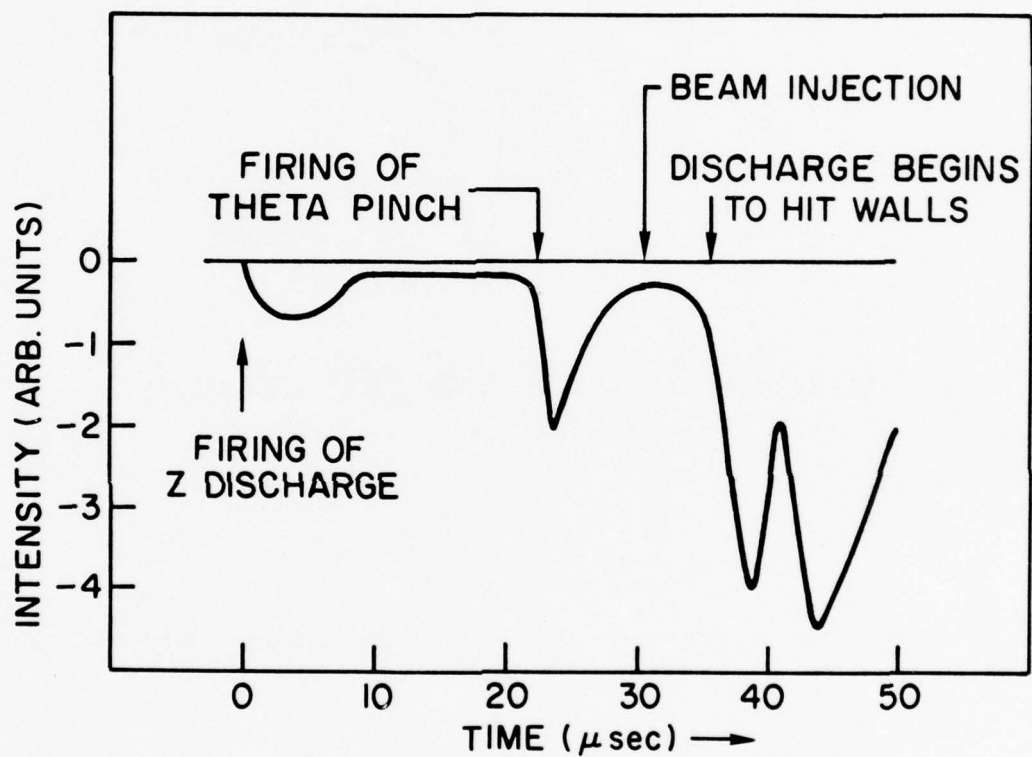
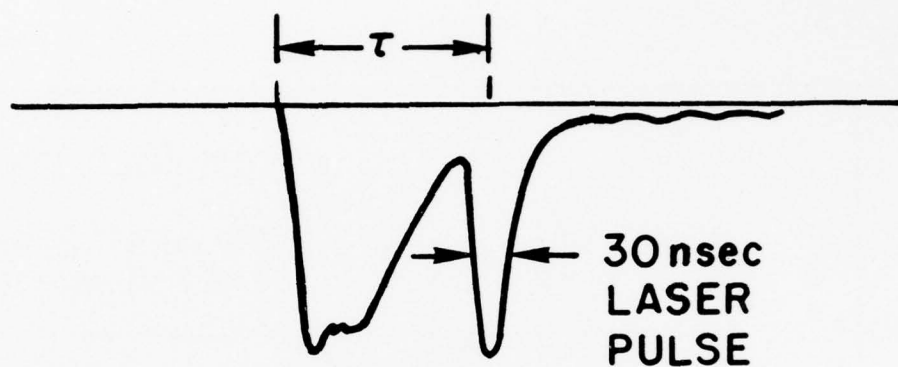
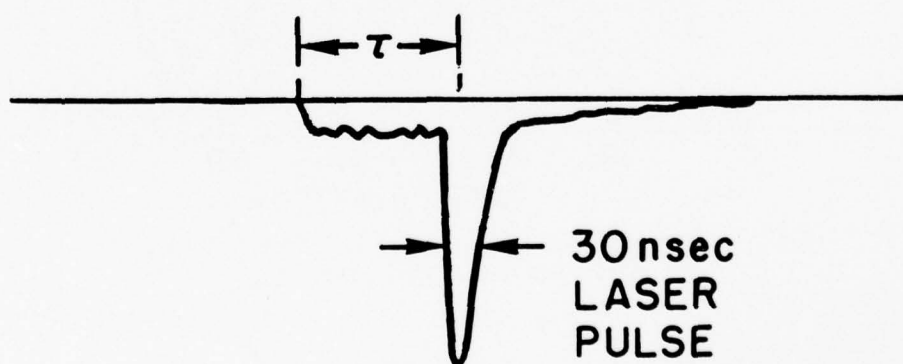


Fig. 3 - A sample oscillograph of H_β (4861 Å) light from the plasma for the highly ionized case



(a) PARTIALLY IONIZED CASE



(b) HIGHLY IONIZED CASE

Fig. 4 — Sample oscillographs from a typical channel of the Thomson scattering system for the (a) partially ionized and (b) highly ionized cases. The laser timing τ is from the *start* of the beam induced enhanced continuum to the peak of the laser pulse. The large enhanced continuum during the beam pulse in the partially ionized case required $\tau \gtrsim 70$ ns.

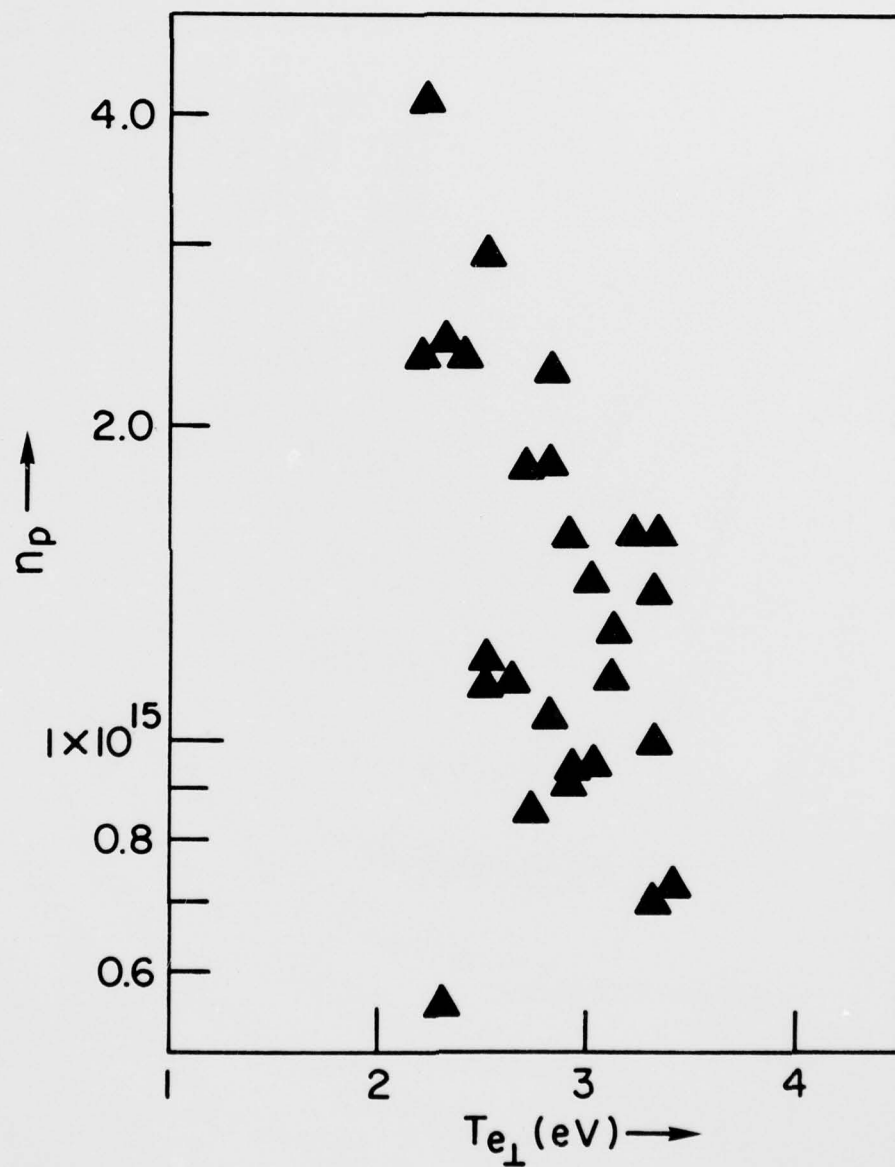


Fig. 5 — The range of densities and temperatures (from Thomson scattering) obtained in one sequence of plasma discharges in the highly ionized case with no beam injection

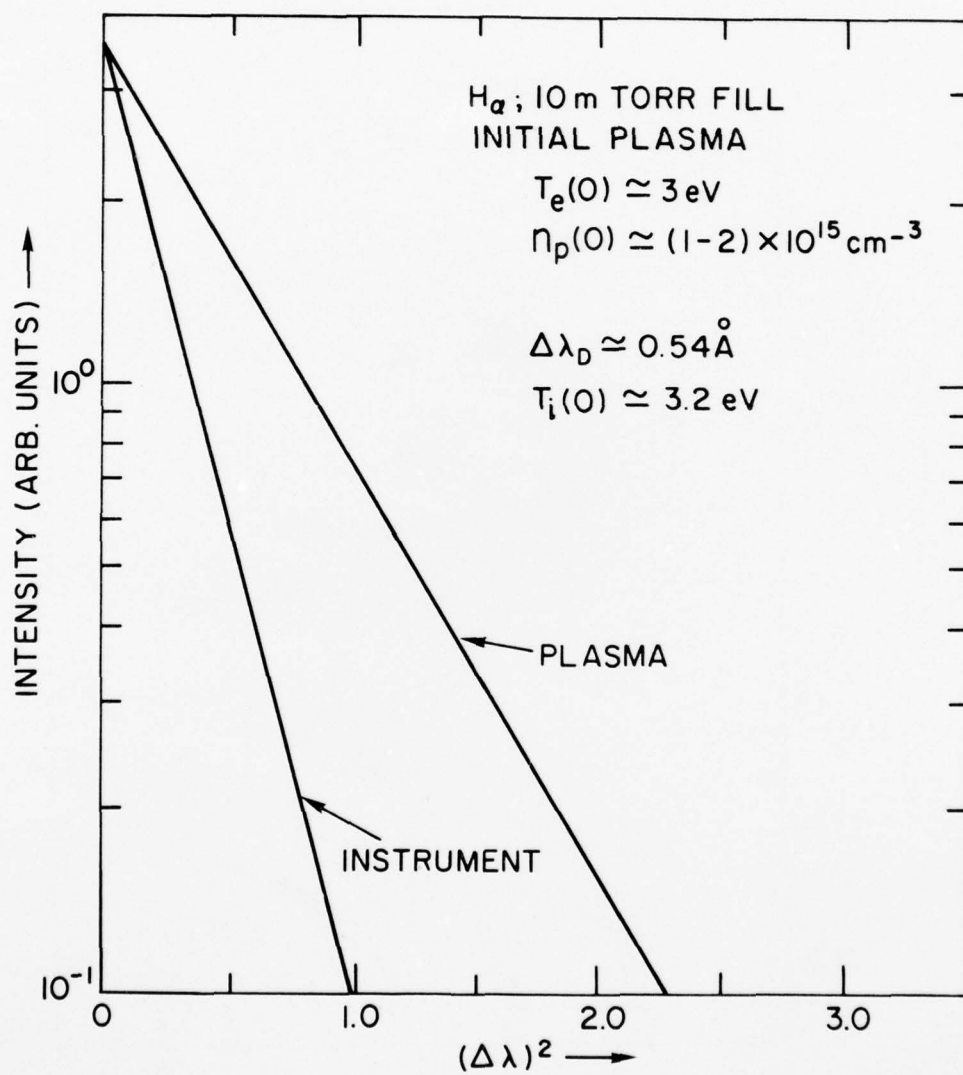


Fig. 6 — Determination of the ion temperature from the Doppler broadening of the H_{α} line (6531 Å)

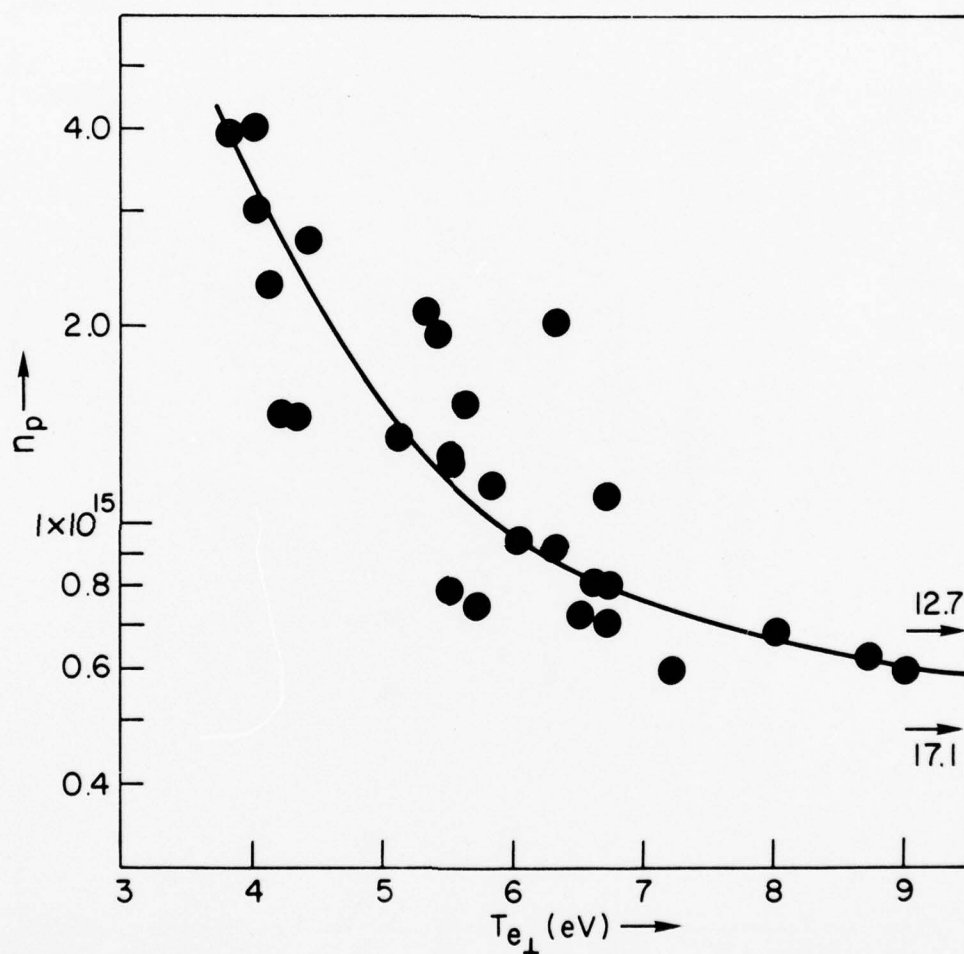


Fig. 7 — Plasma density versus temperature (from Thomson scattering) for a series of beam shots corresponding to the plasma only shots shown in Fig. 5. Arrows indicate two data points with unusually high temperatures. The line is simply to emphasize the trend.

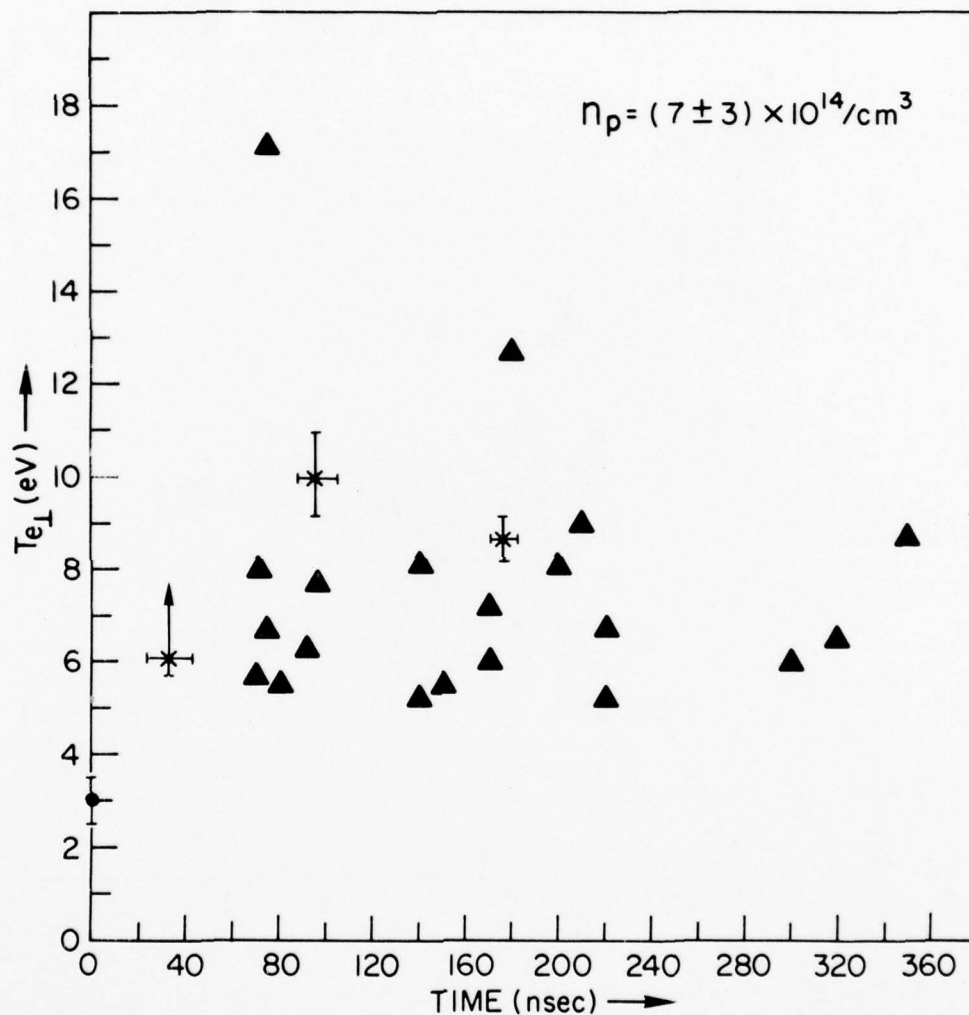


Fig. 8(a) — Plasma temperature as a function of time (from Thomson scattering) for shots having plasma density in the ranges (a) $(7 \pm 3) \times 10^{14} / \text{cm}^3$, (b) $(1.5 \pm 0.5) \times 10^{15} / \text{cm}^3$, and (c) $(3.1 \pm 1.0) \times 10^{15} / \text{cm}^3$. Parts (a) and (b) include data points (shown with error bars) obtained during a previously published run.²⁵ Arrows on error bars indicate the presence of tails containing an unknown total energy, but estimated to raise the average electron energy to near the top of the arrow. The curves in (c) are obtained assuming classical resistive heating and the plasma current densities shown.

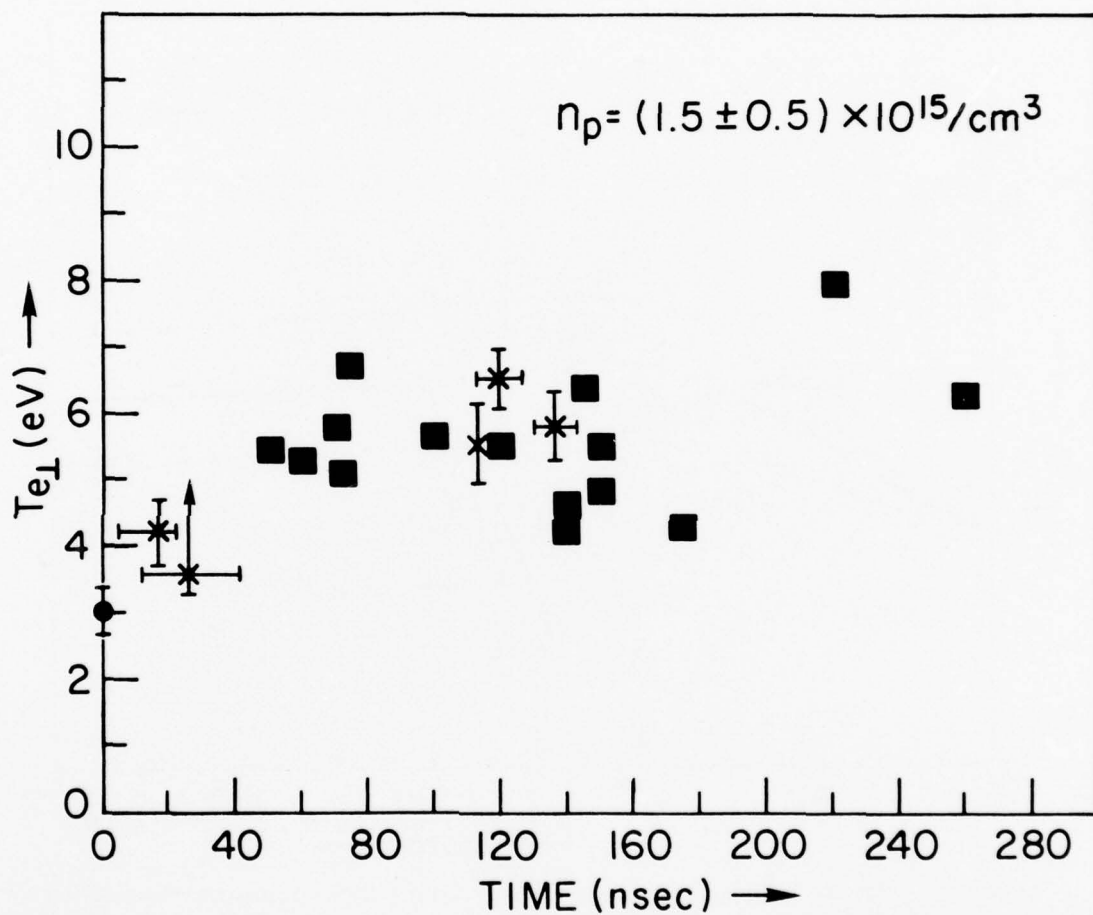


Fig. 8(b) (Continued)

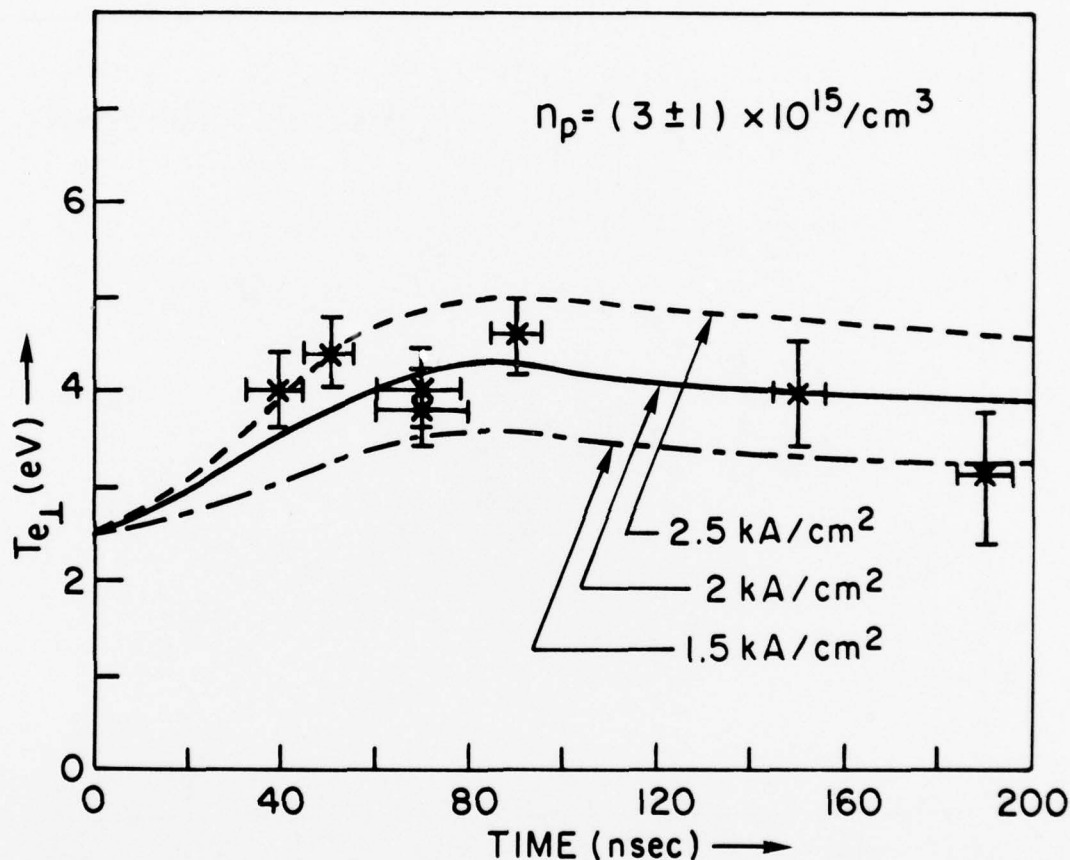


Fig. 8(c) — Plasma temperature as a function of time (from Thomson scattering) for shots having plasma density in the ranges (a) $(7 \pm 3) \times 10^{14}/\text{cm}^3$, (b) $(1.5 \pm 0.5) \times 10^{15}/\text{cm}^3$, and (c) $(3.1 \pm 1.0) \times 10^{15}/\text{cm}^3$. Parts (a) and (b) include data points (shown with error bars) obtained during a previously published run.²⁵ Arrows on error bars indicate the presence of tails containing an unknown total energy, but estimated to raise the average electron energy to near the top of the arrow. The curves in (c) are obtained assuming classical resistive heating and the plasma current densities shown.

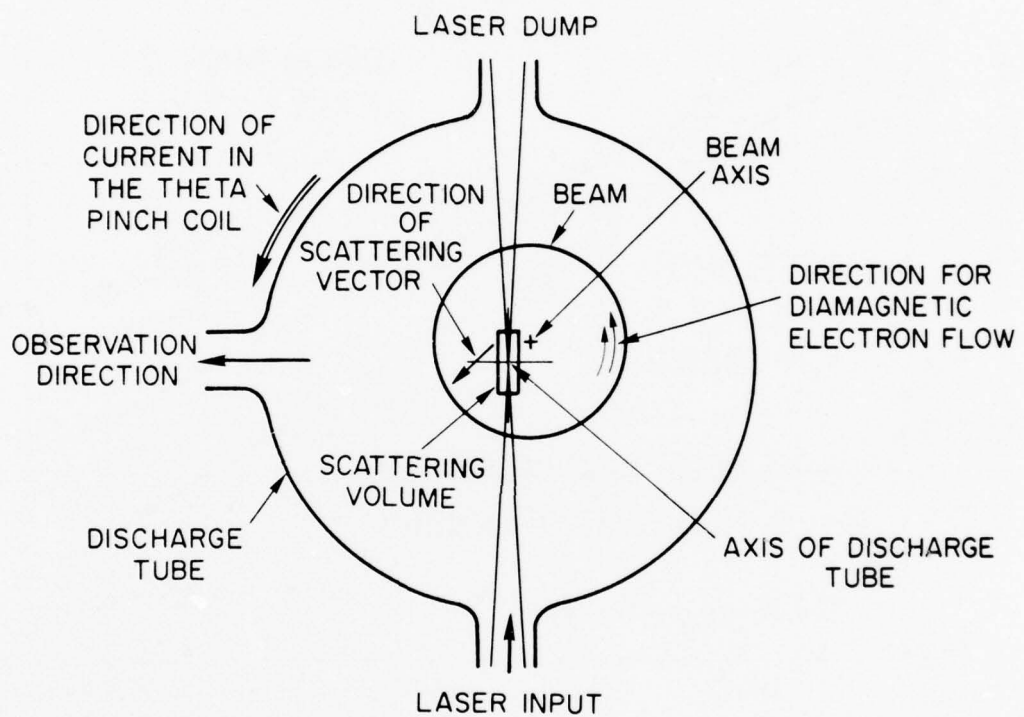


Fig. 9(a) — Simplified interaction geometry at the laser scattering part

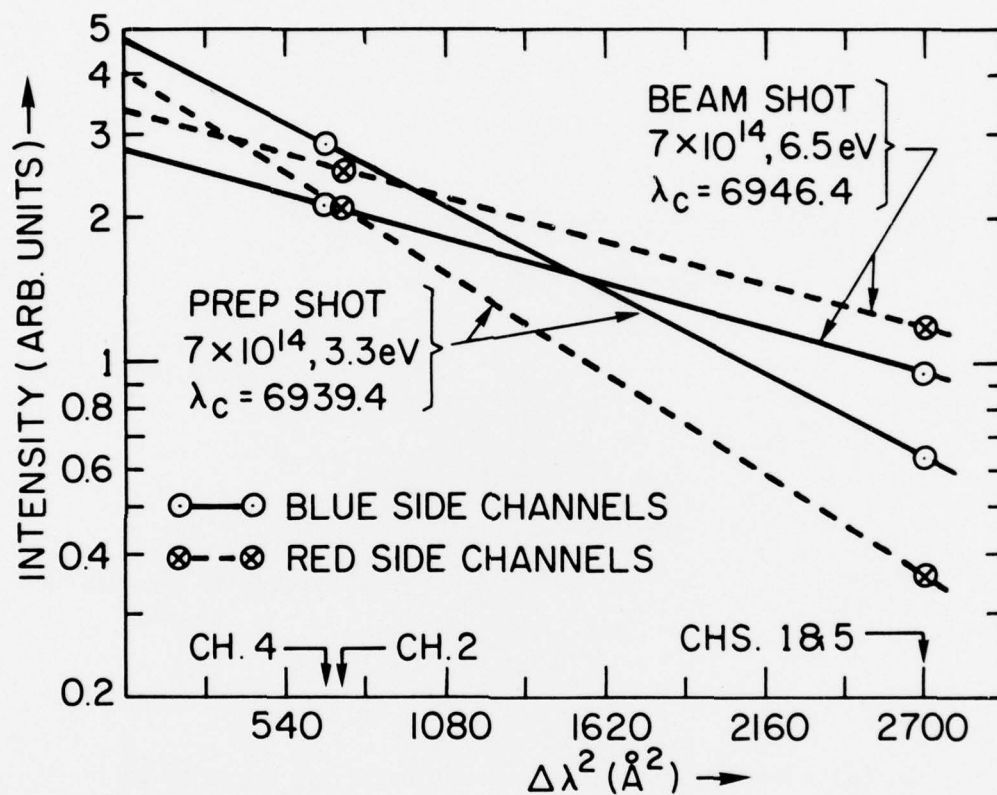


Fig. 9(b) — Intensity versus the square of the wavelength shift data for selected prep shot and beam shot cases to illustrate the observed shift from blue side enhancement to red side enhancement

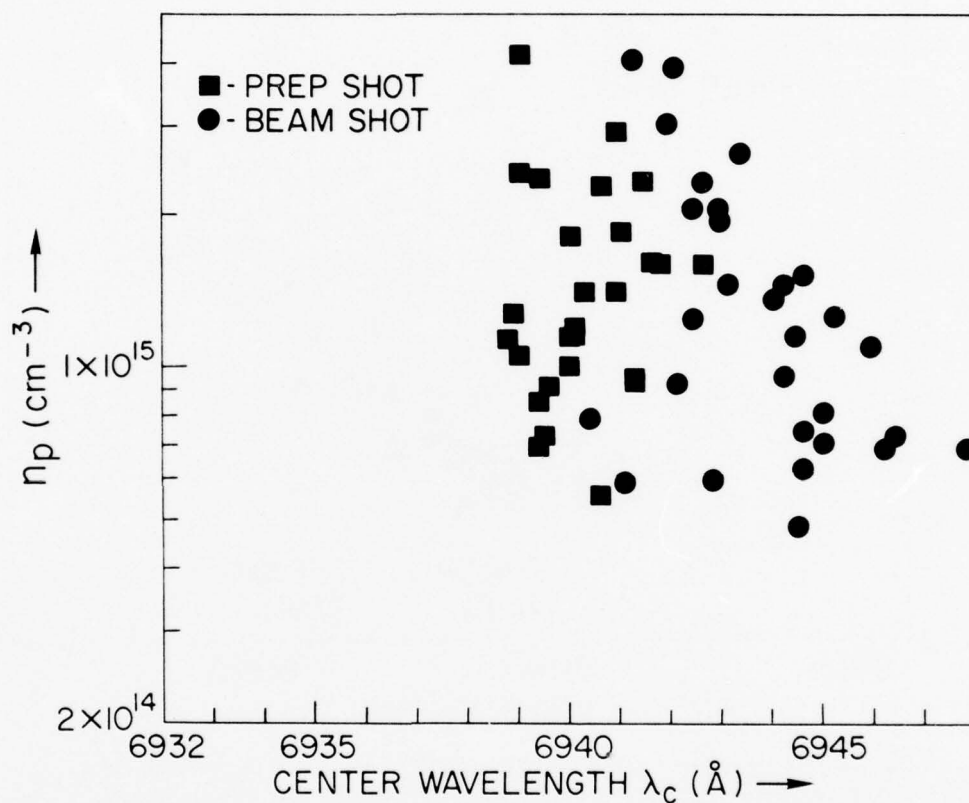


Fig. 10 — Calculated scattering line center (Appendix A) versus (a) density, and (b) temperature, for beam and plasma shots. Arrows indicate the line center of the 17.1 eV and 12.7 eV cases. The tendency for beam shots to have a larger center wavelength is evident in both figures.

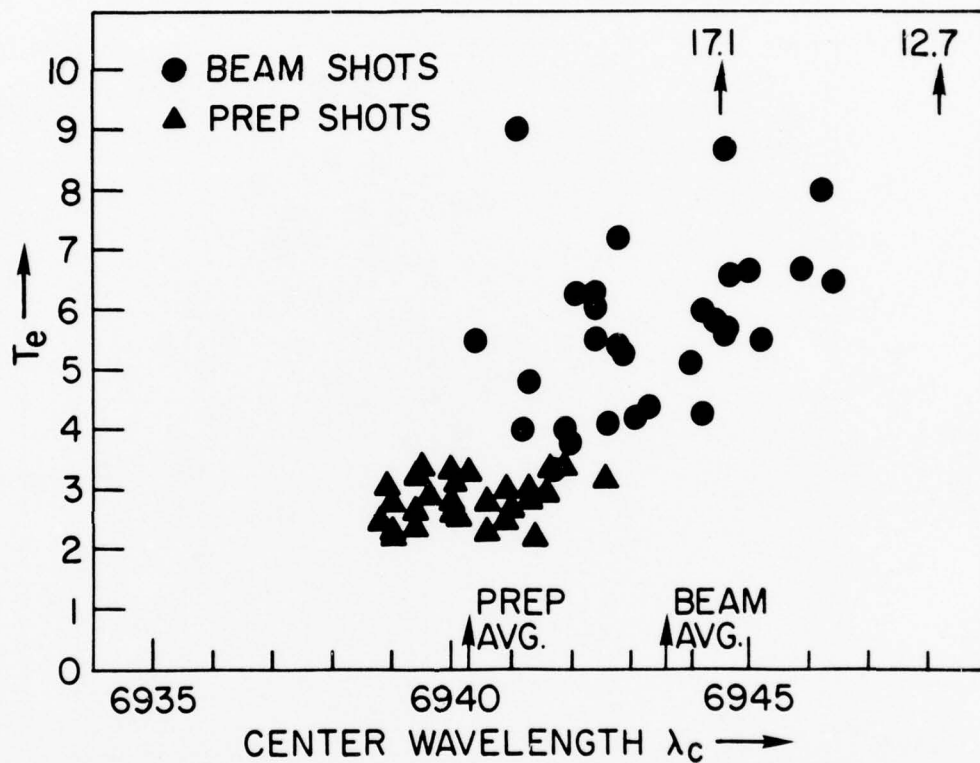


Fig. 10 (Continued) — Calculated scattering line center (Appendix A) versus (a) density, and (b) temperature, for beam and plasma shots. Arrows indicate the line center of the 17.1 eV and 12.7 eV cases. The tendency for beam shots to have a larger center wavelength is evident in both figures.

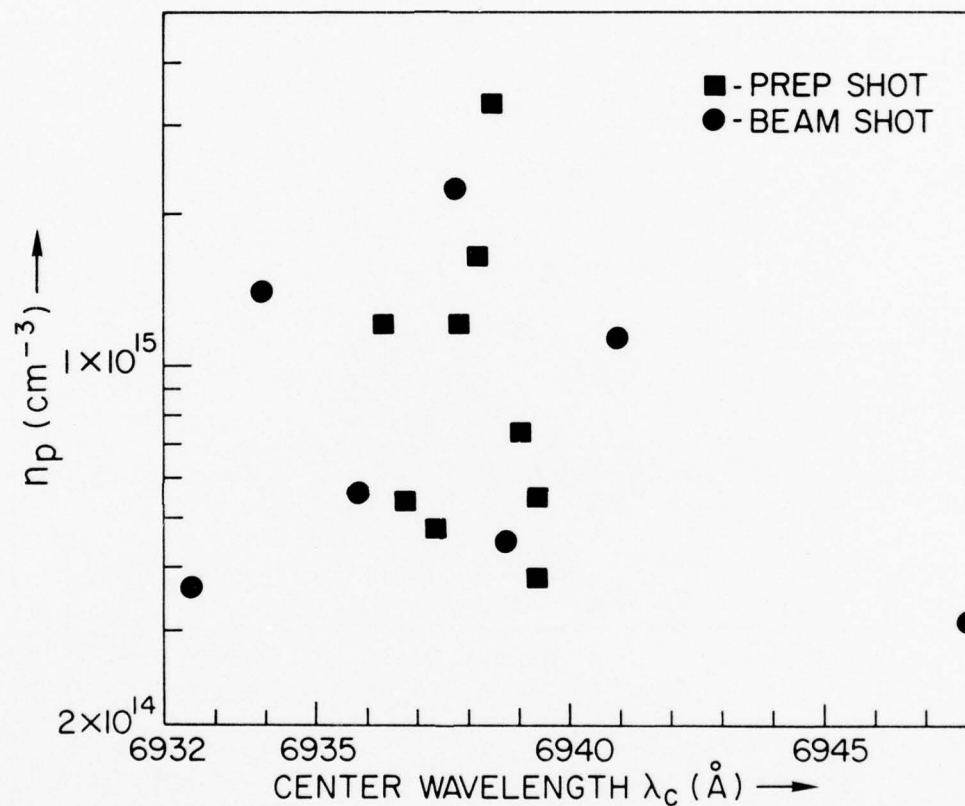


Fig. 11(a)—Scattering line center versus (a) density, and (b) temperature, when only the upper half of the scattering volume was viewed. Density and temperature for the lower half of the scattering volume are shown in (c) and (d) respectively. The upper half beam results show random line center shifts relative to prep shot results, whereas in the lower half case the beam shot line centers are shifted to longer wavelength relative to prep shot centers.

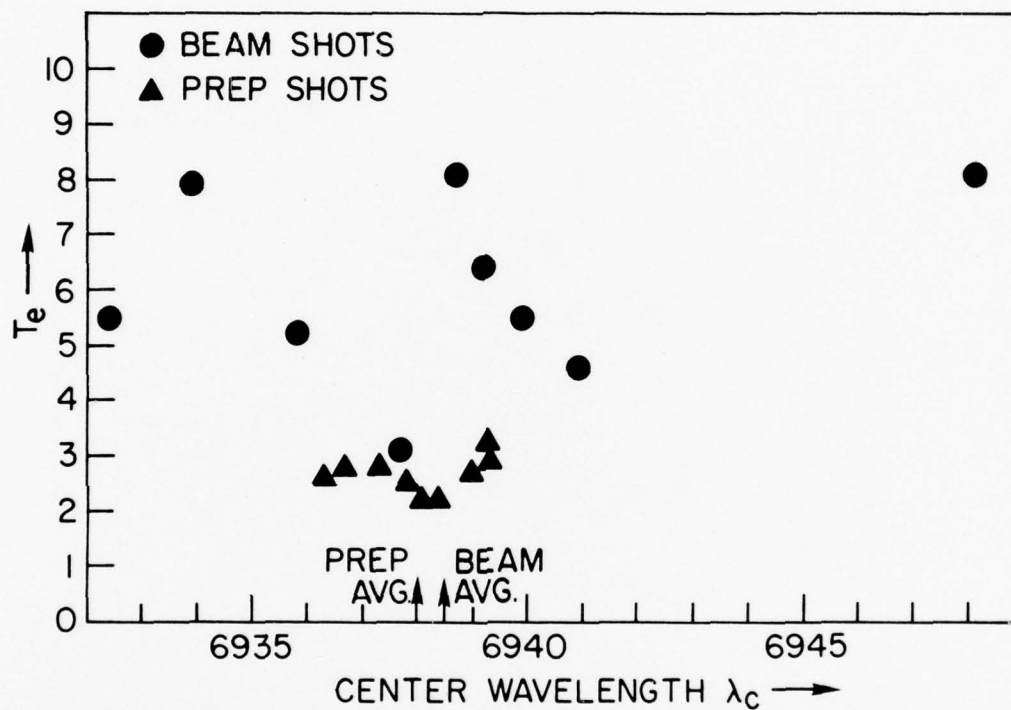


Fig. 11(b) (Continued) — Scattering line center versus (a) density, and (b) temperature, when only the upper half of the scattering volume was viewed. Density and temperature for the lower half of the scattering volume are shown in (c) and (d) respectively. The upper half beam results show random line center shifts relative to prep shot results, whereas in the lower half case the beam shot line centers are shifted to longer wavelength relative to prep shot centers.

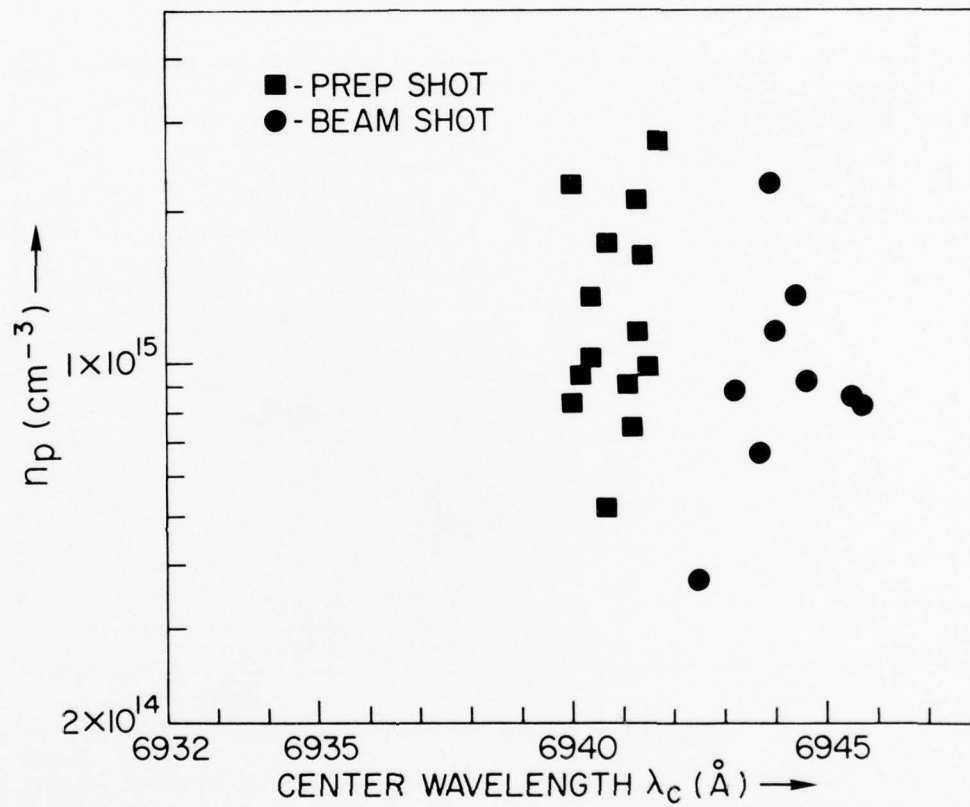


Fig. 11(c) (Continued)

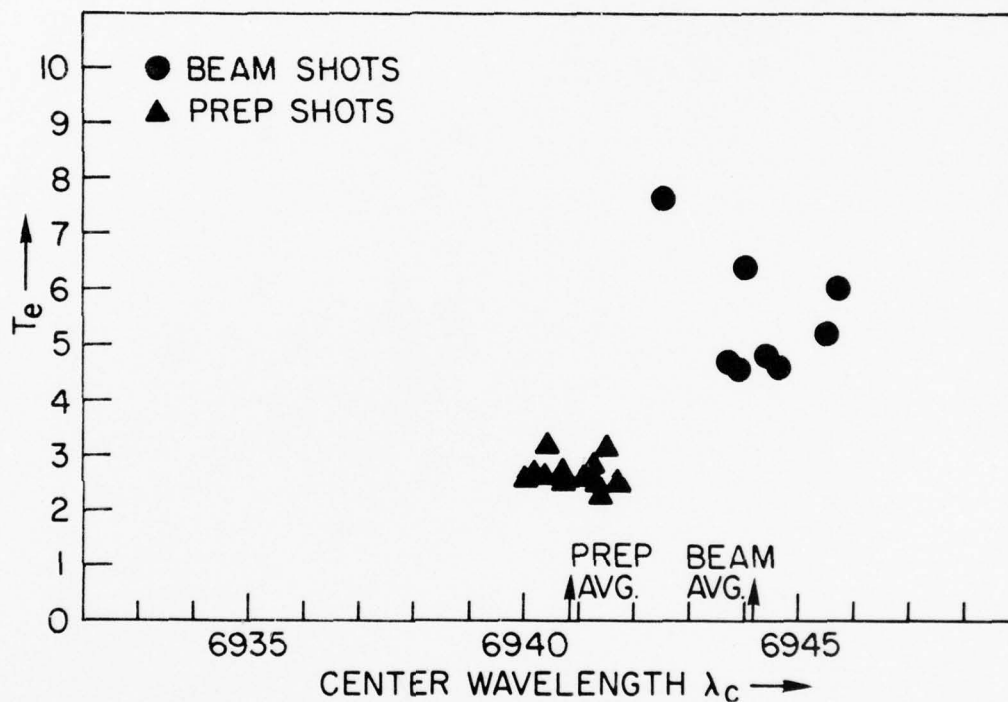


Fig. 11(d) (Continued) — Scattering line center versus (a) density, and (b) temperature, when only the upper half of the scattering volume was viewed. Density and temperature for the lower half of the scattering volume are shown in (c) and (d) respectively. The upper half beam results show random line center shifts relative to prep shot results, whereas in the lower half case the beam shot line centers are shifted to longer wavelength relative to prep shot centers.

AD-A036 308

NAVAL RESEARCH LAB WASHINGTON D C

F/G 20/9

INTENSE RELATIVISTIC ELECTRON BEAM INTERACTION WITH A COOL THET--ETC(U)

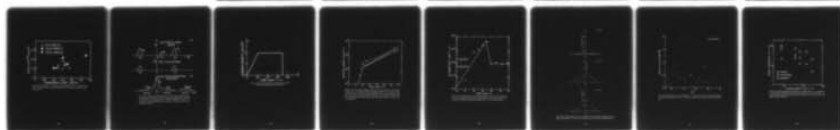
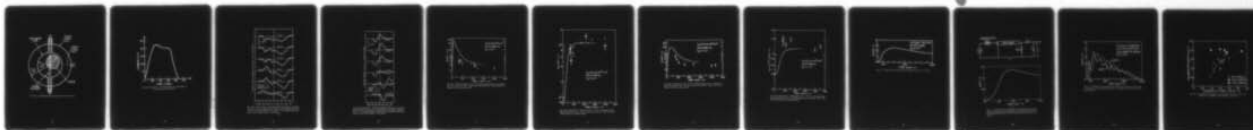
JAN 77 D A HAMMER, K A GERBER, W F DOVE

UNCLASSIFIED

NRL-MR-3439

NL

2 OF 2
AD
A036308

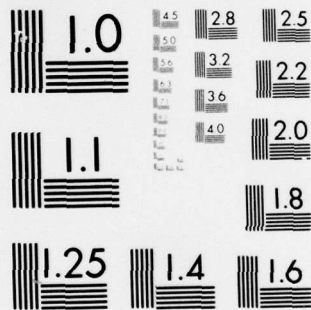


END

DATE

FILMED

3-77



MICROCOPY RESOLUTION TEST CHART
NATIONAL BUREAU OF STANDARDS-1963-A

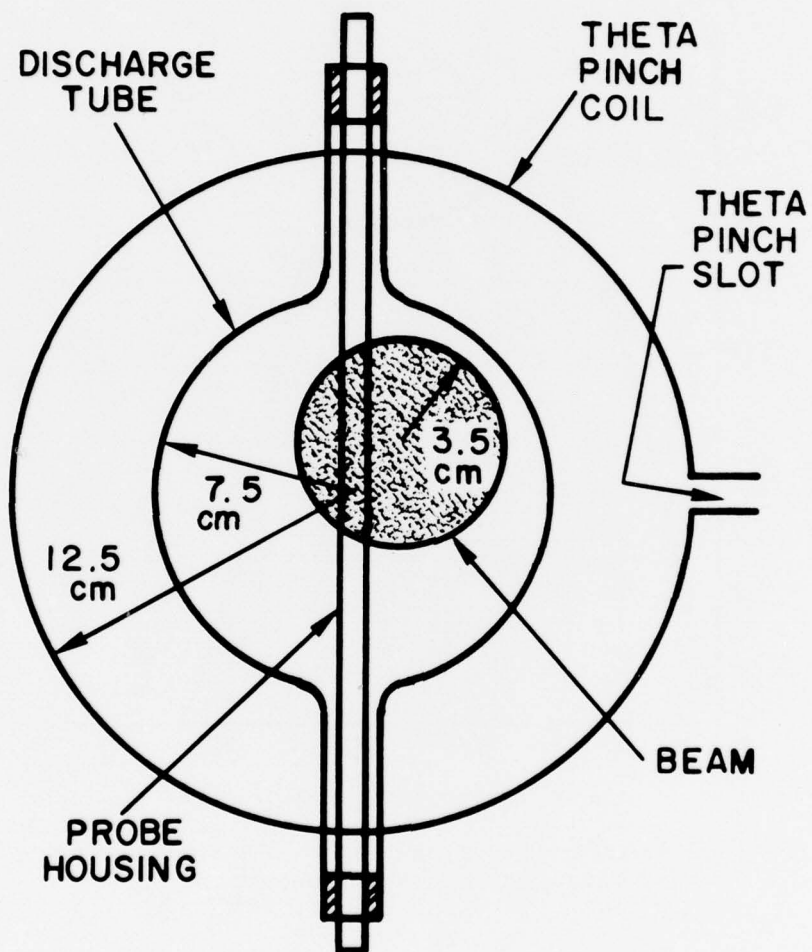


Fig. 12(a) — Simplified interaction geometry at the probe port

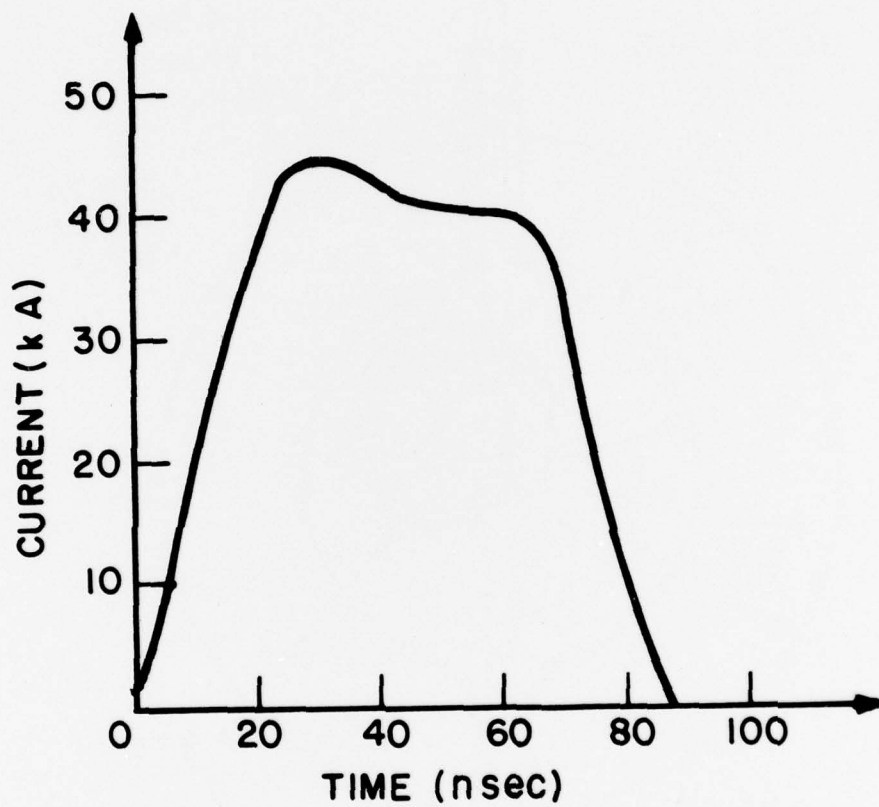


Fig. 12(b) (Continued) — Typical Faraday cup oscillogram for the magnetic probe experiment

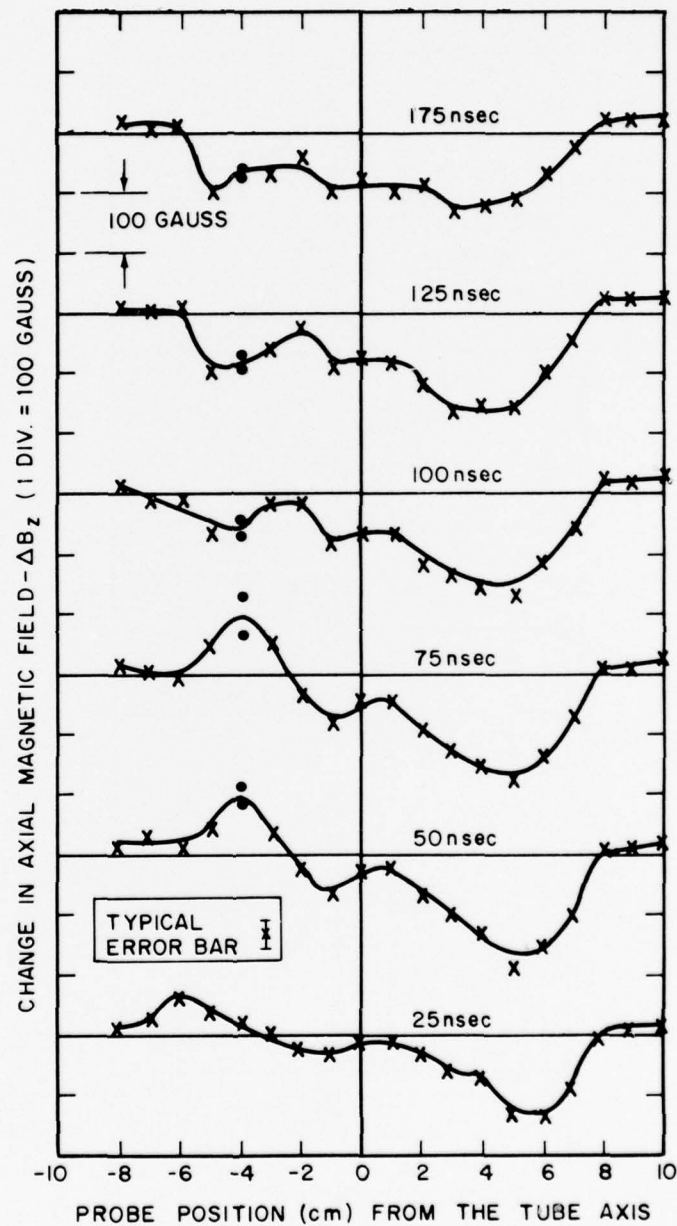


Fig. 13(a) — The change in the axial magnetic field, ΔB_z as a function of probe position at various times during the beam-plasma interaction. Shot to shot reproducibility is illustrated by individual data points shown at one radial position in each figure.

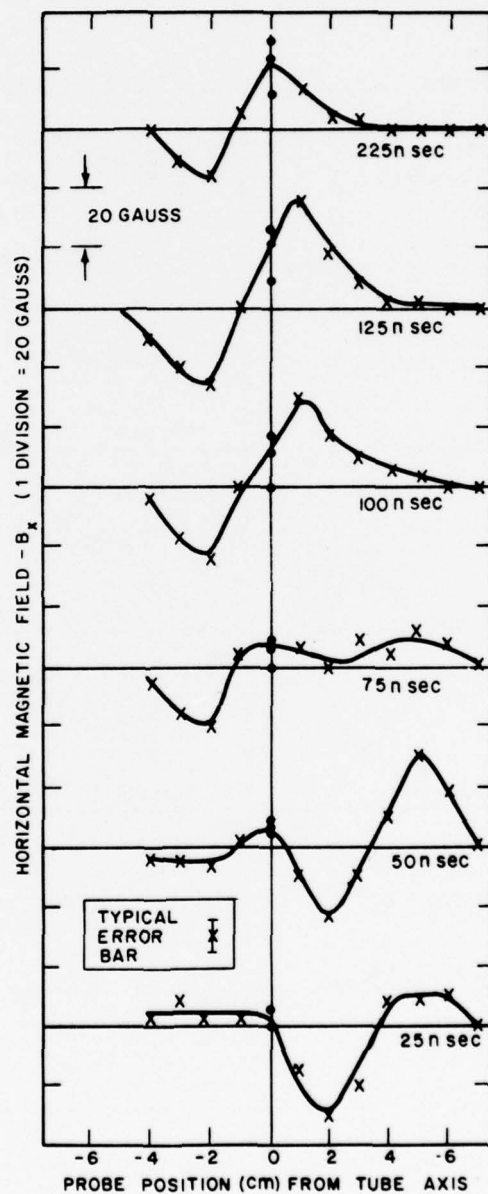


Fig. 13(b) (Continued) — Horizontal magnetic field, B_x , as a function of probe position at various times during the beam-plasma interaction. Shot to shot reproducibility is illustrated by individual data points shown at one radial position in each figure.

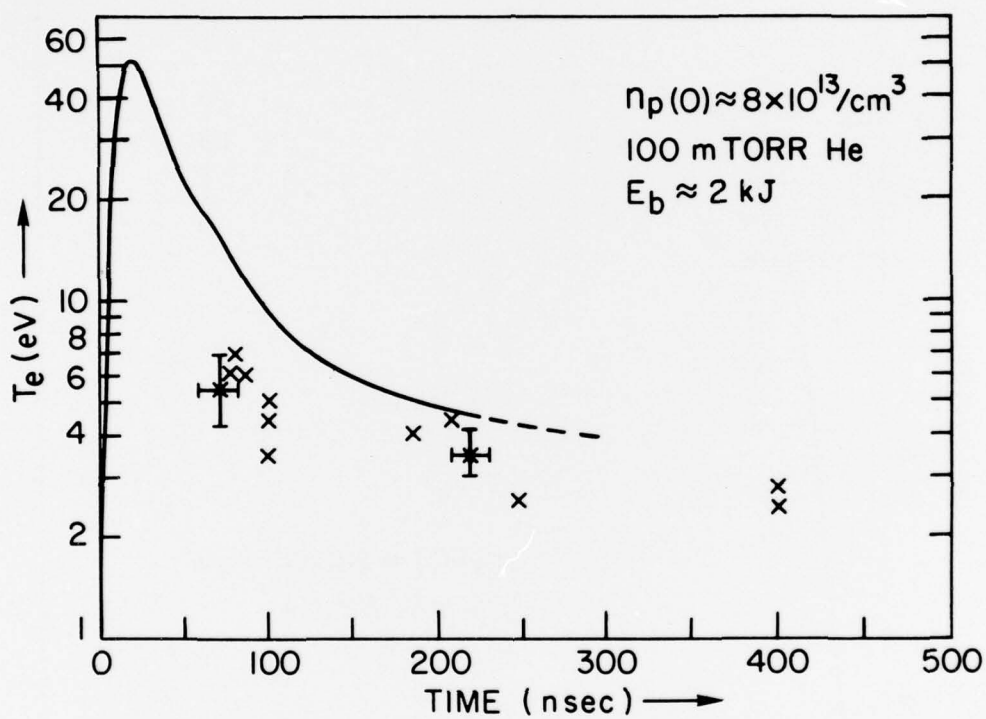


Fig. 14(a) — Results for the 8×10^{13} case showing plasma electron temperature, data as a function of time. Typical error bars are shown. Solid curves are obtained from the numerical model.

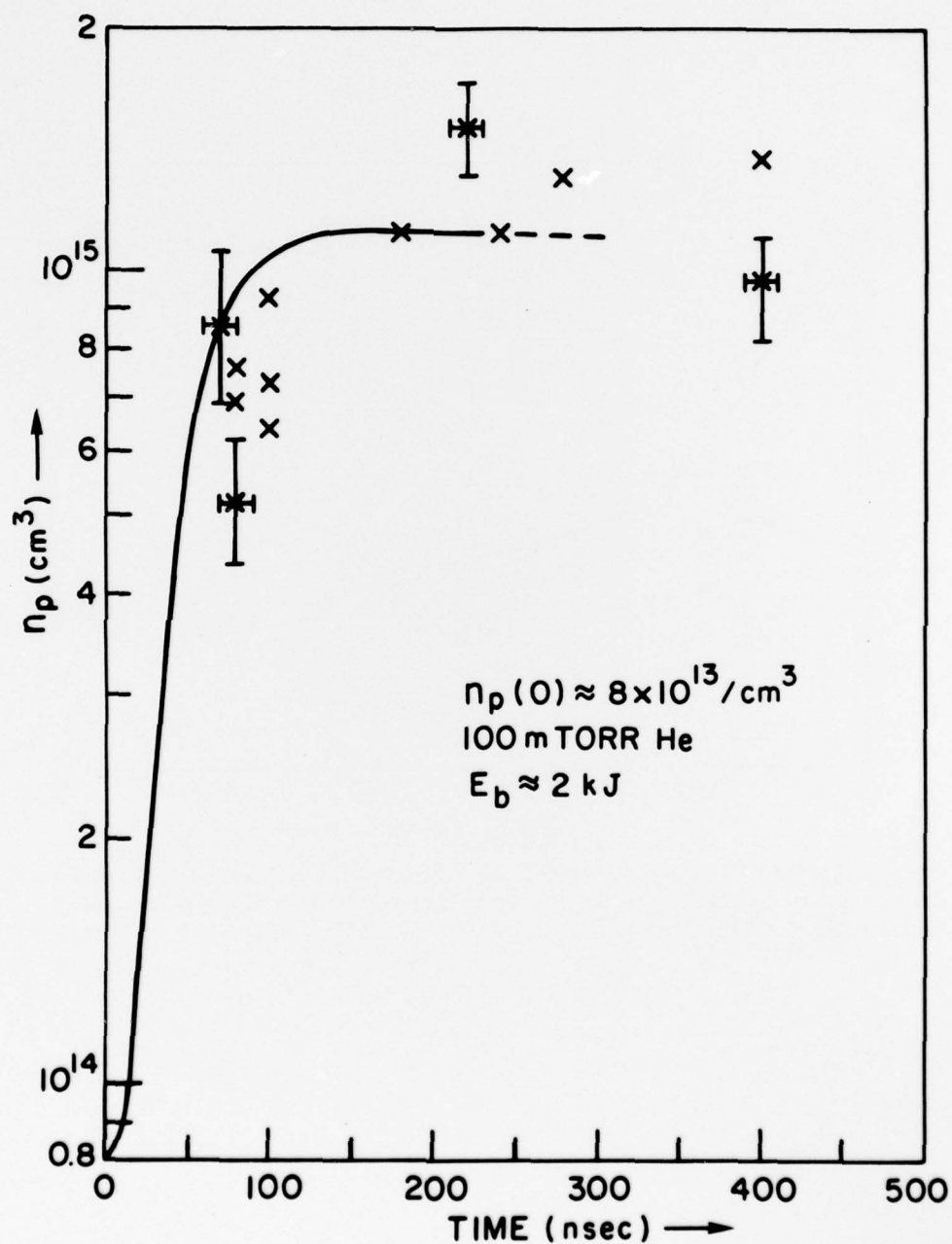


Fig. 14(b) (Continued) — Results for the 8×10^{13} case showing density, data as a function of time. Typical error bars are shown. Solid curves are obtained from the numerical model.

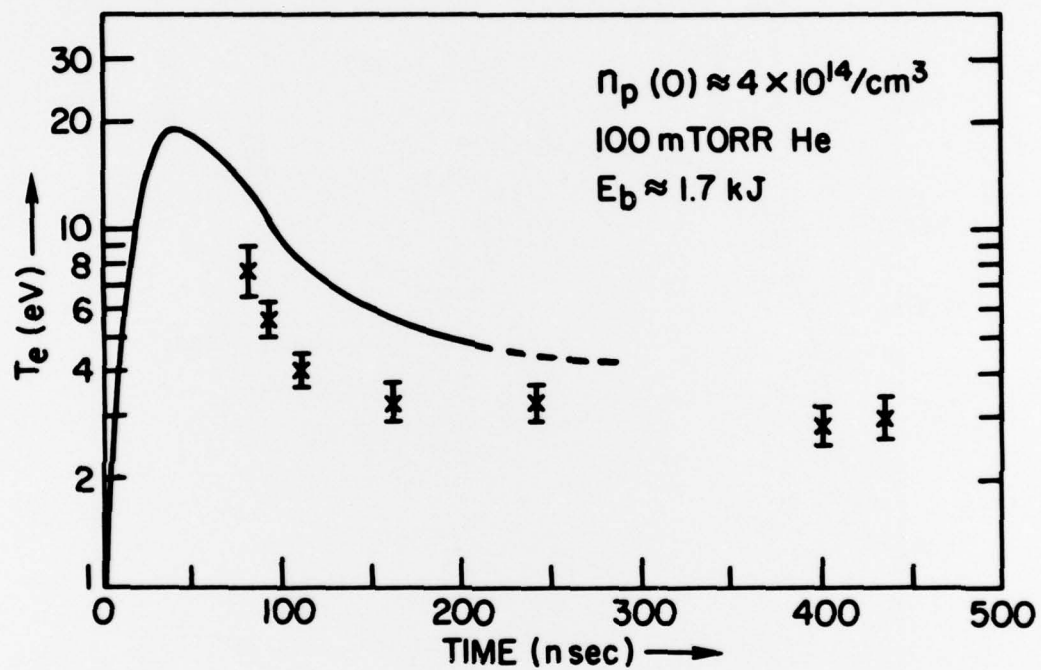


Fig. 15(a) — Results for the 4×10^{14} case showing plasma electron temperature, data as a function of time. Typical error bars are as shown. Solid curves are obtained from the numerical model.

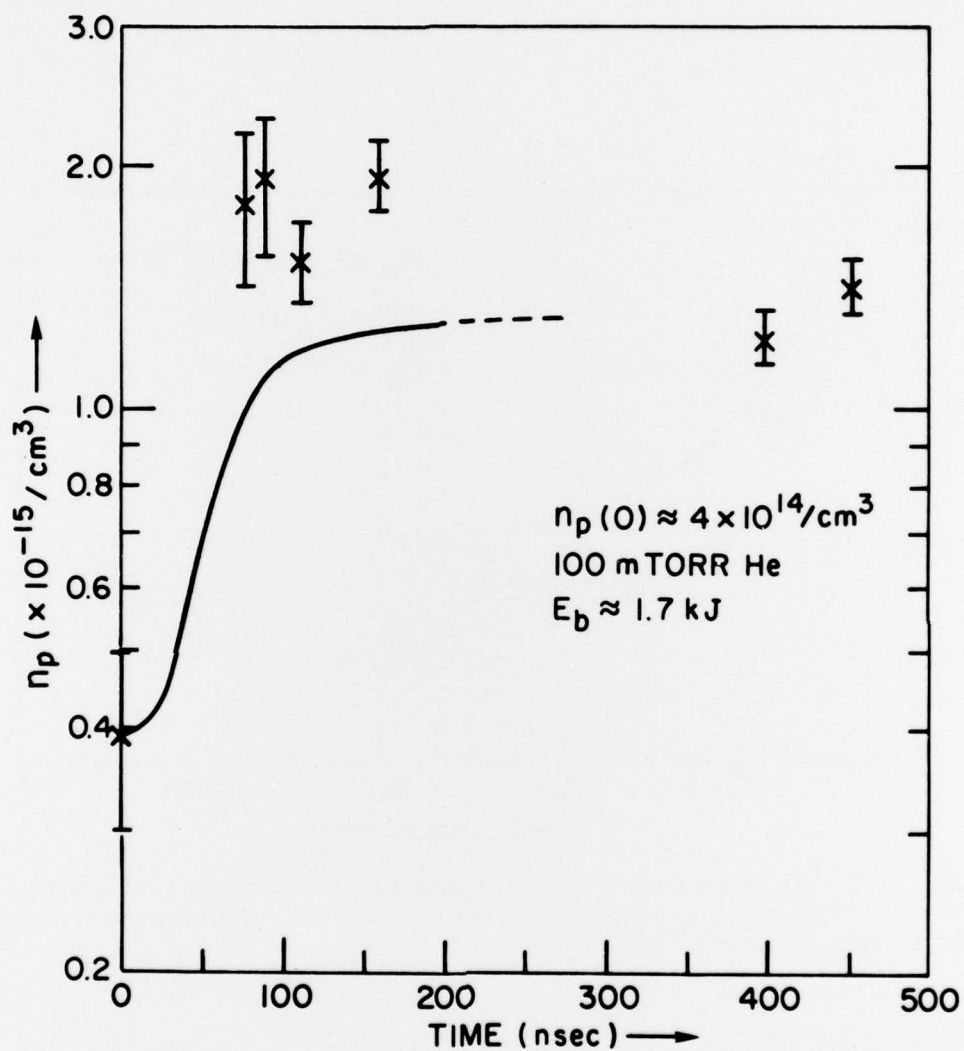


Fig. 15(b) (Continued) — Results for the 4×10^{14} case showing density, data as a function of time. Typical error bars are as shown. Solid curves are obtained from the numerical model.

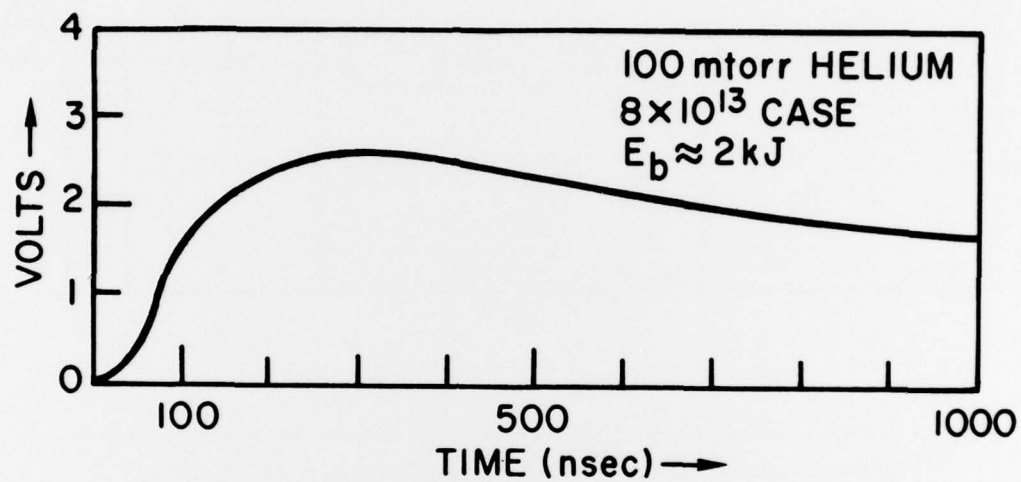
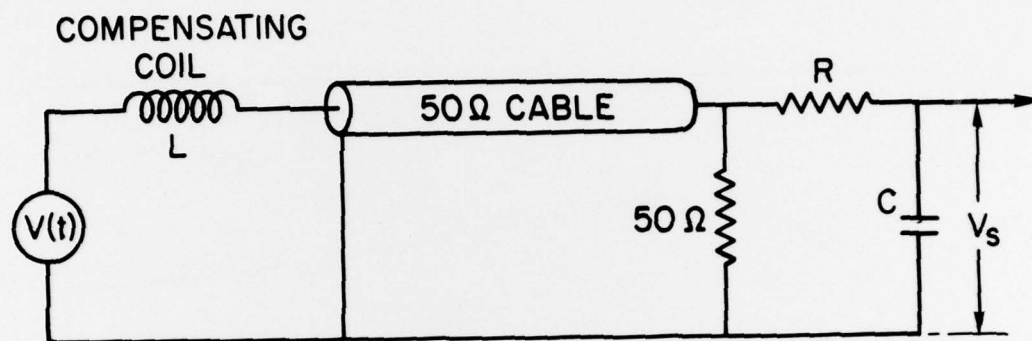
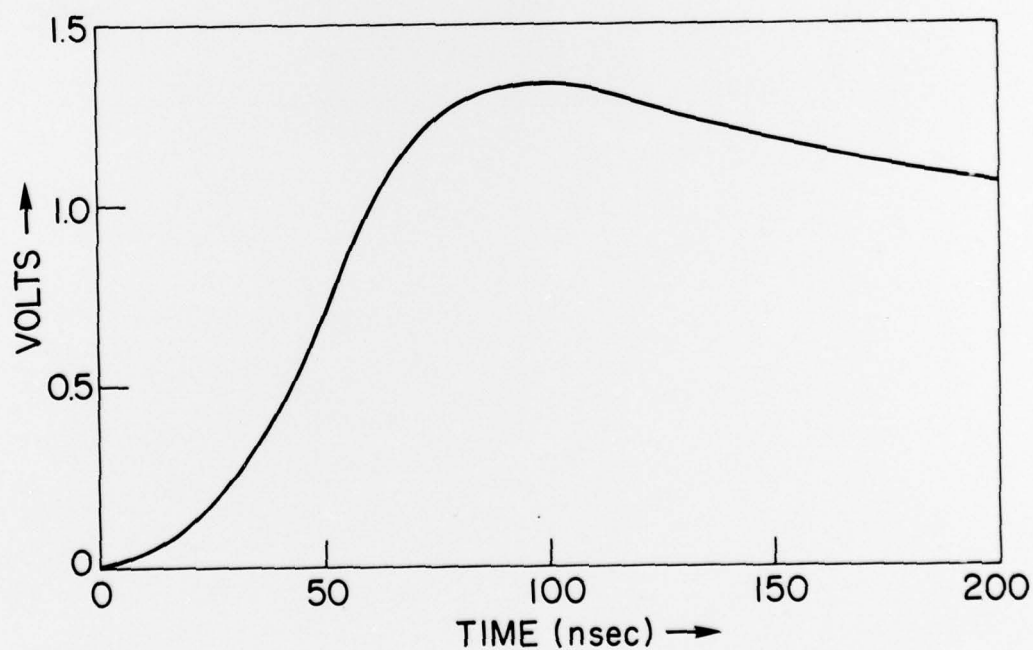


Fig. 16 — Typical corrected diamagnetic loop signal for the 8×10^{13} case



(a)



(b)

Fig. 17 — (a) Circuit used to approximate the diamagnetic loop circuit.
(b) Expected signal from the diamagnetic loop resulting from the transverse energy pulse described in the text and using the circuit shown in part (a).

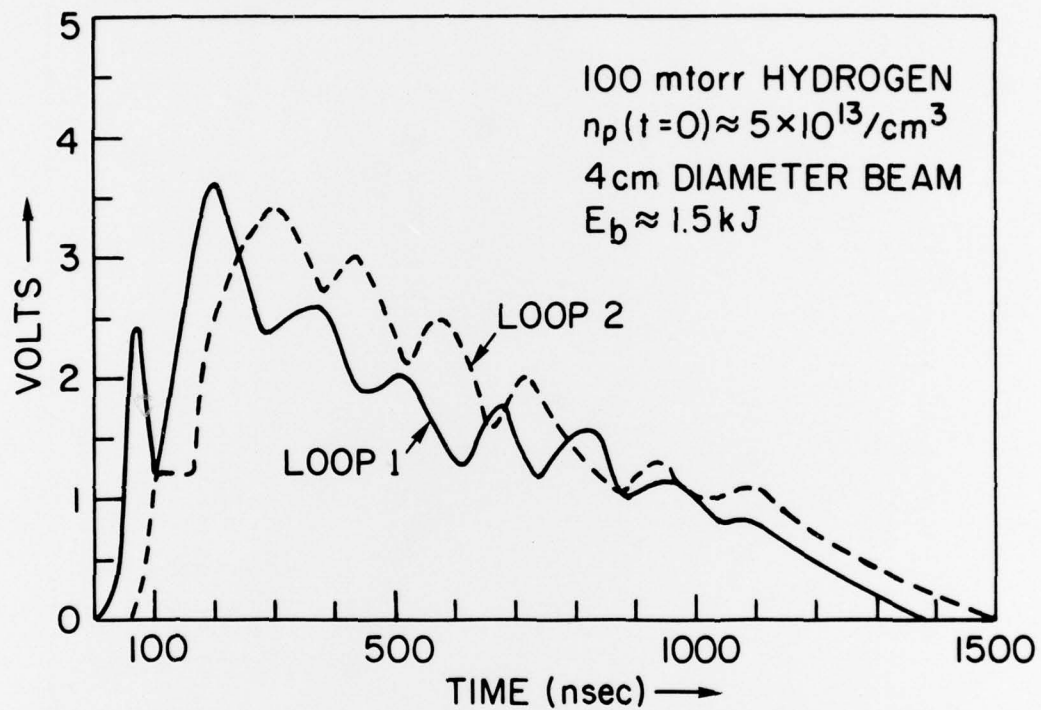


Fig. 18 — Diamagnetic loop signals from loops at both ends of the theta pinch in a partially ionized hydrogen experiment. Oscillations were present in most hydrogen cases.

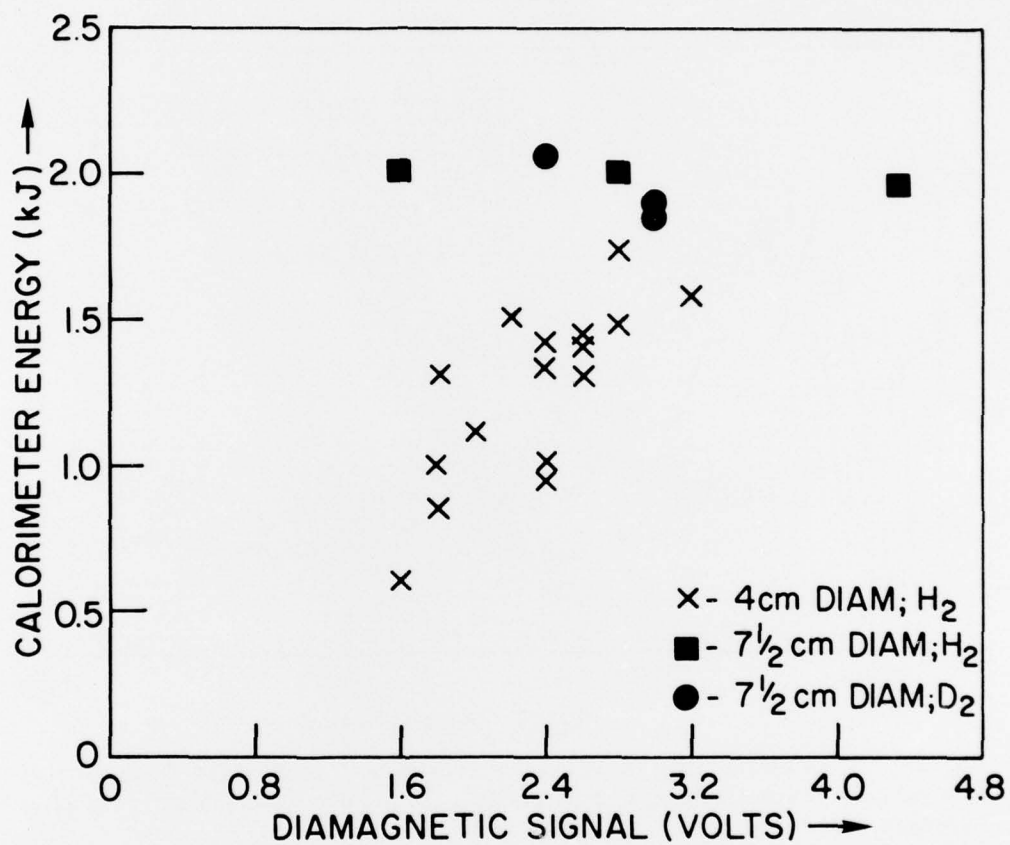


Fig. 19(a) — Comparison of diamagnetic loop amplitude and beam energy on the calorimeter, for partially ionized hydrogen experiments

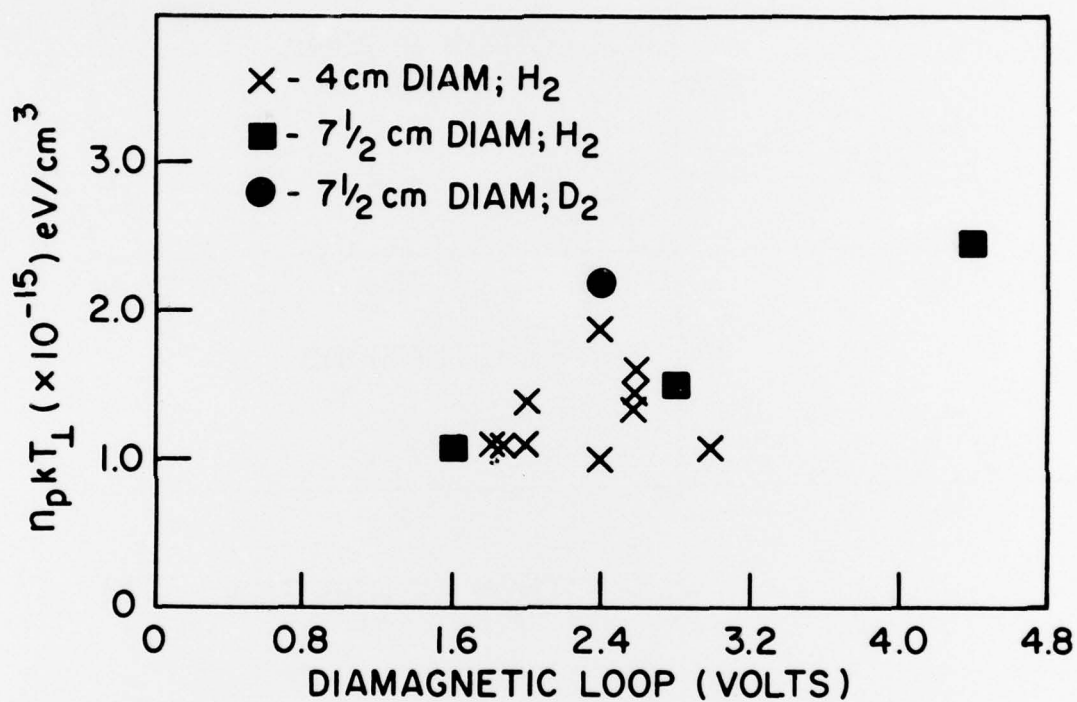


Fig. 19(b) (Continued) — Comparison of diamagnetic loop amplitude and $n_p k T_{\perp}$, obtained from Thomson scattering, for partially ionized hydrogen experiments

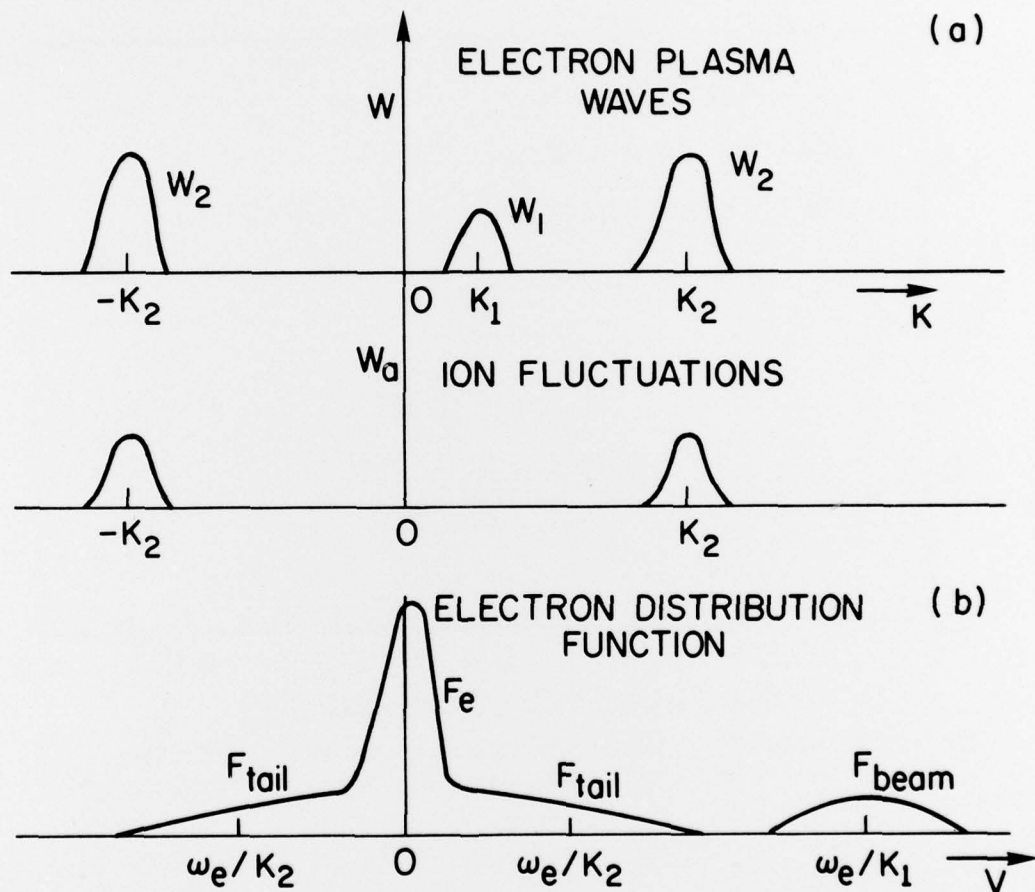


Fig. 20 — Nonlinear quasistationary state of the beam-plasma system. (a) Spectral distribution of electron plasma (Langmuir) waves (W) and ion waves (W_a). (b) Schematic of the electron distribution function including the slowly drifting plasma component, plasma electron tails, and beam electrons.

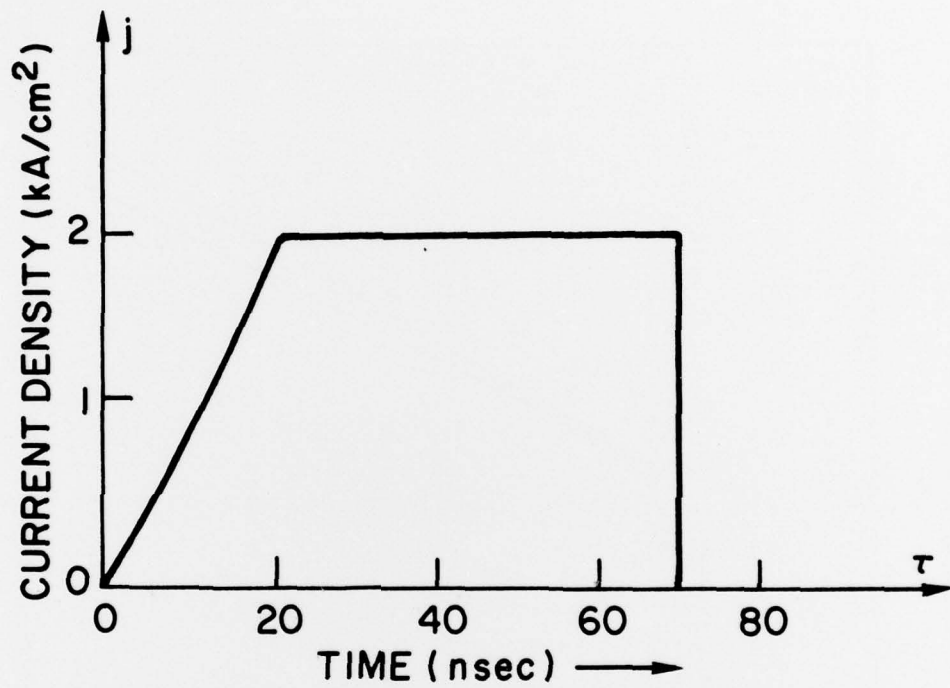


Fig. 21 — Beam current density pulse shape used for the theoretical comparison with experiment

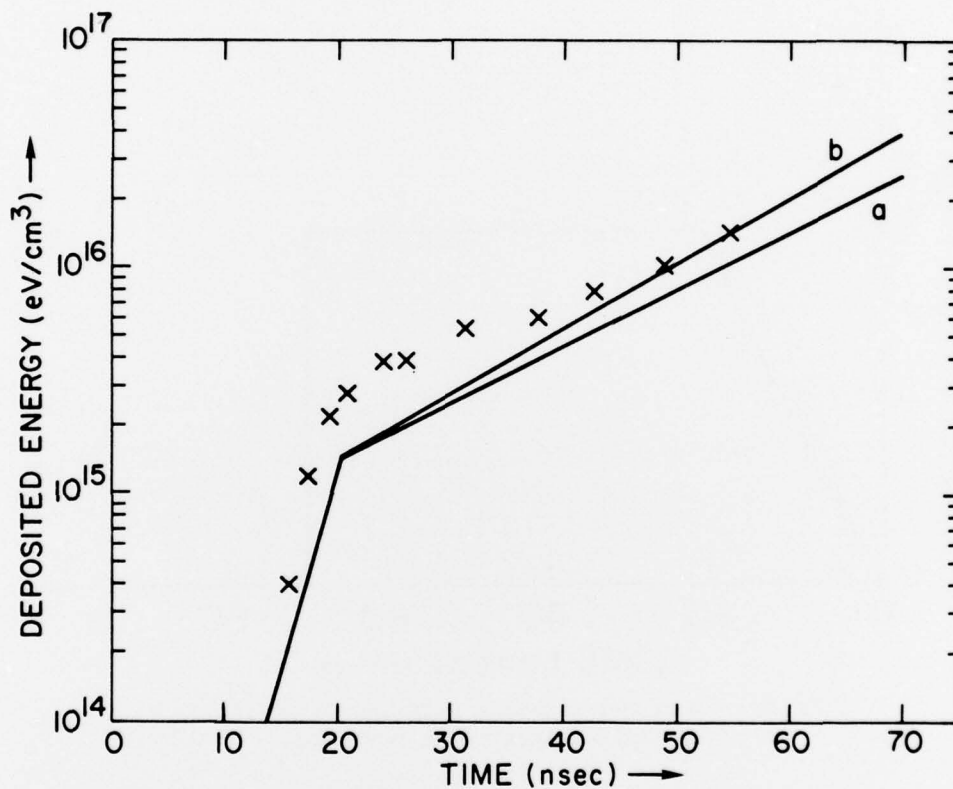


Fig. 22 — Beam energy deposition rate as a function of time for the highly ionized case. Continuous lines are averaged results from the approximate analytic theory. Line (a) represents deposition due to wave damping, while (b) is the total including the resistive heating. The points are results from the numerical solution of the exact mode coupling equations including only wave damping.

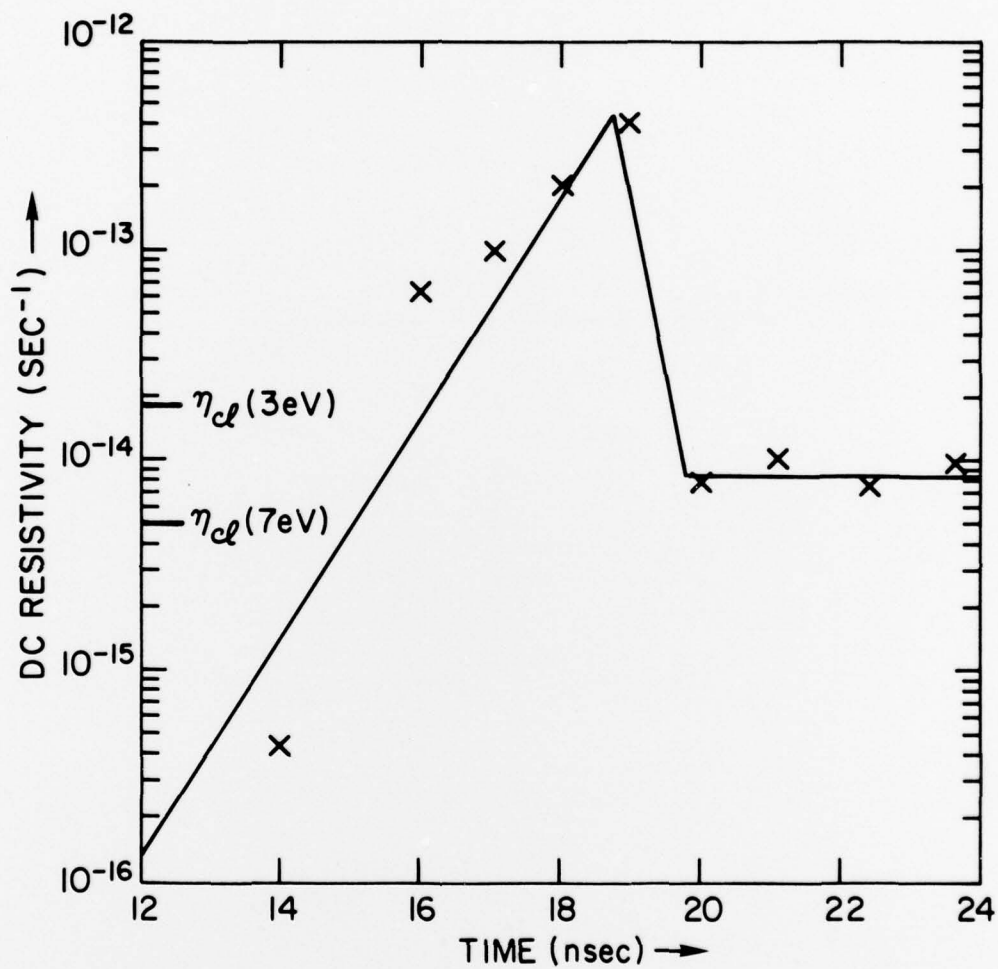


Fig. 23 — Time dependence of anomalous resistivity for the case considered in Fig. 22. Again the line is from the analytic model while the points are from the numerical experiments averaged over a ~ 1 ns time interval.

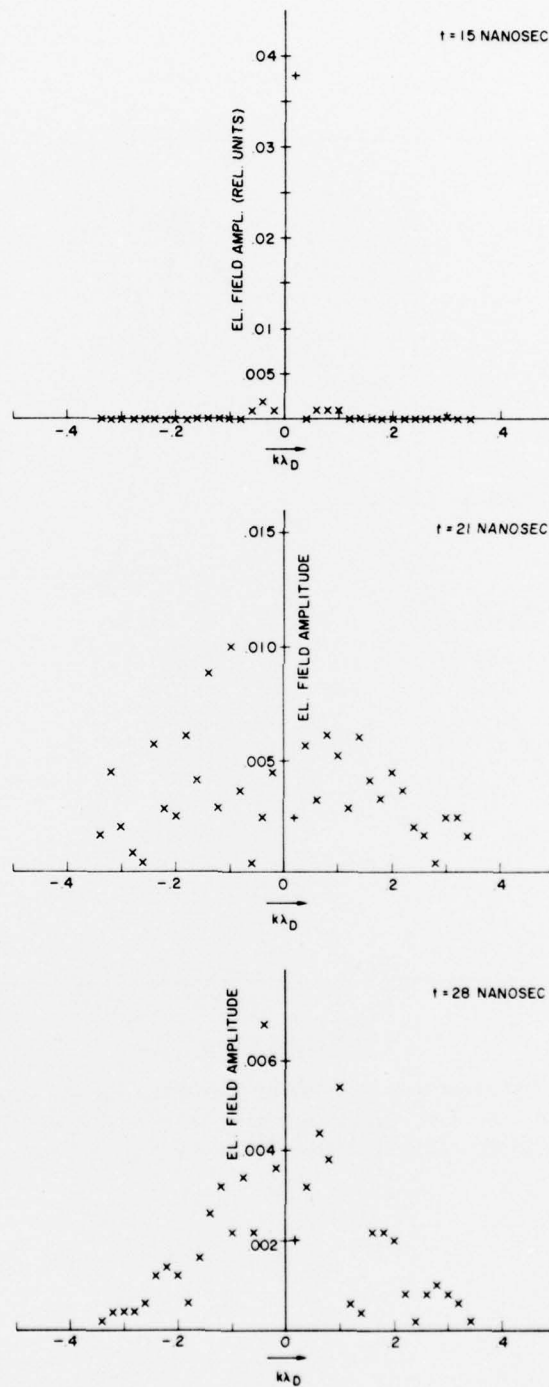


Fig. 24(a) — High frequency (ω_p) spectra from the numerical simulation for the highly ionized case. The waves in resonance with the beam are indicated by +.

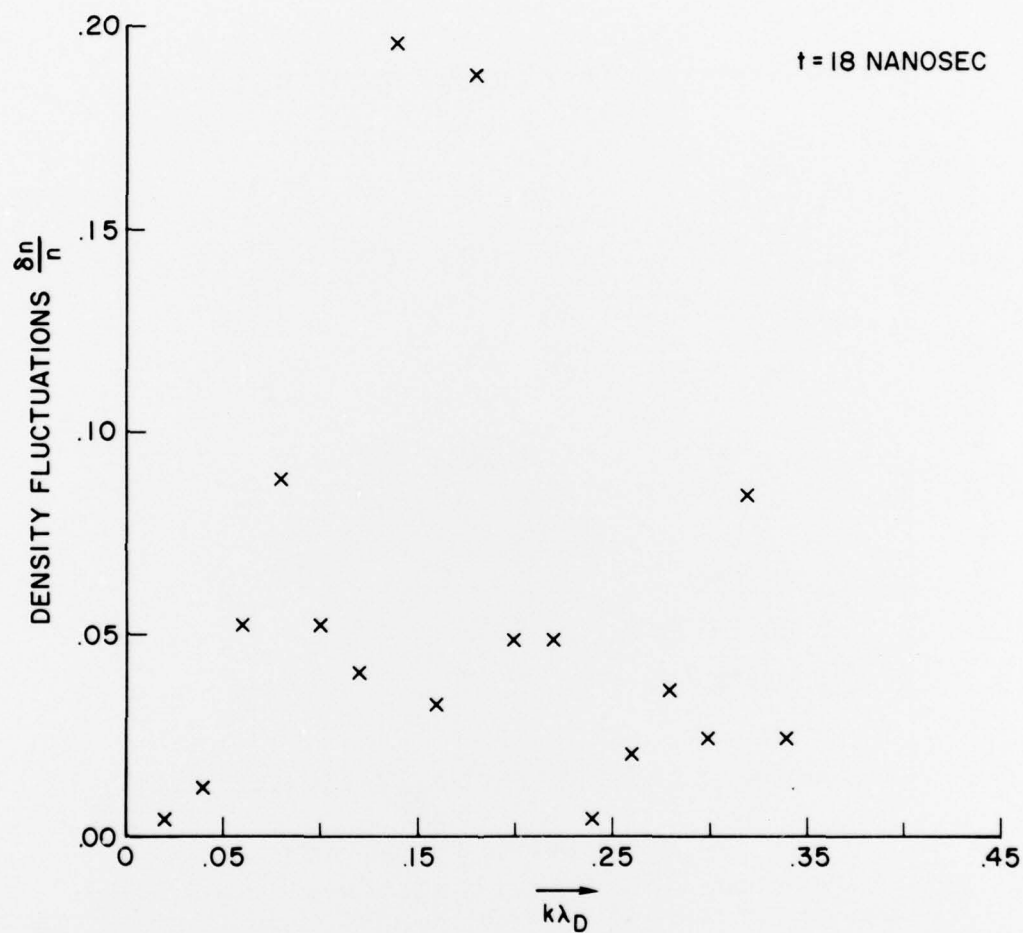


Fig. 24(b) (Continued) — Low frequency ($< \omega_{pi}$) spectra from the numerical simulation for the highly ionized case. The waves in resonance with the beam are indicated by +.

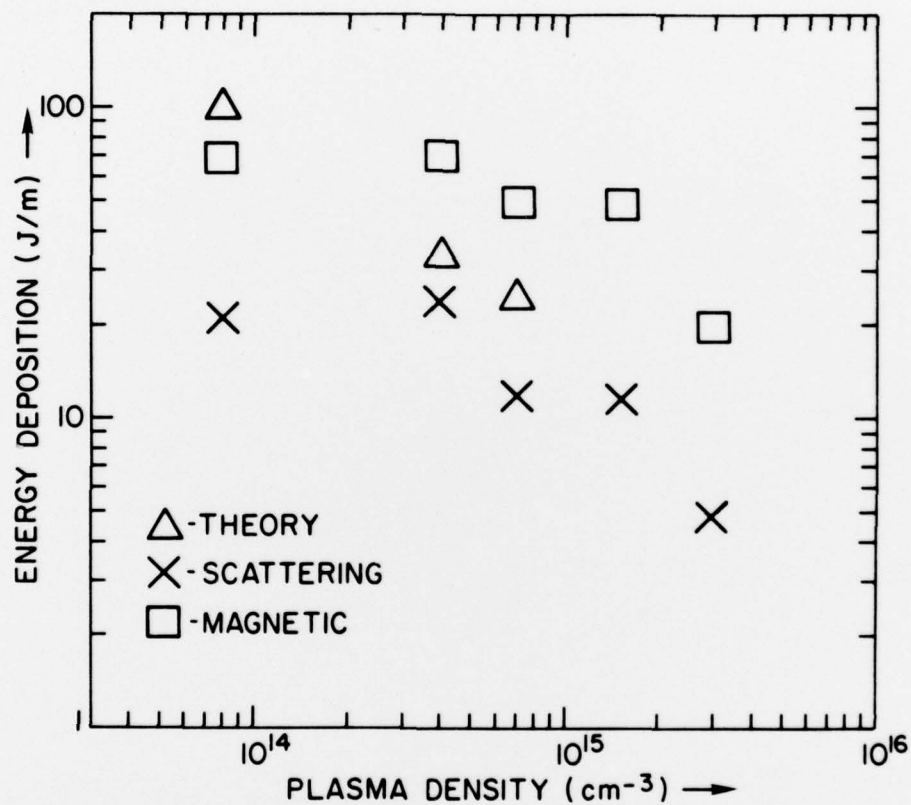


Fig. 25 — Energy deposition as a function of plasma density: a comparison of experimental observations and theoretical predictions. Note that the two lower density cases are partially ionized helium and the other three are highly ionized hydrogen.